Glacier dynamics and subsurface classification of Austfonna, Svalbard: Inferences from observations and modelling

Thorben Dunse

Dissertation submitted for the degree of Philosophiae Doctor (PhD)

Department of Geosciences
Faculty of Mathematics and Natural Sciences
University of Oslo

Oslo, Norway 2011

Series of dissertations submitted to the
Faculty of Mathematics and Natural Sciences, University of Oslo
No. 1080

ISSN 1501-7710

Cover: Inger Sandved Anfinsen.
Printed in Norway: AIT Oslo AS.

Produced in co-operation with Unipub.
The thesis is produced by Unipub merely in connection with the
thesis defence. Kindly direct all inquiries regarding the thesis to the copyright
holder or the unit which grants the doctorate.

Abstract

Ice loss from glaciers and ice caps in the Arctic constitute a major contribution to eustatic sea-level rise. Climate change is more pronounced in the Arctic than in other regions, because strong feedback mechanisms such as the albedo feedback lead to enhancement of the initial warming trend. Glaciers and ice caps serve as valuable indicators of past and present climate. However, extraction of climate signals from glaciers is not straightforward. The history, current state and future evolution of glaciers result from external factors, e.g. air temperature or precipitation, and intrinsic glacier dynamics, such as changes in thermal structure or subglacial drainage. Climatically-driven and dynamic processes may interact with each other and either moderate or amplify the glacier's response to climate change.

This thesis is a contribution to the project GLACIODYN: 'The dynamic response of Arctic glaciers to global warming', under the framework of the International Polar Year (IPY) 2007–10. It addresses the dynamic behaviour and mass balance regime of Austfonna by combining geophysical techniques for glacier observation and numerical modelling. Austfonna is one of the largest ice caps in the Arctic and by far the largest land-ice mass on the highly glacierized Svalbard archipelago. Observed interior thickening and marginal thinning of Austfonna during the last decade is presumably related to slow glacier dynamics of several basins that are known to have surged in the past and are currently in the quiescent phase. The observed changes may also partly be imposed by changes in the surface mass balance (SMB). Austfonna's total mass balance during the last decade was negative. Ice-mass loss was primarily attributed to calving from marine terminating outlets and retreat of the marine ice margin. The calving flux depends on the rate at which ice is transported towards the calving front. Previous estimates rely on ice-surface velocity maps that represent snapshots during mid-1990s winter months.

The spatial and temporal variability in snow accumulation is inferred by ground-penetrating radar (GPR). The previously suggested snow-accumulation pattern of Austfonna with about twice as much snow accumulation in the southeast compared to the northwest and a large interannual variability in the total amount of snow is confirmed

for the observational period. Rigorous GPR data processing reveals distinct radar zones and allow to distinguish between firn and superimposed ice underneath the last-summer surface, as well as pure glacier ice, representing multi-year-mean accumulation and ablation, respectively. Repeated GPR surveys along coincident transects in spring 2004–07 are utilized to derive time series of radar zones and detect temporal and spatial changes in the SMB regime. Following an initial decrease in 2003–04 the firn area grew in subsequent years of observations, both in terms of the areal extent and thickness, creating favorable conditions for the retention of surface melt in form of internal accumulation and superimposed ice, which constitute a large contribution to the accumulation of Austfonna.

Continuous GPS measurements over the period 2008–10 are utilized to investigate seasonal velocity changes along the central flowlines of two marine-terminating fast-flow units, Basin-3 and Duvebreen. Results from low-frequency GPR and a nearby Automatic Weather Station (AWS) provide supplementary information with respect to glacier geometry and timing of surface melt. The analysis gives insights into mechanisms that may influence basal motion, characteristic bedrock topography above/below sea level, timing and volume of meltwater input into the subglacial drainage system and drainage characteristics. At Basin-3, the observed annual mean ice-surface velocities exceed those measured by InSAR in the mid 1990s by a factor $\gtrsim$3, indicting that ice loss due to calving from this outlet may be significantly larger then previously anticipated. A marked speed-up following the onset of the summer melt period is recorded at both Basin-3 and Duvebreen, implying enhanced basal motion through input of meltwater into the subglacial drainage system. Air temperatures during summer 2009 were significantly higher than in 2008 and the relation between observed ice-surface velocity and melt periods is more complex. This suggests a transition to a hydraulically more efficient drainage system that can accommodate repeated meltwater input without increased basal water pressure.

To gain a better knowledge of the present-day dynamics of Austfonna and surge-type behaviour of individual basins in particular, the existing ice-sheet model SICOPOLIS is employed. Implementation of the new model domain involves compilation of a comprehensive model-input dataset, comprising surface and bedrock topography, and the climatic forcing in terms of precipitation and air temperature. Steady-state model experiments are performed with the present-day geometry as initial conditions and the present-day climate is applied as external forcing. Mechanisms that may govern the dynamic characteristics are investigated by systematically changing the description of basal motion. Depending on the chosen parameter combinations, simulated fast-flow units operate in a mode of steady fast-flow or cyclic surge behaviour. The model results suggest that a

change in the basal thermal regime, ultimately controlled by the long-term evolution of the glacier geometry, is decisive for surge-type behaviour, but not sufficient. The model successfully generates surge-type behaviour if the transition from no-slip to full basal sliding occurs within a narrow temperature range near the pressure-melting point (PMP), and if combined with enhanced sliding of ice regions grounded below sea level, e.g. representing plastic deformation of water-saturated sediments. This scenario is in agreement with previous observations of unconsolidated sediments beneath the marine grounded ice and statistical model results, suggesting a thermally controlled soft-bed surge mechanism for Svalbard glaciers. Fast flow is accomplished by basal motion over a temperate bed. Irrespective of the dynamic regime, considerable volumes of temperate ice are, however absent, both in the observed and simulated ice cap. The simulated steady states of Austfonna provide idealized initial conditions for prognostic model runs that allow to assess the uncertainties in the dynamic response of the ice cap to climate change.

Finally, prognostic model runs are performed under the framework of the model initiative GlacMod2010 that aims at investigating the response of an appreciable number of simulated glaciers and ice caps to a set of simple climate-change scenarios. Due to the short simulation period from 2010–2100 (90 years), compared to the principle period of simulated surge-type behaviour (200–500 years), the model was set-up with flow units in steady fast-flow. The prescribed increase in precipitation is found insufficient to compensate for the non-linear increase in mass loss associated with the warming scenario.

Acknowledgements

This thesis would not have been possible without the support and inspiration from a whole bunch of people. First of all, I thank my supervisors, Jon Ove Hagen and Thomas Vikhamar Schuler, for always having their doors open for me and for being positive towards the discussion of new ideas. They encouraged me to participate in numerous conferences, fieldwork and summer schools which made me feel part of the international glaciological community. Jon Ove has the talent to figure out additional funding when it is needed. Thomas was of great help concerning technical issues, paper writing and last but not least, as a climbing buddy. All the people involved in the activities on Austfonna deserve a big thanks. Trond Eiken was indispensable with respect to field logistics, radar (800 MHz) and kinematic GNSS measurements. Geir Moholdt provided great company in both field and office, and probably as many good discussions about Austfonna as about skiing. I thank my colleagues at the University of Oslo and associated Institutes, including Anne Chapuis, Karsten Müller, Chris Nuth, Kirsty Langley, Anna Sinisalo, Torbjørn Østby and many others for good discussions, coffee breaks and a lot of fun beyond the professional live.

International collaboration played an important role in the collection of data presented in this thesis. Carleen Reijmer and the Institute for Marine and Atmospheric Research Utrecht provided the GPS receivers, which enabled us to collect a great record of ice-surface velocities. Francisco 'Paco' Navarro and Evgeniy Vasilenko joined our fieldwork in 2008 to collected the low-frequency radar data.

I am grateful for having been given the opportunity to experience the magnificent culture and natural beauty of Japan, connected to a 4 months research stay in Sapporo, Hokkaido. Ralf Greve at the Institute of Low Temperature Science (ILTS), Hokkaido University, was a welcoming host. Ralf guided me towards the essential modules and parameters of the ice-sheet model SICOPOLIS that facilitated exciting simulations of Austfonna. Tatsuru Sato and other colleagues at ILTS were incredible helpful and patient, getting me started in Sapporo and making my stay so enjoyable. Arigato gozaimashita!

Gudfinna 'Tolly' Adalgeirsdottir at the Danish Meteorological Institute happily shared her knowledge about the model with me.

A major part of my funding throughout the years was provided by the Norwegian Research Council under the framework of GLACIODYN as part of the International Polar Year, the ESA CryoSat calibration/validation experiment CryoVEX and the ice2sea programme of the European Union 7th Framework Programme. Arctic field grants through the Svalbard Science Forum in 2007/08 allowed me to participate in the fieldwork on Austfonna. The Japanese Society for the Promotion of Science provided me with a short-term pre-doctoral fellowship enabling my research stay in Japan.

Last but not least, I thank my mother, Karin, and my brother, Sven, as well as my friends. Thank you for your confidence that I will eventually make it through this project, and for dragging me away from it when needed–preferably into the depths of Nordmarka: No matter what season of the year, this invaluable forest around Oslo provides alleviation and joy. Tusen hjertelig takk for mange fine turer!

Thorben Dunse

Oslo, Norway
March 2011

Contents

List of Figures

List of Tables

Acronyms and Abbreviations

ELA	Equilibrium-Line Altitude
CTS	Cold-Temperate transition Surface
DEM	Digital Elevation Model
F	Firn
EM	Electro Magnetic
ESA	The European Space Agency
GLACIODYN	The Dynamic Response of Arctic Glaciers to Global Warming
GNSS	Global Navigation Satellite System
GPR	Ground-Penetrating Radar
GPS	Global Positioning System
IA	Internal Accumulation
IBCAO	International Bathymetric Chart of the Arctic Ocean
InSAR	Interferometric Satellite Aperture Radar
IPCC	Intergovernmental Panel on Climate Change
IPY	International Polar Year
IRH	Internal Reflection Horizon
IS	Initial State (for model runs)
LSS	Last Summer Surface
PDD	Positive Degree Days
PMP	Pressure-Melting Point
NPI	The Norwegian Polar Institute
RES	(airborne) Radio-Echo Sounding
SI	Superimposed Ice
SIA	Shallow-Ice Approximation
SLE	Sea-Level Equivalent
SMB	Surface Mass Balance
SSA	Shallow-Shelf Approximation
TWT	Two-Way Traveltime
UIO	The University of Oslo
VIRL	Video Impulse Radio Locator
w.e.	water equivalent

Part I

Overview

1 Introduction

1.1 Motivation

The role of glaciers as indicators of climate change is widely acknowledged and there is a growing public demand for estimates on future glacier change and associated contribution to global sea-level rise. Global sea-level rise affects ocean circulation and ocean ecosystems and bears significant socio-economic challenges. The total sea level rise for the period 1993–2003, in terms of sea-level equivalent (SLE), has been estimated to $3.1 \pm 0.7\,\mathrm{mm\,SLE\,a^{-1}}$ of which about half, $1.6 \pm 0.5\,\mathrm{mm\,SLE\,a^{-1}}$ is attributed to thermal expansion of the warming ocean water (Solomon *et al.*, 2007). About $1.8\,\mathrm{mm\,SLE\,a^{-1}}$ is attributed to additional water input to the oceans, the 'eustatic sea-level rise', of which glaciers and ice caps other than the ice sheets of Antarctica and Greenland currently account for ∼60% (Meier *et al.*, 2007). Their contribution has been increasing from 0.35–$0.4\,\mathrm{mm\,SLE\,a^{-1}}$ between 1961–90, referred to as climatic-normal period, to 0.8–$1.0\,\mathrm{mm\,SLE\,a^{-1}}$ for the period 1991–2004 (Kaser *et al.*, 2006).

The Arctic region constitutes a large fraction of the worldwide area covered by glaciers and ice caps. Over the coming decades, ice mass loss from Arctic glaciers is expected at accelerating rates. Global warming is known to be amplified in the Arctic, owing to positive feedback mechanisms, such as the albedo feedback associated with changes in the areal extent and surface characteristics of sea and land-ice masses, as well as the perennial snow cover, or thawing of permafrost and the stability of the lower troposphere (Serreze *et al.*, 2000). Air temperature is expected to increase by 3–5°C over land areas and up to 7°C over the oceans (ACIA, 2004).

Direct measurements of glacier mass balance are only available since the mid 20th century, generally covering less than 100 glaciers at a time (Kaser *et al.*, 2006). The pool of measured glaciers is biased towards smaller glaciers at lower elevations, selected for reason of their relative accessibility and safety. These glaciers tend to have more negative mass balances than more remote and large Arctic glaciers (Kaser *et al.*, 2006). Advances in satellite remote-sensing techniques during the last decades allow to monitor glacier vol-

ume changes over large regions. Densification of the extensive firn area of Arctic glaciers complicate the conversion of measured volume to mass changes, as spatial and temporal density variations have to be accounted for. Large quantities of meltwater may percolate and refreeze in the firn, termed 'internal accumulation' (IA). Superimposed ice (SI) formation on top of impermeable ice and IA are difficult to quantify, but may account for 5–100% of the total net accumulation of Arctic glaciers (Rabus and Echelmeyer, 1998).

A large part of the ice flux within Arctic ice caps occurs through spatially limited flow units. These flow units may be characterized by steady fast flow, or surge-type behaviour, characterized by long quiescent phases alternating with short lived surge phases. Surge-type glaciers undergo significant changes in glacier dynamics and geometry that are largely decoupled from climate variability, challenging both observational glaciologists and modellers to deliver estimates on glacier response to climate change. Glacier evolution is climatically controlled through the surface mass-balance (SMB), i.e. accumulation and ablation, and dynamically through the ice flux from the interior towards the margins (Hagen *et al.*, 2005). Increased ice flux results in a lowering of the glacier surface and makes the glacier more vulnerable to rising air temperatures, causing a feedback that leads to further melt and accelerating ice flux. This dynamic instability may amplify glacier response to climate change significantly. Yet, its potential contribution to eustatic sea-level rise (SLR) is excluded from the last consensus estimate (0.18–0.6 m until 2100) of the Intergovernmental Panel on Climate Change (IPCC) Fourth Assessment (Solomon *et al.*, 2007).

Recent ice mass loss appears to be dominated by rapid retreat and thinning of marine-terminating glaciers grounded below sea level (Meier *et al.*, 2007). Iceberg calving allows for rapid ice mass loss that may exceed surface melt also in a warming climate. Exceptional iceberg calving events, such as the 'Heinrich events' associated with surges of the prehistoric Laurentide ice sheet (MacAyeal, 1993), also provide a mechanisms for the rapid disintegration of marine ice sheet. A better understanding of the combined effects of ice dynamics, iceberg calving and SMB is required to asses the current and future response of glaciers and ice caps to future global warming (Burgess and Sharp, 2008).

Here, I focus on the Austfonna ice cap, the largest individual ice body on the highly glacierized archipelago of Svalbard, in the Eurasian Arctic (Fig. 3.1). Several of Austfonna's drainage basins are known to have surged in the past (Schytt, 1969; Dowdeswell, 1986). Austfonnas SMB is characterized by large interannual variations (Pinglot *et al.*, 2001; Taurisano *et al.*, 2007). Internal accumulation and superimposed ice give a large contribution to the net accumulation (Schuler *et al.*, 2007). The ice cap is selected as

validation/calibration site for the European Space Agency's (ESA) CryoSat mission, due to the diversity in subsurface characteristics that influence the radar signal of the satellite altimeter. Recent observations suggested considerable thickening in the interior and thinning at the margins (Bamber *et al.*, 2004; Moholdt *et al.*, 2010a). Such geometry changes are potentially related to both surface processes as well as ice dynamics (Hagen *et al.*, 2005). Large regions of the ice cap are grounded below sea level, forming an extensive tidewater coastline and allowing for the discharge of large volumes of icebergs into the Barents Sea (Dowdeswell, 1989). Austfonna may therefore be regarded as a miniature example of a marine ice sheet, such as the West Antarctic Ice Sheet. Austfonna's comparably small size and simple dome-shaped topography makes it a suitable case study for observations and modelling of marine-ice dynamics.

1.2 Objectives

This thesis is a contribution to the project GLACIODYN–The dynamic response of Arctic glaciers to global warming–under the framework of the International Polar Year (IPY) 2007–10. It aims at gaining a better understanding of the dynamic behaviour of Austfonna and its SMB characteristics by combining geophysical and traditional methods of glacier observations with numerical modelling. It is essential to determine the relative impact of climatically and dynamically driven processes, in order to properly assess the ice cap's response to climate change.

With respect to the SMB, repeated ground-penetrating radar (GPR) surveys along fixed transects are employed to investigate the spatial and temporal variability in snow accumulation. The information content of the GPR data is exploited beyond the commonly assessed winter balance, i.e. by identifying and monitoring the distribution of distinct glacier facies.

With regards to the dynamics of Austfonna, temporal variations in the ice-surface velocity of spatially limited flow units are addressed by continuous observations of ice-surface velocities. Given supplementary information from low-frequency GPR and a nearby automatic weather station (AWS) the aim is to provide insights into mechanisms that may influence basal motion, the role of characteristic bedrock topography, timing and volume of meltwater input into the subglacial drainage system and drainage characteristics. Finally, present-day velocities are compared with previous spaceborne results that are restricted to winter snapshots during the mid 1990s.

To gain a better understanding of the present-day velocity structure and configuration an existing numerical model is applied to Austfonna. Special focus is put on the surge-type behaviour of several drainage basins and the potential role of large ice regions grounded below sea level. This task involves compilation of a comprehensive model input, consisting of surface and bedrock topography and the external forcing in terms of air temperature, precipitation and geothermal heat flux. The model input builds on existing field measurements and data retrieved during the course of the thesis project.

1.3 Outline

This thesis is divided into two parts. Part I comprises an overview of the thesis of which this introduction constitutes the first chapter. The relevant glaciological background is provided in Chapter 2. Chapter 3 introduces the Austfonna ice cap and summarizes previous research activities, relevant to the objectives of this thesis, and their findings. Chapters 4 and 5 address the methodological approaches with respect to geophysical methods and modelling. Chapter 6 provides a summary of the main results presented in three papers and one report. Finally, Chapter 7 closes Part 1 with suggestions for future work.

Part II is a collection of three papers that present the main achievements of this thesis. The papers are referred to by Roman numbers. Paper I: 'Recent fluctuations in the extent of the firn area of Austfonna, Svalbard, inferred from GPR' is published in the *Annals of Glaciology* 50(50), 2009; Paper II: 'Continuous GPS surface velocity measurements on two fast flowing outlet glaciers of Austfonna, Svalbard' is a manuscript to be submitted, e.g. to *The Cryosphere*; and Paper III: 'Permanent fast flow vs. cyclic surge behaviour: numerical simulations of the Austfonna ice cap, Svalbard is published in the *Journal of Glaciology*, 57(202), 2011.

2 Theoretical Basis

This chapter outlines the glaciological theory relevant for this thesis, loosely following the textbooks by Paterson (1994) and Greve and Blatter (2009), as well as further cited publications.

2.1 Glacier mass balance

The mass balance of glaciers concerns the storage and release of water and has therefore implications on eustatic sea level change. Glaciers and ice caps other than the Greenland and Antarctic Ice Sheets only represent a small fraction of the water stored as land ice. However, they currently constitute the largest source of water input into the world ocean (Meier *et al.*, 2007).

2.1.1 Surface mass balance and glacier facies

The glacier surface is divided into an area of net accumulation, where the glaciers gains mass during the course of a balance year, and an area of net ablation, where mass is lost. These areas are separated by the equilibrium-line altitude (ELA). A balance year usually starts and ends at the end of two consecutive summer melt seasons. A balance year is ideally split up in periods of predominant accumulation or ablation, the winter and summer balance, respectively. The total annual mass balance M is the balance between the annual SMB, B_n, consistent of accumulation, M_acc, and ablation, M_abl, and iceberg calving, M_c (Hagen *et al.*, 2003):

$$M = M_\mathrm{acc} - M_\mathrm{abl} - M_\mathrm{c} \tag{2.1}$$

At Austfonna, no floating ice tongues exist and associated terms of bottom melting or freezing-on do not need to be accounted for. The SMB for the entire glacier is calculated by integrating the local SMB rate, $\dot{b}$, over the area, A, and the time period of a particular

balance year, t. The dot decoration denotes the derivative with respect to time. The total annual change of glacier ice mass, M, becomes:

$$M = \int_t \int_A \rho \dot{b} \, \mathrm{dA} \, \mathrm{d}t - M_\mathrm{c}, \tag{2.2}$$

where ρ is the density of snow, firn or ice.

The spatial variability in SMB manifests itself in zones of characteristic surface properties, referred to as glacier facies (Paterson, 1994). Arctic glaciers and ice caps experience surface melt even at their highest elevations, although melting is generally restricted to a short summer melt season. In the 'percolation zone', meltwater penetrates into the cold snow and refreezes. Refreezing meltwater provides a large source of latent heat, considerably warming the snow. If the temperature of the snowpack is raised to melting point at the end of the summer season, i.e. the cold content is eliminated, the area is referred to as the 'wet-snow' or 'soaked zone'. Its lower border marks the snow line. Meltwater that refreezes on top of the impermeable bare ice below the snowline, and survives the summer melt season, is called 'superimposed ice'. The lower limit of the SI zone marks the ELA. In the ablation area below, all snow and some additional ice mass is lost by the end of the summer melt season. The percolation and wet-snow zone can be summarized as the firn zone. The extensive firn area of Arctic glaciers represents a large reservoir for water storage. Meltwater may be retained within the annual snowpack or penetrate beyond the last summer surface (LSS) and refreeze within previous year's firn layers, termed 'internal accumulation' (IA). Both SI and IA can have a significant contribution to the mass balance of Arctic glaciers, but are difficult to measure (Hagen *et al.*, 2003). Internal accumulation results in firn densification (Pfeffer and Humphrey, 1996; Reeh, 2008) and inclusions of solid ice clusters constitute a strong density contrast with the surrounding snow/firn matrix. This has unfortunate implication for remote sensing analysis, that may lead to erroneous determination of surface elevation and large uncertainties in the conversion of the observed volume changes to mass changes, associated with temporal and spatial density variations (Li *et al.*, 2007; Helsen *et al.*, 2008).

In a warming climate, as observed during the last few decades, the mass balance gradient with elevation tends to steepen, due to increased melt at lower and increased snow accumulation at higher elevations, resulting in an increased mass turn over (Dyurgerov and Meier, 2005). The position of the ELA may also move upglacier, thereby decreasing the accumulation area ratio.

2.1.2 Calving flux

Iceberg calving constitutes substantially to the ice mass loss from Arctic tidewater glaciers and ice caps, that may have a considerable fraction of marine ice. Floating ice shelves or tongues are not a common phenomenon in the Arctic, and hence, marine ice refers here to ice that is grounded below sea level. Changes in the flux of land-based ice into the ocean affect global sea-level, in contrast to calving of floating ice.

The calving flux, M_c, is defined as the volume of icebergs released per time, t, and unit area of a vertical calving front:

$$M_c = \int_c \rho_i W_T H_T u_c \, dt, \tag{2.3}$$

where W_T is the terminus' width, H_T the ice thickness of the terminus. The calving rate, u_c, is given by the difference between the depth averaged ice velocity at the glacier terminus, $\overline{u}_T$ and the change of glacier length, L over time:

$$u_c = \overline{u}_T - \frac{dL}{dt}. \tag{2.4}$$

Marine ice is potentially unstable. Sequences of ice rafted debris in marine sediment cores from the North Atlantic provide geological evidence of periodic large-scale marine ice disintegration of the Laurentide Ice Sheet. The associates events of major iceberg-discharge are known as Heinrich events (Heinrich, 1988; Broecker *et al.*, 1992). Most of the understanding of marine-ice dynamics is based on studies of grounded tidewater glaciers. Clarke (1987) suggested that the advance-retreat cycle of tidewater glaciers may be nearly independent of climate and mainly a function of fjord geometry. For tidewater glaciers, retreat from one stable terminus position may cause rapid retreat to the next anchor point, while advance rates are usually slow (Meier and Post, 1987). The retreat from a anchor point is associated with a reduction in longitudinal backstress, leading to increased velocity and horizontal stretching (Meier and Post, 1987). This indicates complex feedback mechanisms between calving and ice dynamics. Key factors that govern calving include ice thickness of the marine terminus relative to water depth, the 'flotation thickness', along-flow variations of longitudinal strain rates that determine the crevasse formation and surface melt, that may cause hydraulic fracturing. Several empirical relations have been derived to describe the calving rate of grounded tidewater glaciers and aim at providing estimates on long-term calving rates (>1 year) rather than to capture individual calving events or short-term changes.

Brown *et al.* (1983) suggested a linear relation between the calving rate and water depth at the calving front. Other studies point at the limitation of the simple linear water-depth relation. Meier and Post (1987) pointed out that if the terminus retreats into deeper water, the calving rate may increase non-linearly and approach to flotation may become the controlling factor. An alternative treatment of calving is provided in the flotation model, where the position of the calving front coincides with a critical height of the calving front above flotation (van der Veen, 1996). Similar to the water-depth relation, calving increases when the terminus moves into deeper water and only stabilizes when the water depth decreases. Implementation of the height-above flotation criterion in one and two-dimensional numerical models therefore leads to unstable retreat of marine terminus over a basal depression (Vieli *et al.*, 2001).

A physically based calving criterion by Benn *et al.* (2007) does not directly depend on water depth and facilitates also glacier advance into deeper water (Nick *et al.*, 2010). This waterline crevasse-depth model locates the calving margin where the depth of surface crevasse, equals the ice height above sea level. The crevasse depth is calculated from the longitudinal strain rate, according to Nye (1957) and Glen's flow law (Eq. 2.5). Crevasses, filled with water of depth have enhanced crevasse depth due to hydraulic fracturing. This allows linkage of calving rate to climate-sensitive variables, such as temperature and surface melt.

2.2 Thermal regime

Svalbard glaciers are characterized by polythermal/subpolar thermal regime. Polythermal glaciers comprise regions of cold and temperate ice, i.e. ice at the pressure-melting point (PMP), separated by the cold-temperate transition surface (CTS) (Macheret *et al.*, 1991; Björnsson *et al.*, 1996). Small glaciers may also be entirely cold.

The vertical temperature distribution in glaciers is controlled by the surface temperature at the top and the geothermal heat flux from the lithosphere beneath the glacier base. In steady-state, the temperature increases with depth, depending on the thermal conductivity of the snow, firn and ice. Thicker ice provides increased insulation from the cold athmosphere and facilitates higher basal temperatures. Internal heat sources, such as strain or basal frictional heating, ice advection and water flow modify the temperature profile. Strain heating is highest near the glacier base, where the shear stress is at its maximum. The PMP at a certain depth is determined by the local pressure field.

At the glacier surface, ice-surface and surface-air temperature needs to be balanced. This is achieved by changes in snow/ice temperature, partial freezing of liquid water or melting of snow/ice, respectively. Consequently, the upper part of the ice column is subject to seasonal temperature variations that vanish with depth. As a rule of thumb, the temperature in 10–20 m depth corresponds to the annual mean surface temperature (Paterson, 1994). However, in regions where refreezing of meltwater/rain is significant, such as in the firn and SI area, near-surface temperature may be much higher and reach the melting point by the end of the summer melt season. During the winter, the cold content is recharged.

2.3 Glacier flow

Glacier flow can be regarded as a mechanism of the glacier to seek or maintain equilibrium with the present climate. The ice flux required to maintain a steady-state surface profile is termed the 'balance flux'. It implies that the annual ice flux through the cross-section located at the ELA, equals the mass gain of the accumulation area during one balance year. Glacier flow constitutes two components: internal deformation and basal motion. Fast glacier flow is only facilitated by basal motion that, if enabled, allows for much higher flow velocities than plastic deformation. Glacier response to changes in accumulation and ablation may last for several decades or even centuries. A response to changes in the basal thermal regime or hydrology may act on short timescales of ∼1 day–1 year. Such intrinsic processes provide possible mechanisms for surge-type behaviour.

2.3.1 Creep deformation

Creep refers to time-dependent, gravity-driven, plastic deformation of glacier ice. A material or constitutive equation relates strain rates to the applied stress and accounts for the rheology of ice. Ice is regarded as an incompressible, heat conducting power-law fluid. The most commonly used relation is 'Nye's generalization of Glen's flow law':

$$\dot{\varepsilon_{ij}} = A(T', p){\tau_{\text{eff}}}^{n-1}\sigma'_{ij}, \tag{2.5}$$

where $\dot{\varepsilon_{ij}}$ are the nine strain-rate components associated with a three-dimensional orthonormal basis ($i, j \in$ [x,y,z]), σ'_{ij} the components of the stress deviator, respectively, and

τ_{eff} the effective stress. The flow-law/stress exponent, n, is usually set equal to 3. The stress deviator is defined as the total stress less the hydrostatic pressure:

$$\sigma'_{ij} = \sigma_{ij} - \frac{1}{3}\delta_{ij}(\sigma_{\text{xy}} + \sigma_{\text{xz}} + \sigma_{\text{yz}}). \tag{2.6}$$

The effective stress follows from the second invariant of the stress deviator

$$\tau_{\text{eff}}{}^2 = \frac{1}{2}(\sigma'_{\text{xx}}{}^2 + \sigma'_{\text{yy}}{}^2 + \sigma'_{\text{zz}}{}^2) + \sigma'_{\text{xy}}{}^2 + \sigma'_{\text{xz}}{}^2 + \sigma'_{\text{yz}}{}^2. \tag{2.7}$$

The rate factor, $A(T', p)$, accounts for the thermomechanical coupling and dependent on the temperature relative to PMP, $T' = T - T_{\text{PMP}}$, and pressure, p, following an Arrhenius law

$$A(T', p) = A_0 e^{-Q/RT'}. \tag{2.8}$$

Different pre-exponential constants, A_0 and activation energies, Q, are recomended for temperatures below or above $T' = 263.15\,\text{K}$. $R = 8.314\,\text{J}\,\text{mol}^{-1}\,\text{K}^{-1}$ is the universal gas constant. Effects of impurities or anisotropy, i.e. the dependence of strain on the direction of the applied stress are not accounted for. There are efforts towards developing new constitutive equation, e.g. by Goldsby and Kohlstedt (2001), that suggest at least four mechanisms for creep flow, each one being associated with characteristic flow-law exponents and activation energies.

2.3.2 Basal motion

Fast glacier flow is achieved by basal motion rather than by internal deformation and requires basal temperatures at or near the pressure-melting point. Basal motion refers to sliding of the ice base over bedrock (Clarke, 1987) or deformation of subglacial sediments (Clarke *et al.*, 1984; Tulaczyk *et al.*, 2000a). Basal sliding over bedrock protrusions may involve regelation or enhanced flow. Regelation dominates flow over small ($<$1 m) obstacles and refers to excess-pressure melting on the stoss side of bumps and subsequent lee-side refreezing of melt water. Regelation is enhanced in the presence of subglacial sediment grains or rock fragments that attract a thin liquid layer adjacent to them (Gilpin, 1979). Enhanced flow is the primary mechanism for flow over large obstacles ($>$1 m) and associated with local rises in basal shear stress and hence, strain rates. Basal sliding is generally considered minimal and negligible, incase of a cold glacier bed frozen to the ground. However, Shreve (1984) showed that regelation may take place at subfreezing temperatures, albeit at very small rates.

The relation between basal motion and effective basal normal pressure, i.e. ice overburden reduced by basal water pressure, explains much of the variations on shorter timescales (hours to weeks) (Meier and Post, 1987). Excessive charge of the subglacial hydrological drainage system early in the summer melt season reduces the effective normal pressure which in turn weakens the ice-bed coupling (Iken and Bindschadler, 1986) and promotes high velocities in excess of those during winter. Early in the melt season, the basal drainage system is hydraulically inefficient and characterized by a system of interconnected cavities. A particularity of such a drainage system is that basal water pressure increases with water discharge (Walder, 1986) and consequently, water is distributed along the ice-bed interface, effectively weakening the ice-bed coupling over a large area. Given sustained input of meltwater, a hydraulically efficient drainage system consisting of large 'Röthlisberger' channels may evolve later in the melt season (Iken *et al.*, 1983; Mair *et al.*, 2001). The effective normal pressure increases and the bed-coupling strengthens. If overcharged, a channelized system may also respond with increased water pressure, but typically, water pressure is low (Röthlisberger, 1972). Recent observations underpin that a simple linear relation between surface melt and glacier acceleration does not exist. Sustained input of large volumes of meltwater may hamper rather than enhance glacier motion, as recently observed in SW Greenland (Sundal *et al.*, 2011), if it permits transition from a hydraulically inefficient to an efficient drainage system in the first place. Model results confirm that a switch in the characteristics of the basal drainage system can explain such observations (Schoof, 2010b). Enhanced ice-surface velocities following surface melt was reported not only for temperate glaciers, but also for the Greenland ice sheet (Zwally *et al.*, 2002) and several Arctic glaciers with polythermal/predominately cold thermal regimes (Copland *et al.*, 2003; Rippin *et al.*, 2005; Nuttall and Hodgkins, 2005). Velocity variations not only arise from effects of the subglacial hydrology. Significant calving events at the marine terminus (Thomas, 2004) or buoyancy perturbations due to ocean tides (O'Neel *et al.*, 2003) may change the backstress exerted on the upglacier ice through longitudinal stress coupling to marginal ice, indicating that non-local forces may influence the velocity at a particular location (Price *et al.*, 2008; Nick *et al.*, 2009).

Sliding laws provide a quantitative relation between basal motion and the controlling factors: the driving stress, the basal thermal regime, the basal water pressure, the bedrock lithology and the characteristics of the sediment layer, if present. A modified Weertman-type sliding law is used in this thesis (Paper III) and introduced in Section 5.2.

2.4 Surge behaviour

Surge-type glaciers are characterized by an oscillatory mode of equilibrium and do not maintain a steady mass flux that equals the theoretical balance flux to maintain a steady-state surface profile (Clarke, 1987). Instead, their dynamics are characterized by a long quiescent phase of inefficient ice flow, undershooting the balance flux, and a short-lived surge phase of super-efficient ice flow, greatly overshooting the balance flux. During the quiescent phase, the glacier can be divided into an active thickening zone, the 'reservoir zone', and an almost stagnant depleted zone, the 'receiving zone', separated by the dynamic balance line (DBL) (Meier and Post, 1969; Dolgoushin and Osipova, 1975). The reservoir and receiving zones do not usually coincide with the glacier's accumulation and ablation zones, instead the DBL marks a boundary zone where glacier outflow is restricted (Clarke *et al.*, 1984). The distribution of mass from the reservoir zone into a receiving zone during the surge may be accompanied by a significant advance of the terminus (Meier and Post, 1969).

Both cold and temperate glaciers can surge, but the ice base must be at PMP during the active surge phase in order to allow for high basal velocities (Clarke, 1987; Murray *et al.*, 2000). Changes in the basal-thermal or basal-hydraulic regime have been suggested as triggering the abrupt onset of a surge (Clarke and Blake, 1991; Kamb, 1987). Kamb (1987) and Raymond (1987) discussed implications of different basal drainage systems and pointed out that a highly pressurized system of linked cavities may facilitate fast flow and prevail during a surge, while a switch to a hydrologically efficient channel system reduces the basal water pressure and may cause surge termination. The surge termination often coincides with an exceptional peak in water and sediment flux (Björnsson, 1998). Clarke *et al.* (1984) suggest the presence of highly-deformable, water-saturated sediments as an alternative explanation of highly enhanced basal motion. Basal motion of polythermal ice bodies is spatially and temporarily restricted to basal areas at PMP. The cold basal areas are frozen to the ground and basal motion is prohibited. Therefore, the thermal evolution of the bed plays a decisive role.

The occurrence of surge-type glaciers worldwide is spatially limited to several clusters, suggesting that certain regional conditions favour surge behaviour (Hamilton and Dowdeswell, 1996). Surging glaciers are very common on Svalbard (Liestøl, 1969; Lefauconnier and Hagen, 1991; Hagen *et al.*, 1993; Sund *et al.*, 2009). Statistical model results indicate a thermally controlled soft-bed surge mechanism with largest surge probability for polythermal glaciers resting on unlithified or easily erodible beds (Jiskoot *et al.*, 2000).

Although surge behaviour is not climatically controlled, i.e. it may occur under constant climate conditions, changes in the net mass accumulation affects the built-up time of the reservoir area and may thereby influence the period of the surge cycle. This is reflected in regional differences in surge periodicity. For Svalbard glaciers, both the duration of the active surge phase (3–10 a) and the quiescent period (50–500 a) is long (Dowdeswell *et al.*, 1991) compared to surges in other areas, e.g. SE-Alaska (Eisen *et al.*, 2005). Surge behaviour complicates projections of sea level rise into the future. On Svalbard, thickening at higher elevations is observed despite regional glacier net loss (Nuth *et al.*, 2010).

3 The Austfonna Ice Cap

The Austfonna ice cap constitutes the largest individual glacier on the highly glaciated archipelago of Svalbard (Fig. 3.1). This chapter adverts to previous research activities that are of particular relevance to this thesis and summarizes their findings. In addition, an overview of the geographical setting of Austfonna, the Svalbard archipelago, and a brief account of the exploration of Austfonna are provided. The description of present-day Austfonna overlaps with the corresponding paper sections, section I.2 with focus on the SMB, section II.2 concentrating on the ice surface motion and section III.2 with respect to ice geometry, thermal structure, ice flow and basal properties.

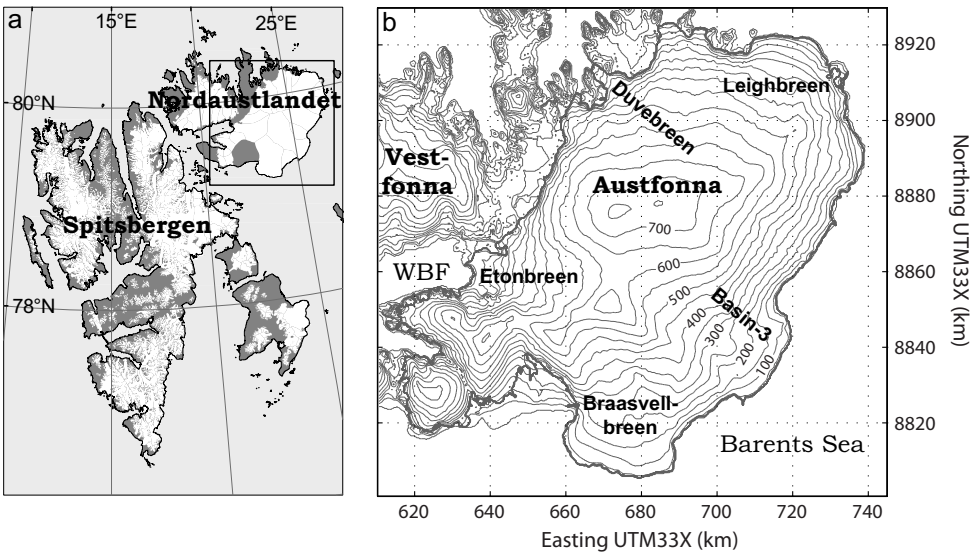

Figure 3.1: Map of Svalbard (a) and the Austfonna ice cap on Nordaustlandet (b).

3.1 Geographical setting on Svalbard

Svalbard is an archipelago in the Eurasian Arctic. Located north of mainland Norway at 76–81° N and 10–35° E, it lies between Greenland in the west and the Russian archipelagos Franz Josef Land and Novaya Zemlya in the east. Svalbard comprises four major islands: Spitsbergen being the largest, followed by Nordaustlandet in the northeast and Edgeøya and Barentsøya in the southeast. Spitsbergen is characterized by rugged mountain regions, while the eastern islands are comparably flat.

Despite the archipelago's high arctic location, the climate is relatively mild, due to its marine setting and surrounding oceanographic conditions. A branch of the Gulf Stream, the 'West Spitsbergen current', enters the Arctic basin through the eastern side of the Fram Strait between Svalbard and northern Greenland. The Arctic Ocean to the north and the northern Barents Sea off the eastern flank of Svalbard are dominated by cold and light Arctic water masses, i.e. water with low salinity (Loeng, 1991) and cold polar air masses (Isaksson *et al.*, 2005). The northeast is therefore more affected by perennial sea ice, reducing the moisture flux from the ocean during the winter. There is thus a spatial trend from milder marine climate in the southwest to more harsh Arctic conditions in the northeast. A pronounced high-pressure over the Arctic Ocean give rise to a frequent weather type associated with cold easterly or northeasterly winds (Isaksson *et al.*, 2005). The Svalbard region is one of the major gateways for atmospheric heat and moisture flux into the Arctic. During the winter months, the Icelandic low and an associated broad band of low pressure extend far into the Arctic forms a dominant feature (Serreze *et al.*, 1997), creating favorable conditions for the development of cyclones (Tsukernik *et al.*, 2007). These cyclones may be associated with significant temperature changes of $\gtrsim 20$°C, within a few hours, and rainfall may occur everywhere on Svalbard, even in winter.

Direct meteorological observations date back until 1911, but are spatially limited to locations in central Spitsbergen (Nordli and Kohler, 2004). The temperature record shows a pronounced warm period during the 1920–30s followed by a cold spell in the 1960s. During the last ∼5 decades, the temperatures were steadily rising. According to the data provided by the Norwegian Meteorological Institute (met.no), the average annual temperature in Longyearbyen, central Spitsbergen, for the time period 1961–90 was –6.7°C with February being the coldest (–16.3°C) and July the warmest month (5.8°C). Ice core analysis revealed that present temperatures reached a level unprecedented in at least the last 600 years (Isaksson *et al.*, 2005). During the instrumental record, precipitation over Svalbard has increased by about 25% (Førland *et al.*, 1997). Despite the principle storm

tracks from the North Atlantic, most precipitation is brought by more frequent easterly winds. This is also reflected in the distribution of the snow accumulation, with a general decrease from east to west and from south to north, with a pronounced minimum in the central, more continental parts of Spitsbergen (Winther *et al.*, 1998; Sand *et al.*, 2003).

About 34600 km^2 or 60% of Svalbard are covered by glaciers (Hagen *et al.*, 1993), which is about 4–6% of the worldwide area covered by glaciers other than the ice sheets of Greenland and Antarctica. Glaciers on Svalbard have contributed about $9.5 \pm 1\,km^3$ w.e. a^{-1} over the past decades (Nuth *et al.*, 2010). The most common form of glaciers on Spitsbergen are extensive ice fields interrupted by mountain ridges and nunataks, as well as smaller valley and cirque glaciers. The eastern islands are dominated by large ice caps of which Austfonna ($\sim$8000 km^2) and Vestfonna ($\sim$2400 km^2) on Nordaustlandet constitute the two largest ones. Svalbard glaciers seem to have been at maximum extent in the beginning of the 20th century, just prior to the early 20th century warming and interrupted only by occasional surge advances (Hagen *et al.*, 1993). The glaciers are generally polythermal (Macheret *et al.*, 1991; Björnsson *et al.*, 1996) and many of them of surge-type (Liestøl, 1969; Schytt, 1969; Lefauconnier and Hagen, 1991). Flow of land-terminating glaciers are generally low, typically less than 10 m a^{-1} due to low ice temperatures and accumulation rates, usually less than 1 m a^{-1} w.e. (Hagen *et al.*, 2003). Glaciers terminating into the sea are usually flowing much faster, up to an annual mean of 1.5 m d^{-1} in the case of Kronebreen, a tidewater glacier at the head of Kongsfjorden near Ny-Ålesund (Lefauconnier *et al.*, 1994). The total length of the calving front for the entire archipelago adds up to about 1000 km (Hagen *et al.*, 2003). All marine ice margins are grounded, i.e. floating ice margins do not exist (Dowdeswell, 1989). The area not covered by glaciers has permafrost with variable thickness ranging from less than 100 m at the coast to more than 500 m in mountain areas (Liestøl, 1976; Humlum *et al.*, 2003).

3.2 From discovery to modern research expeditions

The demand for whale oil as a combustible spurred whaling in Svalbard since the early 17th century. Not surprisingly, first sightings of the coast of Nordaustlandet were made by English and Dutch whalers. A first complete outline of Nordaustlandet was drawn in a map published by Van Keulen in the beginning of the 18th century. Commanders Giles and Reps noted that the inland ice extends into the sea along the eastern coast of Nordaustlandet. In 1827 Captain Parry explored the northern part of the Hinlopen Strait and the northwestern part of Nordaustlandet. However, it was not before 1871 that the

true extent of eastern Nordaustlandet was determined by Leigh Smith by determining the positions of the northeastern and southeastern corner. In 1873, the Swedish explorer Nordenskjöld attempted to push as far north on the sea ice, as possible. Difficult sea ice conditions forced him eastwards, along the northern coast of Nordaustlandet, and finally southwards, onto the inland ice. He and his men were the first to cross the Nordaustlandet ice caps. Nordenskjöld's expedition coincided with the culmination of the Little ice Age and consequently, he observed no signs of surface melt (Leslie, 1879; Nature 20, 1879). He reported that the eastern part of Austfonna forms a continuous and vertical calving front, while the northern parts mainly terminate on land. He assumed the inland ice being at rest, except for certain streams that terminate into the sea. In the eastern part of Austfonna, Nordenskjöld discovered a regular pattern of 10 m deep and 10–30 m wide fissures. He suggested, these fissures were due to thermal expansion and contraction of the ice. What he might have observed, however, was the highly crevassed surface of Basin-3, after a surge prior to his expedition (Lefauconnier and Hagen, 1991).

The English Oxford University expedition in 1924 can be regarded as the first well prepared scientific expedition to Nordaustlandet. Its objectives were to study the glaciological conditions of the Nordaustlandet ice caps, the geology of the ice-free land outcrops, as well as the meteorological and oceanographic conditions of the area (Binney, 1925). In contrast to Nordenskjöld's expedition, the advance of their sledge journey was hampered by intense summer melt. The expedition coincided with the 1920s warm period and was furthermore performed in late in summer. Sandford (1929) noted that the snow transformed in a mass of slush, which, later in autumn, freezes and adds to the ice mass of the glacier. The oceanographic survey circumnavigated the island and confirmed that the entire eastern, southeastern parts of Austfonna terminates in an ice cliff 15–30 m high and more than 160 km long, forming one of the longest calving fronts of the Arctic. He suggested that the submerged ice regions are aground on a sedimentary bed, as clay was observed to cover the seafloor in close vicinity to the ice front which was interrupted only by a small granite outcrop at Isis Point. Sandford also suggested that most of the ice cap is stagnant, with marked movement limited to certain areas such as the 'Eton-depression'. Etonbreen was characterized by a maze of crevasses, calving large icebergs into Wahlenbergfjord. In contrast to the eastern, southeastern marine margin, Etonbreen appeared to be afloat along its central flowline.

The Swedish-Norwegian Expedition to Nordaustlandet in summer 1931, made a great effort to investigate the mass balance regime of both Vestfonna and Austfonna (Ahlmann and Rosenbaum, 1933). Based on numerous snow and firn pits along their ice-cap tra-

verses, maps of accumulation and ablation were drawn (Ahlmann *et al.*, 1933b,a). An intermediate zone was identified, reflecting the year-to-year variability in surface mass balance. The objectives of the inland expeditions further included meteorological conditions, shallow snow/firn and ice temperatures, characteristics of surface melt and runoff and a topographic survey. Based on topographic features of the ice surface and the height of ice-free land, Ahlmann assumed a large plateau with elevations in excess of ∼400–450 m underneath the ice caps. The ice thickness was thus believed to be $\lesssim$ 200 m (Ahlmann *et al.*, 1933b). Another Oxford University expedition in 1935-36 spend 14 months on Nordaustlandet (Glen, 1937). Two ice cap stations were established on Vestfonna, in addition to the main station at the coast, northwest of the ice cap. The ice cap stations allowed for continuous observations of the meteorological and glaciological conditions on the ice cap, including precipitation and ablation, wind drift, snow metamorphism and the transition from snow to ice (Glen, 1939).

In 1938, the Norwegian Polar Institute (NPI) did an airborne topographic survey to derive a 1 : 100 000 scaled map of Nordaustlandet (Luncke, 1949). A strongly crevassed glacier tongue was found to extend beyond the old coastline in the southeast and named Bråsvellbreen. In addition, Etonbreen in the west had advanced considerably. Both advances were accompanied by a general subsidence of the ice-surface and appeared to be in no relation to the present mass balance (Glen, 1939). It was first after the second world war, that two Oxford University expedition lead by Hartog in 1949 and 51 investigated the post-surge Bråsvellbreen (Thompson, 1953). Surface crevasses had closed up and were

Figure 3.2: German wartime weather station 'Haudegen' anno 2008.

replaced by sub-parallel lines of an hummocky ice surface. The height of the ice cliff was measured and the terminus concluded to be aground. Thermal drilling to a depth of ∼25 m showed that the ice was cold, $< -5\,^{\circ}\mathrm{C}$.

During the war, in 1944–45, a German weather station was established in Rijpfjorden at the northcoast of Nordaustlandet with the pseudonym 'Haudegen' (Dege, 1946, 1947, Fig. 3.2). The meteorological observations recorded frequent cyclone activity, causing warm events during the winter months. Strong winds during winter storms changed the characteristics of the snow-surface fundamentally and within hours. Daily ascends of radiosondes revealed strong and frequent temperature inversion during stable winter-weather situations. Involuntarily, the battalion lead by W. Dege became the last one to surrender after victory of the Allies over Germany. They were evacuated in September 1945 by a Norwegian sealer (Dege, 1954).

The Swedish glaciological expedition under the framework of the International Geophysical Year 1957-58 brought the scientific investigation of Nordaustlandet to a modern standard. Systematic measurements were made during two consecutive summer seasons (Schytt, 1964). A number of 75 snow pits was used to refine previous surface-mass-balance maps. The total mass turn over in terms of accumulation and ablation was found one order of magnitude larger then previously reported. The mass balance was estimated to be close to balance, but being characterized by a large year-to-year variability. A seismic survey disproved the concept of thin ice caps resting on a plateau (Ekman, 1971). Instead, Austfonna was found to rest on a low, undulating bed with ice thicknesses up to ∼600 m. At several locations, a secondary reflection was visible in the seismograms and interpreted to be associated with subglacial till.

3.3 Geometry

Centered at 79.7° N and 24° E, Austfonna occupies the eastern part of the island Nordaustlandet (Fig. 3.1) covering an area of approximately 7800 km^2 (Moholdt *et al.*, 2010b). The ice cap and consists of a main central dome that merges with a smaller dome to its south, feeding a number of drainage basins. A main ice divide oriented southwest-northeast forms a natural border between the northwestern basins, predominately terminating on land or in fjords, and the southeastern basins that form a continuous calving front toward the Barents Sea. Surface elevation and ice thickness has been extensively mapped by airborne radio-echo sounding (RES) in 1983, and revealed the bed topography beneath the ice (Dowdeswell, 1986). The maximum elevation of about 800 m a.s.l. in the central

Figure 3.3: The marine ice margin of Basin-3.

part coincides with the maximum ice thickness of about 580 m (Dowdeswell, 1986). Over 28% of the area covered by Austfonna lies below sea level, especially the southeastern basins (Dowdeswell, 1986). The calving margins (Fig. 3.3) add up to a total length of 230 km (Dowdeswell *et al.*, 2008). The deepest depressions reach more than 150 m below sea-level and are found below the lower reaches of Basin-3 and Leighbreen.

3.4 Mass Balance

Pinglot *et al.* (2001) inferred the annual mean SMB of the accumulation area of Austfonna for the period 1986 to 1998/1999 from shallow ice cores dated by the detected radioactive fallout horizon from the Chernobyl accident. Maximum values of $\sim$0.5 m w.e. a^{-1} were measured in the summit area. Taurisano *et al.* (2007) mapped the winter snow cover using GPR data collected in spring 1999, 2004 and 2005. As Pinglot *et al.* (2001), they found an asymmetry in SMB, in accordance to the distribution of snow, with twice as much accumulation in the southeast than in the northwest. Both studies conclude that this pattern results from the proximity of the Barents Sea in the east, southeast, providing a significant moisture source for precipitation. Taurisano *et al.* (2007) related snow thickness to all three spatial coordinates by multiple regression to derive an accumulation index map. The distribution of snow across Austfonna is thus relatively well understood, whereas the fate of the snow throughout the summer-melt season is only known at a few points from shallow cores and mass balance stakes. A SMB model by Schuler *et al.*

(2007) supported previous observations that internal accumulation and superimposed ice formation contribute significantly to the net accumulation. Geodetically derived mass balance over the time period $2002 - 2008$ suggests an SMB close to zero (Moholdt *et al.*, 2010a). However, the total mass balance of Austfonna is negative, $-1.3 \pm 0.5\,\mathrm{km^3\,a^{-1}}$, due to significant retreat of the marine margins (Dowdeswell *et al.*, 2008; Moholdt *et al.*, 2010a).

3.5 Dynamics

Space-borne radar interferometry of Austfonna revealed a velocity structure of a slow-moving Arctic ice cap ($< 10\,\mathrm{m\,a^{-1}}$) interrupted by distinct fast flow units having velocities in excess of $100\,\mathrm{m\,a^{-1}}$ (Dowdeswell *et al.*, 1999). These snapshots represent a period in the mid 1990's, the time when suitable satellite data was acquired. Several of the drainage basins have been observed to surge, namely Etonbreen (in 1938), Bråsvellbreen (in 1937/38) and Basin-3 (a few years prior to 1873 (Lefauconnier and Hagen, 1991); see Fig. III.1. The surge of Bråsvellbreen is one of the largest ever observed. The 30 km wide front advanced about 20 km (Schytt, 1969). The known surge-type basins are characterized by low driving stresses and low ice-surface profiles that fall below theoretical steady-state surface profiles, as expected for glaciers in an early quiescent phase (Dowdeswell, 1986). Basins with relatively high shear stresses close to the margins and actual ice-surface profiles above the steady-state surface profiles are interpreted to be frozen to their beds and may be of surge-type, too, especially if they contain ice regions grounded below sea level (Dowdeswell, 1986). Macheret *et al.* (1991) note that thermal state and conditions at the ice-bed interface have a significant effect on the mechanical stability of polythermal glaciers on Svalbard and determination of surge mechanisms. Recent observations indicate that the interior of Austfonna is thickening at a rate of approximately $0.5\,\mathrm{m\,a^{-1}}$ while the margins are thinning at a rate of $1\text{–}3\,\mathrm{m\,a^{-1}}$ (Moholdt *et al.*, 2010a). Such changes are potentially attributed to a build-up during a quiescent phase. Bevan *et al.* (2007) suggested that slow ice motion is the key factor for the interior thickening, since the actual ice flux across the equilibrium line appeared to be only half of the theoretical balance flux across the equilibrium line. Changes in the accumulation-ablation pattern due to a loss of perennial sea-ice cover in the Barents Sea have been suggested as alternative mechanism of the observed geometric changes (Bamber *et al.*, 2004). However, this is not supported by observation of SMB that do not indicate a significant trend in snow accumulation prior

to 2002, although large interannual variations in snow accumulation and SMB have been observed in recent years (Taurisano *et al.*, 2007).

3.6 Thermal Regime

Austfonna's thermal regime is described as polythermal (Dowdeswell *et al.*, 1986). In the firn area, latent heat release from internal refreezing of surface generated meltwater contributes significantly to warming the near-surface firn and ice. Current near-surface temperatures (at 10 m depth) in the firn area are $> -3°C$ and exceed those in the ablation area, despite lower air temperatures. Direct measurements of the temperature distribution throughout an entire ice column is available from a borehole at the summit area, drilled in 1987 (Zagorodnov *et al.*, 1989a). The vertical temperature profile shows that the bulk of the 567 m thick ice column is cold, underlain by an isothermal basal layer of approximately 30 m thickness at $-1.2°C$, which is close to PMP, corresponding to $-0.42°C$. A temperature minimum of $-8°C$ at $\tilde{1}60$ m depth at the drilling site is associated with lower temperatures during the Little Ice Age around 1860, when firn warming presumably was insignificant (Zagorodnov *et al.*, 1989b). The temperature gradient in the lower 400 m suggest a moderate geothermal heat flux of approximately $40\,\mathrm{mW\,m^{-2}}$ (Ignatieva and Macheret, 1991). Information on the thermal structure of the ice cap is also contained in the airborne RES data (Macheret *et al.*, 1991). An internal reflection horizon (IRH), separating a transparent zone above and a zone of high back-scatter below, may be associated with the CTS. Such IRHs are characteristic for many glaciers in Spitsbergen/western Svalbard (Björnsson *et al.*, 1996). The Institute of Geography, USSR Academy of Sciences, collected such data in 1984 (Macheret and Vasilenko, 1988). Similar to the RES data published by Dowdeswell *et al.* (1986) the absence of a continuous IRH indicates that significant volumes of temperate ice do not exist. A thin basal layer of temperate ice may not be resolved by the radar system and the absence of continuous IRHs does not exclude basal melt and the occurrence of water at the ice-bed interface (Kotlyakov and Macheret, 1987; Macheret and Vasilenko, 1988). The vanishing of bedrock returns in some regions, such as Leighbreen, may indicate the presence of a localized basal temperate layer. A simple theoretical consideration leads to a similar result: given a constant temperature gradient determined by the geothermal heat flux, an ice thickness of more than 500 m, which is about the maximum ice thickness of the ice cap, is required to approach PMP if internal strain heating is neglected (Fig. 5.7). Without significant contribution from strain heating or latent heat release by infiltrating surface meltwater, the bulk of the ice cap

is expected to be cold, but potentially underlain by a temperate base. Results from the Russian ice cores indicate that bottom melting takes place below the summit (Kotlyakov *et al.*, 2004). The age of the ice was estimated to not exceed 3500–4000 a (Zagorodnov and Arkhipov, 1990).

3.7 Basal Conditions

Turbid meltwater plumes arising from several points beneath the marine ice margin of Austfonna provide evidence that the marine grounded areas are, at least to some extent, underlain by soft sediments and subjected to basal water flow (Macheret and Vasilenko, 1988; Dowdeswell *et al.*, 1999). Furthermore, Solheim and Pfirman (1985) and Solheim (1986) mapped continuous submarine sediment ridges in front of Bråsvellbreen and Basin-3 and conclude that these ridges were partly pushed up by the advancing surge front, partly deposited by vigorous meltwater drainage along the entire surge front during the period of maximum extension. A rhombohedral pattern of linear, discontinuous sediment ridges and mounds is interpreted as formed by a squeeze-up process, filling bottom crevasses that opened during surge advance. After surge termination, the surge lobe was stagnant, preserving subglacial features. The presence of sediment-rich layers outcropping at the front of Etonbreen are presumably related to the drainage of sediment-rich basal water through englacial faults. Englacial sediment layers have also been found on Bakaninbreen and interpreted to be associated with the surge termination Murray *et al.* (2000). These sediments may originate from glacial erosion of the underlying bedrock and/or marine sedimentation during periods when the glacier extent was considerable smaller than today, e.g. the Holocene Optimum ca. 9000 to 5000 years ago (Hjort *et al.*, 1995; Blake, 2006). Glacier extent was also reduced during interstadials of the last glacial period, as evident in sediment cores off the margins of Vestfonna (Kaakinen *et al.*, 2009) and in Franz Victoria Trough, northeast of Nordaustlandet (Kleiber *et al.*, 2000). A geological map of Nordaustlandet published by the Norwegian Polar Institute indicates that an E-W line along Wahlenbergfjord separates hard bedrock types in the north, i.e. Late Precambrian Hecla Hoek rocks and Caledonian granite-migmatide complexes, from soft bedrock types in the south, i.e. flat lying young sediments of Middle Carboniferous to Lower Cretaceous age (Lauritzen and Ohta, 1984). Information on bedrock type for presently glacierized areas is not available but it is noteworthy that the known surge-type basins Etonbreen and Bråsvellbreen are located adjacent to the soft, easily erodible bedrock types. Most of the 80−100 m uplift (60−80 %) that occurred after the decay of the Late Weichselian

ice sheet over Svalbard and the Barents Sea was accomplished at that time (Salvigsen, 1978; Landvik *et al.*, 1998) and large parts of the bedrock areas currently below sea level have presumably been exposed to marine and glacial sedimentation over significant time periods.

4 Geophysical Methods

4.1 Ground-Penetrating Radar

Ground-penetrating radar (GPR) has found broad application in the field of glaciology since the early 1960s. Applications include mapping of the ice thickness (Evans, 1963), investigation of the internal structure and thermal regime (Macheret and Vasilenko, 1988; Jacobel and Hodge, 1995), the spatial variability in snow accumulation (Kohler *et al.*, 1997; Richardson-Näslund and Holmlund, 1999; Sinisalo *et al.*, 2003; Taurisano *et al.*, 2007) or the influence of melt on the near-surface snow and firn structure (Jezek *et al.*, 1994; Kanagaratnam *et al.*, 2001; Dunse *et al.*, 2008). A detailed account on the principles and application of radar in the field of glaciology can be found in e.g. Bogorodsky *et al.* (1985); Dowdeswell and Evans (2004) and only a brief introduction is given here.

4.1.1 Principle

GPR is an active remote-sensing technique and involves radio frequencies ranging of the order from 1 MHz–10 GHz, the particular choice being a trade-off between the desired system resolution and penetration depth. A transmitting antenna is excited by a voltage pulse. An electromagnetic (EM) wave propagates through a medium and part of its energy is reflected at inhomogeneities with respect to the medium's EM properties. Phase and amplitude of the reflected signal are detected by a receiving antenna as a function of two-way travel time (TWT). If the velocity of the EM wave v_{EM} is known, TWT can be converted to the range, R, the distance to the object/interface at which the reflection originates,

$$R = \frac{1}{2} v_{\mathrm{EM}} \,\mathrm{TWT}. \tag{4.1}$$

In air, EM waves travel at approximately the speed of light in vacuum, $\mathrm{c} = 0.2998\,\mathrm{m\,ns^{-1}}$. EM wave speed, energy attenuation and reflection are controlled by the medium's complex electromagnetic properties, generally expressed relative to those of the vacuum. The electromagnetic properties are described in terms of the complex magnetic permeability

μ^* and the complex dielectric constant ε^*. The dielectric constant comprises a real part, the relative permittivity of the medium, ε', as well as an imaginary part, which can be described in terms of the electric conductivity.

An interface separating two media with different electromagnetic properties gives rise to an internal reflection horizon (IRH). Radar measurements from moving platforms allow to track IRHs along continuous profiles.

4.1.2 Propagation of electromagnetic waves in snow and ice

Snow and ice are non-magnetic and their relative magnetic permeability equals 1. The electromagnetic properties are therefore determined by the dielectric constant. Electromagnetic energy suffers rapid attenuation in wet snow, severely limiting the penetration depth of the radar signal. In dry polar snow and ice, effects of liquid water are negligible, allowing for deep penetration of radar signals ranging from several meters to kilometers, depending on the radar frequency. The EM-wave velocity, v, can be estimated by

$$v = \frac{c}{\sqrt{\varepsilon'}}. \tag{4.2}$$

Reflections from within cold snow and firn are mainly attributed to variations in permittivity ε' and strongly related to changes in density, ϱ (Tiuri *et al.*, 1984; Wolff, 2000). The permittivity of snow and ice can be estimated using empirical formulas such as that of Kovacs *et al.* (1995), which relates permittivity to density:

$$\varepsilon' = (1 + 0.000845\varrho)^2. \tag{4.3}$$

Given a vertical density profile, the recorded traveltime can be converted to depth.

Reflections from pure ice at greater depth are dominated by variations in conductivity and may be related to buried volcanic ash layers (Paren and Robin, 1975). Volumes consisting of a mixture of materials with different dielectric properties give rise to volume scattering, e.g. snow and firn comprising solid ice inclusions or temperate ice, a mixture of ice and liquid water.

4.1.3 Applied GPR systems and set-up

In this thesis, I use an impulse-radar system (RAMAC, Malå GeoScience) operating at a center frequency of 800 MHz to map snow accumulation and to retrieve information of the near-surface snow, firn and ice structure (Paper I). A GPS (GNSS) receiver was operated

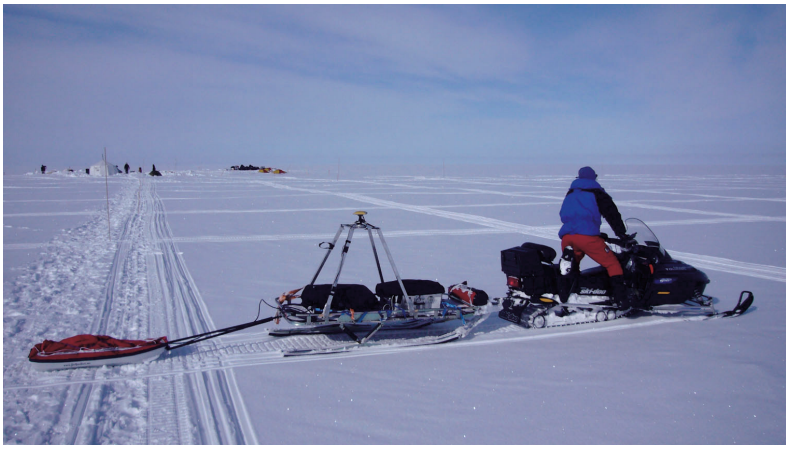

Figure 4.1: Setup of 800 MHz GPR and kinematic GNSS. The shielded GPR antennae are mounted on the rearmost sledge, the GPR control unit and laptop along with the GNSS receiving unit mounted on the main sledge pulled by a snow mobile. The summit camp is visible in the background.

together with the GPR for simultaneous kinematic positioning. The GPR control unit and the GPS system were mounted on one sledge, the GPR antennae on a separate sledge made of fibre glass, and pulled by a snowmobile (Fig. 4.1). A driving speed of about $5\,\mathrm{m\ s^{-1}}$ and a constant triggering rate of the GPR resulted in a trace interval of 0.25 to 0.30 m. The receiving timewindow was set to 145 ns in 2007 and 126 ns in previous years, in order to image a depth range of >10 m. Every trace consists of 1024 samples corresponding to a sample interval of 0.14 ns and 0.12 ns respectively.

Furthermore, a 20 MHz GPR system (VIRL-6) is utilized (Paper II,III) to refine bedrock topography and investigate the thermal structure (Vasilenko *et al.*, 2010). GPR measurements were triggered every 2 m by means of an odometer. Navigation data was recorded simultaneously with the GPR data using a GPS Garmin II Plus receiver.

4.1.4 System resolution and accuracy

The GPR system is generally designed such that the center frequency corresponds approximately to the bandwidth. In the case of the 800 MHz GPR, the wavelength λ in firn ($\rho = 600\,\mathrm{kg\,m^{-3}}$) is $\sim$0.25 m. The theoretical resolution of $\lambda/4$ is therefore about 0.06 m. However, this is limited by the length of the transmitted wavelets, comprising 2 cycles (approximately 2.5 ns), as interference of partial reflections from inhomogeneities

within the length of the wavelets occur. The effective interface resolution hence equals the wavelength, which for our domain varies from 0.21 m for glacier ice ($\rho = 900\,\mathrm{kg\,m^{-3}}$) to 0.29 m for windpacked snow ($\rho = 370\,\mathrm{kg\,m^{-3}}$).

The VIRL-6 transmitter generates pulses of 25 ns duration with a center frequency of 20 MHz, resulting in a system resolution of approximately 2 m (assuming a radio-wave velocity of $0.168 \pm 0.0005\,\mathrm{m\,ns^{-1}}$, typical for cold ice). The precision of the ice thickness measurements were estimated to 1.6 m, based on the standard deviation in ice thickness at more than 34000 crossover points from the entire Austfonna survey (personal communication G. Moholdt, Department of Geosciences, University of Oslo, Norway, 2011). The precision represents the error in ice thickness due to the uncertainty in the time measurement (digitization of bedrock reflection). The accuracy in ice thickness is determined when adding an absolute error of about 0.3 % (3 mm per meter ice) to the precision value. This absolute error is related to the uncertainty of radio-wave velocity. For an ice thickness of 350 m this corresponds to an error of about 1 m ($2000\,\mathrm{ns} \times 0.0005\,\mathrm{m\,ns^{-1}}$) yielding an accuracy of the GPR-derived ice thickness of about 2.6 m.

4.1.5 Post-processing and interpretation

Post-processing of GPR data generally aims at increasing the signal-to-noise ratio and thereby enhancing the information content of the recorded radar data. Processing of the 800 MHz data includes static correction, i.e. shifting the first arrival times of the direct wave and frequency filtering of individual traces. In addition, a horizontal filter is applied to neighboring traces to remove constant time-delay clutter and system artefacts. For visualization and interpretation a gain function is usually applied.

Post-processed 800 MHz GPR data allows us to distinguish distinct radar zones that are associated with firn (F), SI and pure glacier ice of the ablation area (GI) underneath the LSS (Fig. 4.2). Interpretation and results are described in detail detail in Paper I.

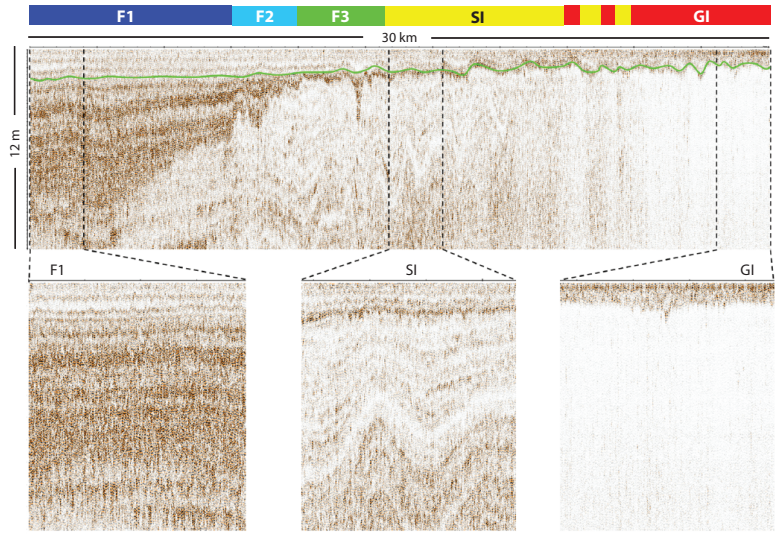

Figure 4.2: Classification of radar zones in 800 MHz GPR data collected along a 30 km transect from the summit area into the ablation area of lower Etonbreen. The green line indicates the position of the last summer surface. The lower panels show close-ups of GPR data from 2 km sections with characteristic reflection pattern indicative for multi-year firn (F), superimposed ice (SI) and pure glacier ice (GI).

4.2 Global Navigation Satellite System

Global Navigation Satellite System (GNSS) is a collective term for satellite navigation systems that provide determination of the geographical position of an electronic receiver in terms of latitude, longitude and elevation relative to a standard datum, e.g. the World Geodetic System WGS84. The United States Global Positioning System (GPS) and the Russian GLObal NAvigation Satellite System (GLONASS) are fully operational. Since 1994, GPS provides more than 24 satellites required for global coverage, GLONASS is about to accomplish this during 2011 (according to a press-release by the Russian Space Forces, ITAR-TASS, 23 Feb 2011). Two other systems are currently under development, the European Galileo and the Chinese COMPASS. A comprehensive account of GNSS is given in textbooks, e.g. Hofmann-Wellenhof *et al.* (2008).

In this thesis, I utilize results from ready-processed kinematic GNSS (GPS and GLONASS; personal communication T. Eiken, Department of Geosciences, University of Oslo, Norway, 2007-11) for accurate positioning of simultaneous GPR measurements

along continuous survey lines (Paper I-III; see Fig. 4.1 for set-up) and raw data collected by continuous GPS for measurement of ice-surface velocity (Paper II).

4.2.1 Principle

GNSS satellites are arranged in several orbital planes with $\geq 50°$ inclination at heights about 20000 km above the Earth surface. The satellites have an orbital period of $\sim$12 hours, repeating the same ground track in 24 hours. Each satellite broadcasts precise orbital information, termed the Navigation message, time of transmission (the "range code"), as well as approximate position and status of all satellites within the system (the "almanac"). The GNSS receiver usually requires information on the position of 4 or more broadcasting satellites to determine its position based on the travel time of the broadcasted signals. Originally intended for military purposes only, precise information of the GPS signals were decoded or artificially degraded, and not open to public applications until the year 2000. Navigation message, ranging code and almanac are transferred by modulation of two separate carrier frequencies, termed the L1 ($\sim$1.6 GHz) and L2 band ($\sim$1.2 GHz). Coarse acquisition of signal travel time is achieved by comparing a pseudo-range signal generated by the receiver, with the code broadcasted by the satellite. The signal travel time equals the time shift required to match both signals. The relatively low frequency of the pseudo-range code ($\sim$1000 MHz) and the high speed of light at which the signal propagates typically inhibits range determination better than within a few meters. Sophisticated receivers make additional use of the high-frequency carrier phase, to fine-tune the signal travel time, enabling a theoretical accuracy of the order of millimeters to centimeters. The positioning is generally enhanced with increasing number of available satellites, an advantage of GNSS receivers that utilize a combination of GPS and GLONASS.

4.2.2 Error sources and corrections

Major error sources include receiver and satellite-clock uncertainties, atmospheric distortions and multi-path error. Several techniques are available to enhance the accuracy of the measurements taking account of the particular objectives (King, 2004). Post-processing capabilities depend on the information that is actually accessed and stored by the receiver.

Charged particles in the ionosphere and water vapor in the troposphere cause a spatially and temporally variable delay of the broadcasted signal. The delay is frequency-dependant and may be corrected for, if information from both the L1 and L2 band are available, as

is only the case for advanced dual-frequency receivers. Alternatively, the signal delay may be simulated by models, given information on particle or gaseous content of the ionosphere and troposphere, respectively. Multi-path error arises when the signal is reflected between local objects and the retarded signal interferes with the signal that reaches the receiver on a direct path. Sophisticated receivers detect and filter out multi-path errors in real-time.

Great enhancement is achieved through differential or relative processing of GNSS data collected of an individual receiver, the 'rover', against simultaneous observations at a reference station, the 'base'. The relative drift of the accurately fixed base position as indicated by the satellite signals can then be used to minimize errors in rover position.

4.2.3 Adopted GNSS

Kinematic GNSS observations were recorded simultaneous to the 800 MHz GPR survey (see set-up in Fig. 4.1). Measurements were logged at a rate of 1 Hz (approx. every 5.5 m) and differentially post-processed using a stationary GNSS as reference (personal communication T. Eiken, Department of Geosciences, University of Oslo, Oslo, Norway, 2007-11), yielding an accuracy of typically better than 5 cm in horizontal position and 10 cm in height (Eiken *et al.*, 1997).

Continuous single-frequency GPS is used to measure ice-surface velocities along the central flowlines of two fast-flowing outlets of Austfonna (Fig. 4.3). The receivers operate unmaintained over time periods of 1 year or longer. The receivers switch on every

Figure 4.3: GPS receiver for continuous positioning deployed on a stake drilled into the ice at lower Duvebreen.

hour for a period of 3 minutes to allow the system to stabilize (personal communication C.H. Reijmer, Institute for Marine and Atmospheric Research Utrecht, Utrecht University, Utrecht, The Netherlands, 2010). Positions are computed within the receiver and only the geographical position and time is logged. Post-processing capabilities are restricted by the limited information stored. Instead, running average filtering of the data is performed to remove high-frequency external disturbances, e.g. caused by atmospheric tides or specific satellite constellation, at the cost of temporal resolution. Based on the standard deviation of the average position of a reference station in central Spitsbergen during $2006 - 2009$, the horizontal accuracy of the system was determined to be 1.62 m (den Ouden *et al.*, 2010). Our measurement period largely overlaps with the period investigated by den Ouden *et al.* (2010) and is characterized by a solar ionospheric minimum. A lower accuracy in the positioning is to be expected in years with higher solar activity.

5 Numerical Modelling

Continuum mechanics and thermodynamics provide the general mathematical framework for numerical models of glacier dynamics (Hutter, 1983; Greve and Blatter, 2009, ; Sec. 2.3). The set of equations to be solved consists of the balance equations for mass, momentum and energy. The system of equations is closed (fully determined) by a constitutive equation that characterizes specific material properties (Sec. 2.5) and suitable boundary conditions. The local balance equations are only valid for physical variables that are continuously differentiable. Otherwise, jump conditions apply, e.g. at the CTS, at which the liquid water content is discontinuous.

5.1 Glacier dynamics

5.1.1 Balance equations

The rheology of ice is that of an linear-viscous heat-conducting fluid, termed a 'Newtonian fluid'. Ice is incompressible and the mass balance reduces to

$$\nabla \cdot \mathbf{v} = 0, \tag{5.1}$$

where $\nabla\cdot$, denotes the divergence and $\mathbf{v}$ the three-dimensional velocity vector. The momentum balance yields the equation of motion and is provided by the Navier-stokes equation for the case of an incompressible Newtonian fluid

$$\rho \frac{\mathrm{D}\mathbf{v}}{\mathrm{D}t} = -\nabla p + \eta \nabla^2 \mathbf{v} + \mathbf{f}, \tag{5.2}$$

where $\mathrm{D}/\mathrm{D}t$, denotes the material time derivative, p is the pressure, η a constant viscosity and $\mathbf{f}$ represents additional body forces. The viscosity of ice is temperature-dependent and an additional energy balance must be solved the:

$$\rho c \frac{\mathrm{D}T}{\mathrm{D}t} = \kappa \nabla^2 T + 2\eta \mathrm{tr}\mathbf{D}^2 + \rho r, \tag{5.3}$$

where c is the specific heat, and κ the heat conductivity of ice, $\mathbf{D}$ the strain-rate tensor and r the specific radiation power.

5.1.2 Shallow-ice approximation

The most comprehensive description of glacier dynamics, the 'Full-Stokes flow', only disregards acceleration in the momentum balance (Eq. 5.2). Full-Stokes flow thus involves solving a set of non-linear differential balance equations with respect to the five unknown variables, the velocity components, v_x, v_y and v_z, the pressure, p and the temperature T (Sec. 5.1.1). Full-stokes models are computationally very demanding and their application generally restricted to studies of small glaciers. The hydrostatic approximation considers a simplified stress field within large ice bodies. The vertical momentum balance is assumed to be dominated by the vertical normal stress, and integration over depth yields the hydrostatic pressure distribution. The hydrostatic pressure follows directly from glacier geometry, and hence, the pressure is eliminated from the set of unknown variables.

The Shallow-ice approximation (SIA) provides more rigorous simplifications. SIA is based on the assumption that typical length scales, L, largely exceeds typical height scales H, i.e. their aspect ratio ε is much smaller than unity (Hutter, 1983; Morland, 1984). The slopes of the ice-surface and bedrock topography are assumed to be small and the flow regime governed by bed-parallel shear. The stress field reduces to the hydrostatic pressure,

$$p = -\rho g(h - z), \tag{5.4}$$

where h is the surface elevation and z, the height within the ice column counted positive upward, and the shear stress components in the horizontal plane:

$$\tau_{xz} = -\rho g(h - z)\frac{\partial h}{\partial x}, \tag{5.5}$$

$$\tau_{yz} = -\rho g(h - z)\frac{\partial h}{\partial y}, \tag{5.6}$$

which are opposed by the basal drag. The effective stress,

$$\tau_{\text{eff}} = \rho g(h - z)|\nabla h|, \tag{5.7}$$

is fully determined by local glacier geometry. The ice flow depends on local ice thickness and surface slope and is aligned with the surface gradient. The individual components

can be readily substituted into Glen's flow law (Eq. 2.5) to determine velocity derivatives. The total ice flow is the sum of the ice flow by internal deformation and basal sliding. Determination of the velocity field allows for computation of the ice flux. Full glacier evolution is determined by supplementing the ice flux term with an accumulation-ablation function at the ice surface, melting at the glacier base and the rebound of the lithosphere.

SIA is suitable for the simulation of ice sheets and large ice caps over long time periods, but has its limitations: the assumptions are violated at the vicinity of ice divides, where ice flow is dominated by vertical compression and horizontal extension, as well as in the vicinity of the ice margins, which are generally characterized by steep surface slopes. SIA has also limitations in the case of non-negligible longitudinal stresses: ice regions resting on complex bedrock topography, and near the transition from grounded to floating ice, the 'grounding line'. Ice shelfs represent the extreme case for which basal drag vanishes and ice dynamics are governed by lateral drag and horizontal extension. Ice shelfs are properly described by the the shallow-shelf approximation (SSA), that follows from a scaling analysis similar as for the SIA derivation. SIA and SSA may be combined to provide a uniform framework for ice-sheets with grounded and floating ice regions or for improved simulation of fast flow within ice streams (Bueler and Brown, 2009).

5.2 The ice-sheet model SICOPOLIS

The numerical model 'SICOPOLIS' (SImulation COde for POLythermal Ice Sheets, http://sicopolis.greveweb.net/) simulates the large-scale evolution of ice sheets in space and time, employing SIA. Given the required input data consistent of surface and bedrock topography, air temperature and precipitation, as well as geothermal heat flux and sea level, the model computes the extent of glacierized area, ice thickness and the three-dimensional fields of velocity, temperature, water content and age of the ice. A particularity of SICOPOLIS is its treatment of cold and temperate ice regions, separated by a CTS, for which boundary conditions are specified in form of a jump equation (Greve, 1997). The temperature evolution in the cold ice is balanced by horizontal and vertical advection, vertical heat conduction and dissipative strain heating. In the temperate ice, the temperature follows directly from the pressure field and instead, the energy balance is provided by an evolution equation for the water content. Basal melting is computed by balancing the heat fluxes from the ice and the lithosphere and the heat generated by basal sliding. The geothermal heat flux is applied as boundary condition 5 km below the ice base to account for the thermal inertia of the lithosphere (Ritz, 1987). Isostatic adjustment of

the lithosphere due to changes in ice load is computed by the elastic lithosphere/relaxing asthenosphere (ELRA) approach (see Greve and Blatter, 2009, and references therein).

5.2.1 Accumulation-ablation function

SICOPOLIS computes the SMB from the given climate input, consistent of precipitation and air temperature (Greve, 1997). The precipitation field is kept constant over the entire model period while the surface temperature may adjust for changes in ice-surface elevation given the constant lapse rate. The monthly precipitation is split up in solid and liquid fraction, i.e. snow and rain, respectively, according to the monthly mean temperature and the specified temperature deviation. Temperature variations on a shorter time scale, e.g. the daily temperature cycle, are accounted for by introducing a standard temperature variation, T_0'. The total energy available for melt is calculated by a positive-degree-day approach. Liquid water, i.e. surface melt water and rain, may refreeze in the snow until a threshold value is reached, defined es a fraction, $P_{\max}$, of the annual snow accumulation. The snow is then assumed to be transformed into impermeable, temperate ice. The remaining energy is spend on melting of ice, associated with runoff, and hence, mass loss.

5.2.2 Sliding law

The dynamic boundary condition at the glacier bed is given by a Weertman-type sliding law (Greve and Blatter, 2009). Typically, sliding is enabled for a temperate ice base and no-slip conditions prevail for a cold base frozen to the ground. Here, I use a modified expression of the basal sliding velocity, v_{b}, following Hindmarsh and Le Meur (2001) and Greve (2005), that allows for partial sliding as the basal temperature approaches PMP, termed 'submelt sliding':

$$v_{\mathrm{b}}(T_{\mathrm{b}}') = -\frac{C_{\mathrm{b}}}{\rho g}\frac{|\tau_{\mathrm{b}}|^{p-1}}{N_{\mathrm{b}}^{q}}\tau_{\mathrm{b}}\exp\left(\frac{T_{\mathrm{b}}'}{\gamma}\right) \tag{5.8}$$

where τ_{b} is the basal shear stress, N_{b} the basal pressure, C_{b}, p and q are the sliding law coefficient and exponents and T_{b}' the basal temperature relative to PMP. Full sliding is enabled for a temperate ice base and exponentially decreases when basal temperatures drop below PMP. The transition between no-slip and slip conditions at the glacier base is prescribed by a submelt-sliding parameter, γ, expressed in °C. It defines the temperature deviation from PMP, for which full sliding is reduced by a factor e^{-1}. A large positive value of γ allows for initiation of sliding well below PMP in a smooth way. A small

positive value, leads to abrupt onset of sliding close to PMP. The basal pressure is given either by the full hydrostatic ice-overburden pressure p_f,

$$p_\mathrm{f} = \rho g H_\mathrm{i}, \tag{5.9}$$

or by the reduced basal pressure p_r, the difference between the ice-overburden pressure and the basal water pressure. To account for the buoyancy force exerted upon the ice volume submerged below sea level, the basal water pressure is assumed to equal the sea water pressure,

$$p_\mathrm{r} = p_\mathrm{f} - \rho_\mathrm{sw} D_\mathrm{w}, \tag{5.10}$$

where ρ_sw is the density of the sea water and D_w the water depth. Note that drainage of basal water from beneath the marine terminus requires an additional pressure head in order to overcome the sea water pressure (Pfeffer, 2007). To assure numerical stability and to keep sliding velocities given by Equation 5.8 within a reasonable range, p_r is constrained to be $\geq 0.2 \times p_\mathrm{f}$.

5.2.3 Calving law

Grounded marine-ice margins typically constitute a vertical calving front that fulfils a certain stability criterion, i.e. the actual ice thickness must exceed the flotation thickness at all times ($H_\mathrm{i} \geq \rho_\mathrm{sw}\, \rho^{-1}\, D_\mathrm{w}$). Otherwise the grounded margin will either disintegrate or form a floating ice tongue or ice shelf. Models using a fixed grid in the map plane usually lack the ability to track the position of the calving front on a subgrid scale. Nevertheless, the models can simulate a retreat of a marine ice margin by setting H_i at particular gridpoints to zero. Advances of the calving front, however, require the marine-ice margin to protrude at least one gridcell in one single time-step while overcoming the stability criterion. This cannot be realized at reasonable flow velocities. To bypass this shortcoming, models usually allow the ice to extend underwater without becoming afloat (Fig. 5.1). Here, this 'underwater ice' is treated as regular ice, but is further subjected to calving that acts on its surface as an additional ablation term. I employ a modified version of the calving parameterization of Marshall *et al.* (2000) that relates the calving flux, Q_c, to the water depth, D_w, to some power k and the ice thickness, H_i, to some power l:

$$Q_c = k_c {D_w}^k {H_i}^l, \tag{5.11}$$

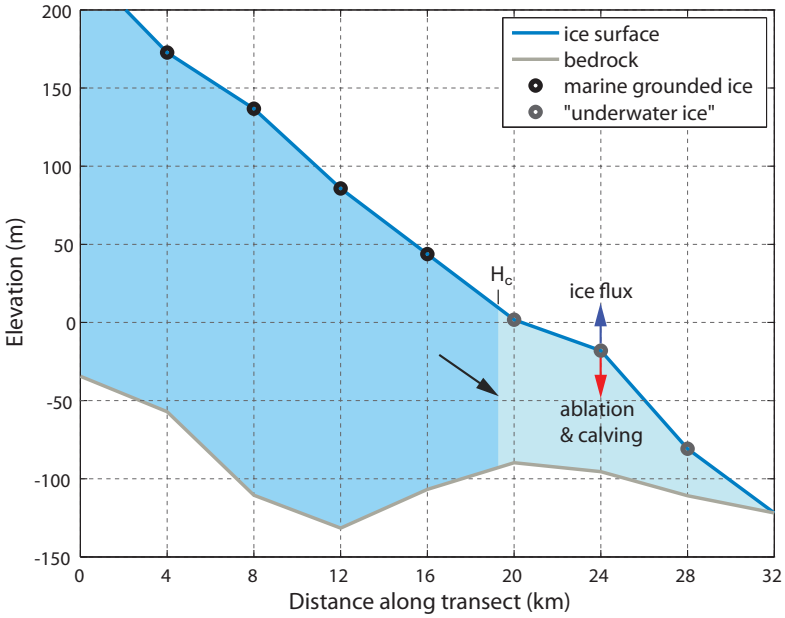

Figure 5.1: Schematic 2-D cross section of a marine terminating ice margin. Circles indicate ice surface elevation at gridpoints with 4 km spacing that are treated as regular ice (black) or underwater ice (UW-ice; dark grey), if the local ice thickness falls below a the critical floatation thickness, H_c. The annual SMB of the UW-ice is negative. The surface of an UW-ice column can only be raised above flotation, if the the flux rate exceeds mass loss due to melting and calving over a significant time period.

where k_c is a calving parameter that may include effects of margin geometry, longitudinal stress gradients, ice temperature or hydraulic fracturing.

This treatment of marine ice represents an improvement to earlier approaches in large-scale ice sheet models that limit the marine ice extent by defining a bathymetric contour at which the ice is simply cut-off, either described by a constant value (Tarasov and Peltier, 1997) or a function of sea-level (Zweck and Huybrechts, 2005). A new concept of subgrid parameterization of ice-front motion that maintains a vertical calving front has recently been applied to another large-scale finite-difference ice sheet model (Albrecht *et al.*, 2010). This approach provides a promising basis for implementation of physical based calving laws such as the waterline crevasse-depth model of (Benn *et al.*, 2007).

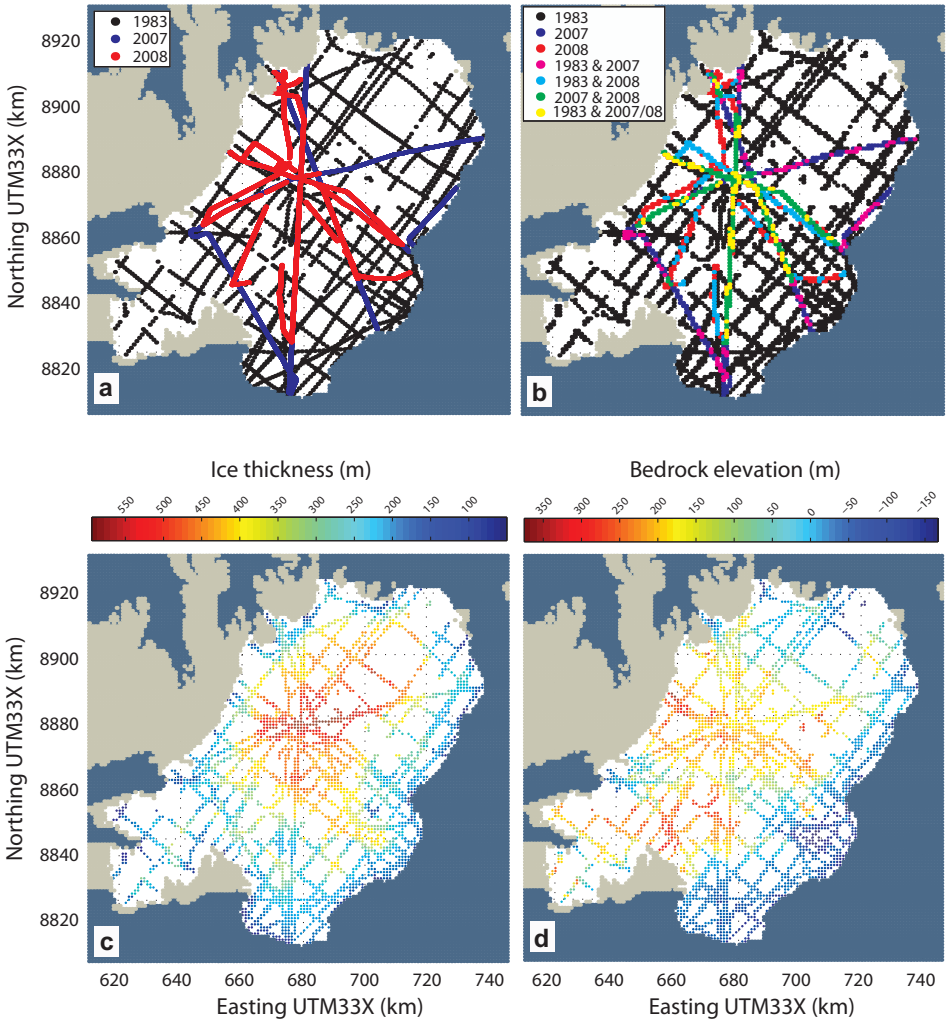

Figure 5.2: Ice thickness surveys: coverage and results. (a) Location of data points of airborne RES survey in 1983 (Dowdeswell *et al.*, 1986) along with profiles of 2008 from both airborne RES and GPR; (b) data coverage at 1-km gridpoints from multiple surveys; (c) measured ice thickness and (d) bedrock elevation. Land area is shaded grey and the sea, marine blue.

5.3 Model-input and setup

Simulations of glacier dynamics and mass balance require accurate information about the glacier geometry, i.e. surface and bedrock topography, as well as the external forcing, in

terms of precipitation, air temperature, geothermal heat flux and sea level. This thesis involves the compilation of a comprehensive model input of Austfonna, and the derivation of a new bedrock map in particular. The model input is based on previously existing datasets, as well as new data, collected during the course of the thesis project. The new model domain 'Austfonna' covers an area of 136×132 km and spans from 610.2–746.2 km UTM33X East to 8800.2–8932.2 km North. The input fields were prepared on a rectangular grid at 1 km horizontal resolution, yielding 137×133 gridpoints in the horizontal plane. The input fields were then also resampled on grids at 2 and 4 km horizontal resolution, encompassing 69×67, and 35×34 gridpoints, respectively.

5.3.1 Geometry

The model domain for Austfonna encompasses the western part of Vestfonna, a number of smaller isolated glaciers and ice caps, as well as Vegafonna, a ∼300 km^2 ice cap attached to the southwest of Austfonna. Austfonna and Vegafonna form a continues ice body, and in the following, the term Austfonna will always include Vegafonna. Other separate ice bodies within the model domain are disregarded, i.e. their ice surface is treated as land surface.

The surface elevation above sea level is based on a Digital Elevation Model (DEM) of Nordaustlandet at 250 m resolution (personal communication K. Melvold, Department of Geosciences, University of Oslo, Oslo, Norway, 2005). The DEM is derived from a 1 : 250 000 map of Svalbard (Sheet 3) published by NPI in 1998 and InSAR data of Austfonna acquired in 1995–96 (Unwin and Wingham, 1997). A glacier outline at 100 m horizontal resolution is available based on data from NPI, an airborne photographic survey in 1990 and kinematic GPS measurements of helicopter tracks along the southeastern marine ice margin in 1992. The bathymetry is represented by the publicly available International Bathymetric Chart of the Arctic Ocean, Version 2.0 (Jakobsson *et al.*, 2008) having a horizontal resolution of 2 km. The bedrock beneath the ice cap is derived by subtracting scattered ice-thickness data from the surface topography. I supplement the airborne RES data published by Dowdeswell *et al.* (1986) with two new datasets from spring 2008. The Danish National Space Centre acquired 60 MHz airborne RES data, while a ground team collected 20 MHz GPR data along profiles of ∼800 km length (Vasilenko *et al.*, 2010). The profiles follow the routes investigated by the University of Oslo and NPI for mass-balance purposes since 1998 (Schuler *et al.*, 2007; Taurisano *et al.*, 2007; Dunse *et al.*, 2009) and cover special areas of interest, such as Duvebreen and Basin-3 (Fig. 5.2a).

To homogenize the various data, all datasets are resampled onto the 1 km grid that spans the Austfonna domain. Resampling is achieved by distance-weighted averaging of available data within a search radius that equal to one gridcell diagonal. No value is assigned at gridpoints that lack data in their vicinity. This is done for each individual data set, separately, i.e. for the surface DEM, the bathymetry and the three ice thickness surveys. Some gridpoints have multiple ice-thickness information (Fig. 5.2b). In this case, a mean value is applied (Fig. 5.2c). Provided that ice thickness information exist, the bedrock elevation at ice-covered gridpoints is derived by subtracting the ice thickness value from the surface elevation (Fig. 5.2d).

The DEM is regarded as the most accurate data source and given priority in the case of inconsistencies with other datasets. The glacier outline distinguishes between ice-covered and ice-free gridpoints. The surface elevation of the DEM allows to distinguish wether the ice-free gridpoints are associated with land areas or the open sea (ocean). An ice-land-ocean mask is created, that attributes each gridpoint with a particular class (Fig. 5.3a). The mask is used to assign gridpoints with the raw dataset associated with each particular class, i.e. the DEM with land areas outside Austfonna, the bathymetry with the ocean and the bedrock information from the ice-thickness surveys and the DEM within the area covered by Austfonna. A quality check of the raw data is performed prior to the interpolation. The coastline of the bathymetry does not exactly match that of the DEM, causing positive elevations at some gridpoints that are classified as ocean. Elevation-values of the associated gridpoints and their nearest neighbour are eliminated, i.e. at

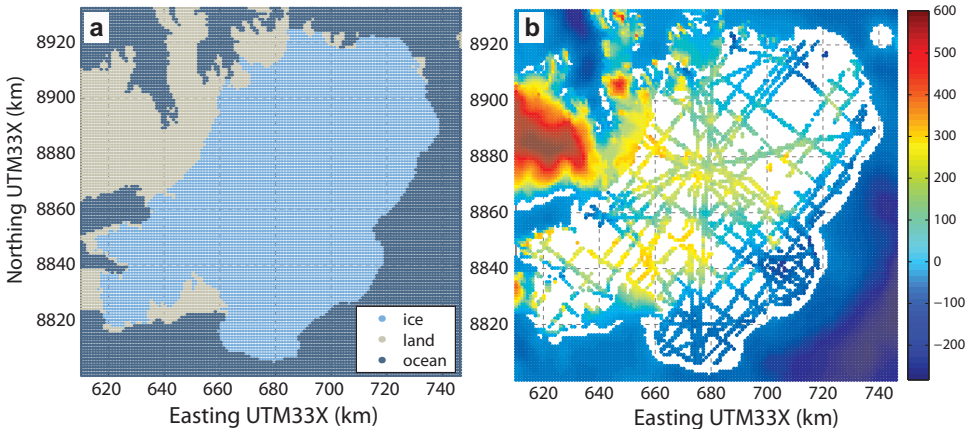

Figure 5.3: (a) Ice-land-ocean mask and (b), the resampled bedrock data for each class.

gridpoints within a search radius of 3.1 km in the southeast and 1.1 km in the northwest. The resulting raw data forms the basis for the new bedrock map (Fig. 5.3b).

The bedrock interpolation involves fitting a plate through the available data. The plate is thought to be connected to individual data points by elastic springs. Spring constants and plate stiffness can be adjusted in order to yield the desired data fit and smoothness of the interpolated surface. The resulting bedrock map is validated against several criteria (Fig. 5.4a): Positive bathymetric values are removed from the original raw data, and where

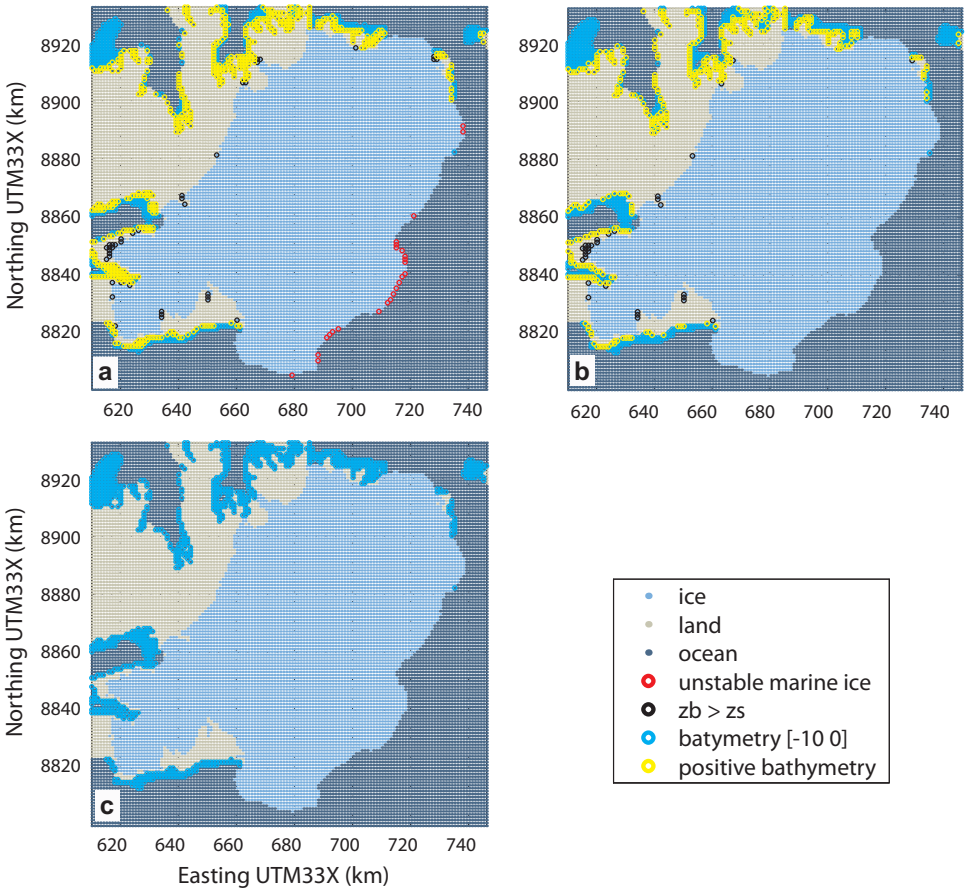

Figure 5.4: Validation of iterative bedrock interpolation sets constraints for unphysical or problematic gridpoint values, i.e. bathymetry above sea level, marine grounded ice thickness less then flotation thickness, a bedrock elevation, zb, in excess of the surface elevation, zs. (a) first iteration, (b) second iteration, (c) final enforcing of above criteria.

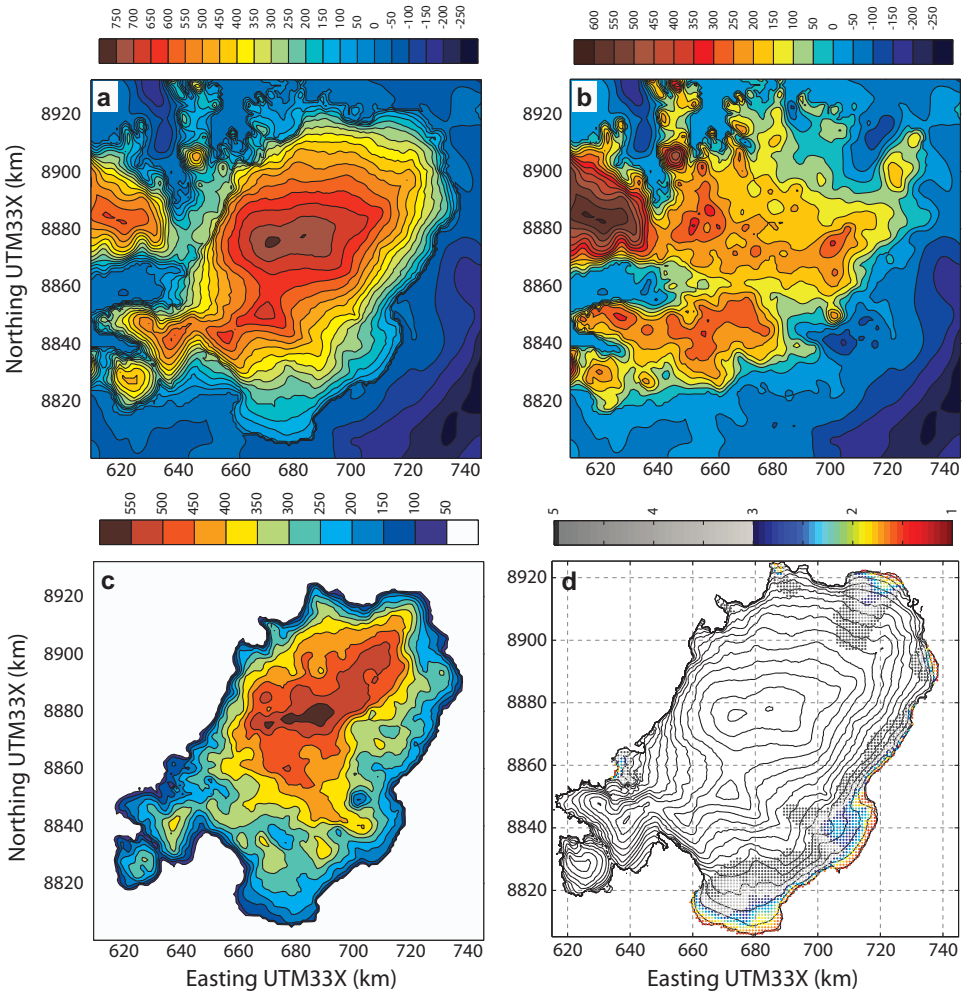

Figure 5.5: The geometric model input at 1 km resolution: (a) surface topography, (b) bedrock topography, (c) ice thickness, and (d) the resulting flotation ratio of marine grounded ice.

necessary, the bedrock elevation is adjusted to correct for bedrock elevations in excess of the surface elevation and thicknesses of marine ice, less than the flotation thickness. The bedrock interpolation is repeated with the updated dataset. Remaining erroneous values are manually corrected (Fig. 5.4b). A minimum surface elevation of 30 m for marine ice, removes potentially floating ice. This is justified as no floating ice exist on Austfonna and satellite observations suggest an average height of the calving front of ∼34 m (personal

communication G. Moholdt, Department of Geosciences, University of Oslo, Oslo, Norway, 2010). Positive bathymetry is first set to sea level, then bathymetric values in the range –10–0 m are projected onto a the range –10–5 m. This ensures proper representation of shallow fjords, in the north and west (Fig. 5.4c). This is also important to properly present land-based vs. marine terminating outlet glaciers. The final bedrock map is presented in Figure 5.5, along with the surface-elevation and ice thickness map, as well as the flotation ratio, defined as ice thickness divided by flotation thickness.

5.3.2 Climate forcing

The climate input consists of monthly mean precipitation and temperature fields. The temperature input is based on observations of two automatic-weather station on Etonbreen, one at Eton-2, 341 m a.s.l., another at Eton-4, 510 m a.s.l. The employed record spans a period from 2004–09 and has a 1 hour temporal resolution. The coldest temperatures were measured in March, with a monthly mean of about –20°C, and the warmest

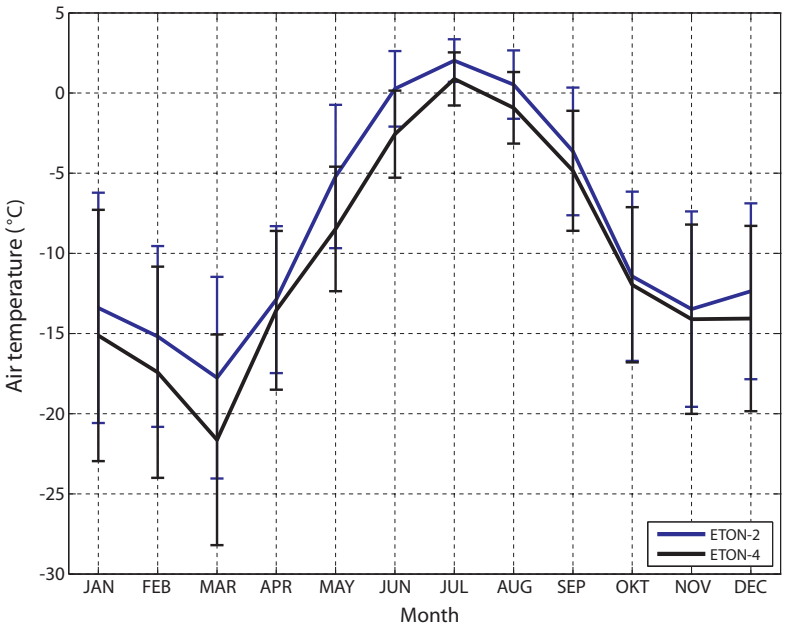

Figure 5.6: Monthly mean air temperatures based on hourly records from two AWSs on Etonbreen at 341 m elevation (Eton-2) and 510 m (Eton-4), respectively, during the time period 2004–2009 and associated standard deviation indicated as error bars.

Table 5.1: Monthly mean air temperatures based on hourly records from two AWSs on Etonbreen at 341 m elevation (Eton-2) and 510 m (Eton-4), respectively, during the time period 2004–2009 and associated standard deviations.

	Eton-2		Eton-4	
Month	T **(°C)**	T_0' **(K)**	T **(°C)**	T_0' **(K)**
JAN	–13.4	7.2	–15.1	7.9
FEB	–15.2	5.6	–17.4	6.6
MAR	–17.8	6.3	–21.6	6.6
APR	–12.9	4.6	–13.6	5.0
MAY	–5.2	4.5	–8.5	3.9
JUN	0.3	2.4	–2.6	2.7
JUL	2.0	1.3	0.9	1.7
AUG	0.5	2.1	–0.9	2.2
SEP	–3.6	4.0	–4.8	3.7
OCT	–11.4	5.3	–12.0	4.8
NOV	–13.5	6.1	–14.1	5.9
DEC	–12.4	5.5	–14.1	5.8
MAY–SEP	–1.2	2.9	–3.2	2.8
OCT–APR	–13.8	5.8	–15.4	6.1
Mean Annual	–8.5	4.6	–10.3	4.7

in July, slightly above freezing (Fig. 5.3.2). Temperature deviations during the winter months (Oct–April), ∼6°C, double those during the summer months (May–Sep), ∼3°C (Table 5.1). For the model input, monthly mean temperatures measured at Eton-4 are distributed over the entire model domain using a mean lapse rate of $-0.0045\,\mathrm{K\,m^{-1}}$ (Schuler *et al.*, 2007). The precipitation field is based on ERA-40/ERA-Interim reanalysis at a 6 hour temporal resolution for the period 1960 to 2006 (personal communication T.V. Schuler, Department of Geosciences, University of Oslo, Oslo, Norway, 2007-11). Monthly mean precipitation fields have been downscaled using a simple precipitation model (Smith and Barstad, 2004; Schuler *et al.*, 2008).

Application of this idealized present-day climate on the present-day topography leads to a net SMB close to zero ($+0.07\,\mathrm{m\,w.e.\,a^{-1}}$), in agreement with recent observations for the time period 2002 to 2008 (Moholdt *et al.*, 2010a). The modelled SMB of Austfonna matches the observations better, if rain is forced to runoff, immediately, instead of being allowed to refreeze in the snow. If additional rain is allowed to refreeze, ablation by meltwater runoff increases and the SMB becomes too negative. This can be explained by the fact, that less energy is spend on the transformation from snow to ice, before melting

of ice can set in. Melting of ice is more efficient than melting of snow, i.e. the characteristic melt factor for ice, β_{ice}, is about 2–3 times larger than those for snow, β_{snow}.

5.3.3 Initial ice temperature

No direct measurements of the geothermal heat flux are available for Nordaustlandet. However, the geothermal heat flux can be estimated from the vertical temperature profile retrieved from the borehole at the summit in 1987 (Zagorodnov *et al.*, 1989b), assuming a vertical ice column at rest. This is a reasonable assumption at the summit. The constant gradient below the temperature minimum at about 160 m depth suggest a moderate geothermal heat flux of 40 mW m^{-2} (Ignatieva and Macheret, 1991). Significantly

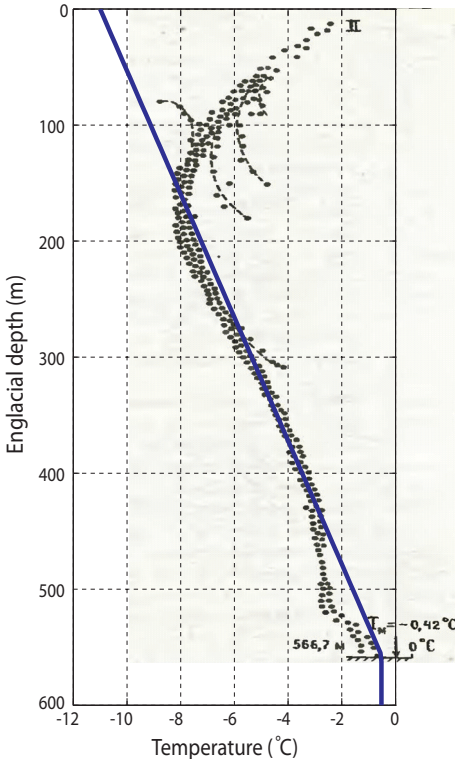

Figure 5.7: Theoretical initial-state vs. previously observed vertical temperature profile in the summit area of Austfonna. The blue solid line represents a steady-state temperature profile for a surface temperature of –11°C and a geothermal heat flux of 40 mW m^{-2}. The measured profile is adopted from Zagorodnov *et al.* (1989b) and based on a borehole drilled in 1987.

increased temperatures towards the glacier surface can be explained by considerable firn warming since the termination of the Little Ice Age (Zagorodnov *et al.*, 1989b).

The initial ice temperature assumes a steady-state temperature gradient according to the geothermal heat flux, while the annual mean air temperature constrains the temperature at the ice surface. The temperature within the ice volume is limited to the basal PMP determined by the ice-overburden pressure. At the summit, good agreement of the initial temperature profile with the observed one is achieved for the lower 400 m (Fig. 5.7). In the upper layer, the initial ice temperatures are too low at the beginning, but may change after ∼100 model years, depending on the significance of the firn warming, that SICOPOLIS accounts for.

6 Summary of Papers and Key Results

6.1 Spatial and temporal variability in the distribution of distinct glacier facies (Paper I)

GPR measurements at a center frequency in the P and L-band (∼400 MHz–2 GHz) provide valuable information on the near-surface structure of glaciers. This paper presents new 800 MHz GPR data collected on Austfonna in spring 2006 and 2007. Snow accumulation and hence winter mass balance is mapped along continuous profiles and compared to results from earlier surveys along the same transects in 1999, 2004 and 2005 (Taurisano *et al.*, 2007). The typical snow-accumulation pattern of Austfonna with about twice as much snow accumulation in the southeast compared to the northwest and a large interannual variability in the total amount of snow (Pinglot *et al.*, 2001) is confirmed also for the extended observational period.

Rigorous data processing allows identification and classification of radar zones with characteristic reflection patterns. These radar zones are associated with the physical properties of firn, superimposed ice and pure glacier ice underneath the snow cover and hence, related to distinct glacier facies. For the first time, these radar zones are utilized to monitor interannual changes in glacier facies along coinciding survey transects. The GPR data from 2004/05 is included in the study and re-processed for this purpose. GPR data interpretation was validated by manual snow-depth soundings, snow pit analysis and neutron-probe inferred vertical density profiles over the depth range investigated by the GPR ($\gtrsim$10 m). The resulting 4-year time series reveals a pronounced growth of the firn area beginning in winter 2004/05, both in terms of firn thickness and areal extent, following an initial decrease in winter 2003/04. The initial decrease and subsequent steady growth of the firn into an area previously classified as SI, indicates an increasingly larger SMB between 2004/05–2006/07, following an unusually negative balance year 2003/04 for which the GPR data indicate severe ablation of the snow cover, even within the summit area.

This study showed that repeated GPR surveys provide information beyond the commonly evaluated winter mass balance. At Austfonna, internal accumulation and SI formation constitutes a major contribution to the net accumulation and a growing firn area significantly increases the potential of meltwater retention, achieving favorable conditions for a more positive SMB during subsequent years. GPR-derived maps of radar zones also provide valuable ground-truth for remote sensing missions of ice volume changes, such as ESA's CryoSat-II missions, for which Austfonna is a selected calibration/validation site. Knowledge about spatial and temporal variation in the physical properties of the near-surface structure of glaciers provide constraints for processing and interpretation of the satellite data. Despite much higher frequencies involved, e.g. in the Ku-band (∼13.5 GHz), radar signals of satellite altimeters penetrate into the near-surface snow and ice. Identification of surface reflection may be erroneous where strong internal reflections occur, e.g. from ice layers within the snow or firn. Furthermore, information about the extent of the firn area provide a valuable constraint for assumptions on spatial density variations that are essential for the conversion of the inferred volume change to mass change, and hence, the contribution of land-ice masses to eustatic sea level rise.

6.2 Spatial and temporal variability in ice-surface velocities (Paper II)

Despite a large interannual variability in snow accumulation and SMB (Paper I), Austfonna's mean SMB during the recent decade has been close to zero (Moholdt *et al.*, 2010a). Austfonna's total mass balance was yet negative, due to a retreat of the marine ice margins and calving from marine terminating outlets (Dowdeswell *et al.*, 2008). The calving rate depends on the ice flux towards the calving front and calving estimates therefore rely on observations of ice-surface velocity and assumptions on its depth-averaged derivative. At Austfonna, the ice flux is concentrated in spatially limited fast-flow units, imbedded within a slow moving bulk of the ice cap. Previous knowledge of the flow pattern of Austfonna is primarily limited to InSAR-derived winter snapshots of ice-surface velocity during the mid 1990s (Dowdeswell *et al.*, 1999; Bevan *et al.*, 2007).

Paper II presents continuous GPS measurements along the central flowlines of two of Austfonna's flow units, Duvebreen in the north and Basin-3 in the southeast. Basin-3 is known to have surged in the past. The records span a time period of two years (2008–10) and provide insights into intra-annual and year-to-year velocity changes. At Basin-3, the observed annual mean ice-surface velocities exceed those measured by InSAR in the mid

1990s by a factor $\gtrsim$3, indicating that ice loss due to calving from this outlet may be significantly larger than previously suggested. A marked speed-up following the onset of the summer melt period is recorded at both Basin-3 and Duvebreen, indicating enhanced basal motion through input of meltwater into the subglacial drainage system. Air temperatures recorded at a nearby AWS were significantly higher during summer 2009 than in 2008 and the relation between ice-surface velocity and melt periods more complex. This could be explained by a transition towards a hydraulically more efficient drainage system that can accommodate repeated meltwater input without increasing basal water pressure.

6.3 Controls on the dynamic behaviour: steady fast-flow vs. surge-type behaviour (Paper III)

Previous observation of surface-elevation change of Austfonna during the last 1–2 decades revealed a marked interior thickening and marginal thinning (Bamber *et al.*, 2004; Moholdt *et al.*, 2010a). Several of Austfonna's drainage basins are known to have surged in the past and appear to have remained quiescent during the last ∼80–150 years. There is growing evidence that the observed elevation changes of Austfonna are caused by insufficient ice dynamics associated with the quiescent phase, rather than by changes in SMB (Bevan *et al.*, 2007). None of the basins was observed to surge twice, because of a long duration of the quiescent phase, estimated to last about 150–500 years (Schytt, 1969; Solheim, 1991), much longer than for surge-type glaciers in other regions. Statistical analysis suggest a thermally controlled soft-bed surge mechanism for Svalbard glaciers (Hamilton and Dowdeswell, 1996; Jiskoot *et al.*, 2000).

To investigate the controls on the dynamic behaviour of Austfonna and possible surge mechanisms, in particular, I employ the ice-sheet model SICOPOLIS (Greve, 1997). The model is based on SIA and solves the thermomechanically coupled balance equations of mass, momentum and energy, along with Glen's flow law and boundary conditions for the free surface, the ice-bed interface and the CTS. A comprehensive model-input dataset is presented, comprising surface and bedrock topography and external forcing in terms of precipitation, air temperature and geothermal heat flux. The present-day geometry is then used as initial conditions for diagnostic model runs with the present-day climate as external forcing.

Special attention is given to the description of basal motion and the role of ice areas grounded below sea level, about 28 % of the presently glacierized area. A series of model experiments is defined, each characterized by a unique combination of sliding-law

parameters. Bedrock areas above sea level are described as consisting of hard bedrock, while the conditions at the ice-bed interface below sea level are systematically changed to represent a broad range of potential basal environments: from hard bedrock or immobile permafrost to a layer of soft, water-saturated sediments. Each experiment is run for a set of varied basal temperature ranges below the pressure-melting point, in which a transition from no-slip conditions to full basal sliding is described by an exponential function. Depending on the scenario, fast flow units operate in distinct dynamic modes. A transition from steady fast-flow to cyclic surge-type behaviour occurs for a more abrupt onset of basal sliding in combination with enhanced sliding of marine grounded ice areas, e.g. by plastic deformation of water-saturated sediments. Basal temperature appears to play a decisive role for glacier surges of Austfonna and ultimately governed by significant long-term changes in glacier geometry. The model results are in agreement with the previously suggested thermally controlled soft bed surge mechanism. Irrespective of the dynamic regime, the simulated ice cap lacks considerable volumes of temperate ice. Fast-flow is nevertheless achieved through basal motion, where the ice-bed interface is at or near the pressure melting point. Given a constant present-day climate, the simulated equilibrium ice cap size varies significantly depending on the chosen sliding-law parameters.

6.4 Transient simulations of Austfonna (Report)

Prognostic model runs of Austfonna are performed as a contribution to the model initiative GlacMod2010. The initiative calls on the glacier-modelling community to investigate the response of an appreciable number of simulated glaciers and ice caps to a set of climate-change scenarios up to the year 2100. A synthesis report will be compiled with the aim to facilitate projections of the contribution of glaciers and ice caps to global sea level rise in a warming climate.

The model is forced with a linear increase in air temperature with and without an associated increase in precipitation. Due to the short simulation period of 90 years compared to the principle period of simulated surge-type behaviour, the model was set-up with flow units in steady fast-flow mode. Steady-state ice cap configuration according to diagnostic simulations presented in Paper III are used as initial conditions. The prescribed increase in precipitation is found insufficient to compensate for the non-linear increase in mass loss that is associated with the warming scenario.

Declaration of the main authors contribution

I participated in fieldwork on Austfonna during two field visits of one month duration in spring 2007/08 and one short visit in summer 2008. I have processed all 800 MHz GPR data and performed the filtering and analysis of the continuous GPS data. With respect to the modelling study, I compiled the model input, including bed- and surface topography, precipitation and air temperature fields, and implemented the new model domain 'Austfonna' into the ice-sheet model SICOPOLIS. During a 4-month stay at the Institute of Low Temperature Science, Hokkaido University, Sapporo, Japan, I was involved in development of a new model version SICOPOLIS V3.0, e.g. with respect to model initialization of ice temperatures, model input/output routines and implementation of a calving law. I developed the main ideas and concepts of Paper I–III, wrote the original manuscripts, designed all figures and implemented comments from co-authors and reviewers.

6.5 Other publications and conference presentations

Peer-reviewed publications

Dunse, T., O. Eisen, V. Helm, W. Rack, D. Steinhage and V. Parry. 2008. Characteristics and small-scale variability of GPR signals and their relation to snow accumulation in Greenland's percolation zone. Journal of Glaciology, 54 (185), 333–342.

Brandt, O., R.L. Hawley, J. Kohler, J.O. Hagen, E.M. Morris, T. Dunse, J.B.T. Scott, and T. Eiken. 2008. Comparison of airborne radar altimeter and ground-based Ku-band radar measurements on the ice cap Austfonna, Svalbard, The Cryosphere Discuss., 2, 777–810.

Conference presentations

Dunse, T., R. Greve, T.V. Schuler, J.O. Hagen. 2010. Investigating surge behaviour versus quasi-permanent fast flow of the Austfonna ice cap, Svalbard, by numerical modelling. IPY Oslo Science Conference, Oslo, Norway, 08–12 June 2010.

Dunse, T., R. Greve, T.V. Schuler, J.O. Hagen, F. Navarro, E. Vasilenko, C. Reijmer. 2010. Insights into the dynamic regime of the Austfonna ice cap, Svalbard, from

numerical modelling and observation. IASC GLACIODYN (IPY) meeting 2009, Obergurgl, Austria, 7–10 March 2010.

Dunse, T., R.Greve, T.V. Schuler, J.O. Hagen, F. Navarro, E. Vasilenko, C. Reijmer. 2009. Improved parameterization of marine-ice dynamics and flow instabilities for simulation of the Austfonna ice cap using a large-scale ice sheet model. 2009 AGU Fall meeting, San Francisco, California, USA, 14–18 December 2009. [poster]

Dunse, T., T.V. Schuler, J.O. Hagen, R. Greve, G. Moholdt, T. Eiken. 2009. Modelling flow dynamics and geometry of the Austfonna ice cap, Svalbard. 32nd Symposium on Polar Meteorology and Glaciology, Tokyo, Japan, 17–18 November 2009. [poster]

Dunse, T., T.V. Schuler, J.O. Hagen, R. Greve, G. Moholdt, T. Eiken. 2009. Modelling flow dynamics and geometry of the Austfonna ice cap, Svalbard. International Symposium 'Frontier of Low Temperature Science', Sapporo, Japan, 9–10 November 2009. [poster]

Dunse, T., T.V. Schuler, A. Adalgeirsdottir and J.O. Hagen. 2009. Modelling flow dynamics and form of the Austfonna ice cap, Svalbard. Workshop on the dynamics and mass budget of Arctic glaciers / GLACIODYN (IPY) meeting, Kananaskis Country, Canada, 16–19 February 2009.

Dunse, T., T.V. Schuler, and A. Adalgeirsdottir. 2008. The dynamics of Austfonna, Svalbard - a modelling approach. IGS - Nordic Branch Annual Meeting 2008, Helsinki, Finland, 6–8 November 2008.

Dunse, T., T.V. Schuler, J.O. Hagen, T. Eiken, A. Taurisano and K.A. Høgda. 2008. Recent fluctuations in the extent of the firn area of Austfonna, Svalbard, inferred from ground-penetrating radar. Workshop on mass balance measurements and modelling, Skeikampen, Norway, 25–28 March 2008.

Dunse, T., T.V. Schuler and J.O. Hagen. 2008. Application of a numerical ice sheet model on Austfonna, Svalbard - model preparations and input data. Workshop on the dynamics and mass budget of Arctic glaciers, GLACIODYN (IPY) meeting, Obergurgl, Austria, 28–31 January 2008. [poster]

Dunse, T., T.V. Schuler, J.O. Hagen, T. Eiken, G. Moholdt and K.A. Høgda. 2007. Glacier facies transitions on Austfonna, Svalbard, derived from GPR. IGS - Nordic Branch Annual Meeting 2007, Uppsala, Sweden, 25–27 October 2007.

Dunse, T., T.V. Schuler, A. Taurisano, J.O. Hagen, K. Melvold, T. Eiken and G. Moholdt. 2007. Snow accumulation over Austfonna, northern Svalbard, derived by ground-penetrating radar. Workshop on the dynamics and mass budget of Arctic glaciers, GLACIODYN (IPY) meeting, Pontresina, Switzerland, 15–18 January 2007. [poster]

7 Outlook

The results and conclusion presented in this thesis suggest several topics for potential future work. Austfonna is selected for ground-based calibration/validation activities of ESA's CryoSat-2 mission. Launched in April 2010, CryoSat-2 replaces the CryoSat satellite that was lost due to a launch failure in October 2005 and aims at measuring mass and thickness fluctuations in the Earth's land ice masses and sea ice cover. Against this background it will be useful to extend the analysis of spatial and temporal variability in snow accumulation and distinct radar zones presented in Paper I, by including 800 MHz GPR data collected in subsequent springs 2008–10. Continued observations are essential to distinguish long-term trends in the SMB from interannual variations.

The GPS records presented in Paper II revealed that current ice-surface velocities of Basin-3 are much higher than in the mid 1990s. Continued measurements are required to investigate if the observed acceleration represents a short-lived flow anomaly or a general change in the dynamics of this flow unit. The latter could be related to the basin's surge cycle. More accurate measurements of horizontal and vertical displacement utilizing dual-frequency GNSS receivers, instead of the single-frequency devices used in this study, would also allow to resolve hourly to daily velocity variations. This would help to properly assess the relative contribution of external factors, e.g. climate and ocean tides, and intrinsic dynamic processes to glacier response to climate change. The velocity measurements should be supplemented with on-spot meteorological and ablation monitoring that allow computation of the accurate timing of melt-water runoff and input into the englacial/subglacial drainage system. In addition to isolated point measurements, spatially distributed observations of modern flow velocities and an updated outline of the marine ice margin are required to improve estimates of the total calving flux from the ice cap. This task may be tackled by employing spaceborne interferometric or speckle tracking/intensity tracking techniques, e.g. from ALOS-PalSAR, a Japanese satellite launched in January 2006.

To date, very limited information on the basal thermal regime, subglacial drainage system, bedrock lithology and presence of subglacial sediments exist. The model results

presented in Paper III confirmed the great significance of the basal conditions with respect to the dynamic regime of Austfonna. In order to achieve a more accurate match of the simulated and the observed ice cap, sliding-law parameters should be rather provided as functions of space and time, than as constants. Observations of basal conditions are essential to properly constrain the functions. Information on basal conditions can be extracted from the bedrock reflection coefficient of low-frequency radar data, providing that no variable gain amplification is applied during data recording. Vibrator sources in active seismic measurements, referred to as 'Vibroseis', provide a promising alternative to collect valuable information of the conditions at the ice-bed interface (Eisen *et al.*, 2010). Vibroseis measurements may cover large areas with minimal efforts compared to conventional seismics and similar to radar measurements. Furthermore, boreholes drilled down to the glacier bed allow for in situ measurements, including the retrieval samples of potential subglacial sediments. The boreholes may be instrumented to monitor water pressure and temperature, as well as basal motion.

Concerning the simulations of Austfonna using SICOPOLIS, further development should focus on the representation of fast-flow units and implementation of a physically based calving law, such as the waterline-crevasse depth model by Benn *et al.* (2007), along with subgrid-representation of front displacements (Albrecht *et al.*, 2010). The dynamic instability associated with interactions between calving and glacier dynamics is still not properly accounted for in global estimates of glacier response to climate change, and hence, sea-level rise. An ice-shelf module is currently implemented into SICOPOLIS (personal communication T. Sato, Institute of Low Temperature Science, Hokkaido University, Sapporo, Japan). Improvements in the description of basal sliding, and hence, fast flow, can be achieved by combining the SIA and SSA modules (Bueler and Brown, 2009). The suggested model developments, along with a more realistic input of the basal conditions, would allow to assess this dynamic instability.

Bibliography

ACIA, 2004. Impacts of a Warming Arctic. Technical report, Arctic Climate Impact Assesment, Cambridge, United Kingdom.

Ahlmann, H., Ångström, A., and Fjeldstad, J. E., 1933a. Scientific Results of the Swedish-Norwegian Arctic Expedition in the Summer of 1931, Part IX-X. Geografiska Annaler, 15, pp. 261–348.

Ahlmann, H., Eriksson, B., Ångström, A., and Rosenbaum, L., 1933b. Scientific Results of the Swedish-Norwegian Arctic Expedition in the Summer of 1931, Part IV-VIII. Geografiska Annaler, 15, pp. 73–216.

Ahlmann, H. and Rosenbaum, L., 1933. Scientific Results of the Swedish-Norwegian Arctic Expedition in the Summer of 1931, Part I-III. Geografiska Annaler, 15, pp. 1–68.

Albrecht, T., Martin, M., Haseloff, M., Winkelmann, R., and Levermann, A., 2010. Parameterization for subgrid-scale motion of ice-shelf calving-fronts. The Cryosphere, 4(3), 1497–1523.

Bamber, J., Krabill, W., Raper, V., and Dowdeswell, J., 2004. Anamolous recent growth of part of a large Arctic ice cap: Austfonna, Svalbard. Geophysical Research Letters, 31(12), L12402.

Benn, D. I., Hulton, N. R., and Mottram, R. H., 2007. 'Calving laws', 'sliding laws' and the stability of tidewater glaciers. Annals of Glaciology, 46, 123–130.

Bevan, S., Luckman, A., and Murray, T., 2007. Positive mass balance during the late 20th century on Austfonna, Svalbard revealed using satellite interferometry. Annals of Glaciology, 46, 117–122.

Binney, F. G., 1925. The Oxford University Arctic Expedition, 1924. The Geographical Journal, 66(1), pp. 9–40.

Björnsson, H., 1998. Hydrological characteristics of the drainage system beneath a surging glacier. Nature, 395(6704), 771–774.

Björnsson, H., Gjessing, Y., Hamran, S. E., Hagen, J. O., Liestøl, O., Palsson, F., and Erlingsson, B., 1996. The thermal regime of sub-polar glaciers mapped by multi-frequency radio-echo sounding. Journal of Glaciology, 42(140), 23–32.

Blake, W., 2006. Occurrence of the Mytilus edulis complex on Nordaustlandet, Svalbard: radiocarbon ages and climatic implications. Polar Research, 25(2), 123–137.

Bogorodsky, V., Bentley, C., and Gudmansen, P., 1985. Radioglaciology. D. Reidel Publishing Company, Dordrecht, Holland.

Broecker, W., Bond, G., Klas, M., Clark, E., and McManus, J., 1992. Origin of the northern Atlantic's Heinrich events. Climate Dynamics, 6(3-4), 265–273.

Brown, C., Sikonia, W., Post, A., Rasmussen, L., and Meier, M., 1983. Two calving laws for grounded iceberg-calving glaciers (Abstract). Annals of Glaciology, 4, 295.

Bueler, E. and Brown, J., 2009. Shallow shelf approximation as a "sliding law" in a thermomechanically coupled ice sheet model. Journal of Geophysical Research-Earth Surface, 114, F03008.

Burgess, D. and Sharp, M., 2008. Recent changes in thickness of the Devon Island ice cap, Canada. Journal of Geophysical Research-solid Earth, 113(B7).

Clarke, G., 1987. Fast glacier flow - ice streams, surging, and tidewater glaciers. Journal of Geophysical Research-Solid Earth and Planets, 92(B9), 8835–8841.

Clarke, G., Collins, S., and Thompson, D., 1984. Flow, thermal structure, and subglacial conditions of a surge-type glacier. Canadian Journal of Earth Sciences, 21(2), 232–240.

Clarke, G. C. and Blake, E., 1991. Geometric and Thermal Evolution of A Surge-type Glacier In Its Quiescent State - Trapridge Glacier, Yukon-territory, Canada, 1969-89. Journal of Glaciology, 37(125), 158–169.

Dege, W., 1946. Das Nordostland von Spitzbergen: Studien zu einer Landeskunde (1) [in German]. Polarforschung, 16, 72–83.

Dege, W., 1947. Das Nordostland von Spitzbergen: Studien zu einer Landeskunde (2) [in German]. Polarforschung, 17, 154–163.

Dege, W., 1954. Wettertrupp Haudegen. Einde deutsche Arktisexpedition 1944/45. Brockhaus, Wiesbaden.

den Ouden, M., Reijmer, C., Pohjola, V., van de Wal, R., Oerlemans, J., and Boot, W., 2010. Stand-alone single-frequency GPS ice velocity observations on Nordenskiöldbreen, Svalbard. The Cryosphere, 4(4), 593–604.

Dowdeswell, J., 1986. Drainage-basin characteristics of Nordaustlandet ice caps, Svalbard. Journal of Glaciology, 32(110), 31–38.

Dowdeswell, J., 1989. On the Nature of Svalbard Icebergs. Journal of Glaciology, 35(120), 224–234.

Dowdeswell, J., Drewry, D., Cooper, A., Gorman, M., Liestøl, O., and Orheim, O., 1986. Digital mapping of the Nordaustlandet ice caps from airborne geophysical investigations. Annals of Glaciology, 8, 51–58.

Dowdeswell, J. and Evans, S., 2004. Investigations of the form and flow of ice sheets and glaciers using radio-echo sounding. Reports on Progress in Physics, 67, 1821–1861.

Dowdeswell, J., G.S., H., and Hagen, J., 1991. The duration of the active phase on surge-type glaciers: contrasts between Svalbard and other regions. Journal of Glaciology, 37(127), 388–400.

Dowdeswell, J. A., Benham, T. J., Strozzi, T., and Hagen, J. O., 2008. Iceberg calving flux and mass balance of the Austfonna ice cap on Nordaustlandet, Svalbard. Journal of Geophysical Research-Earth Surface, 113(F3), F03022.

Dowdeswell, J. A., Unwin, B., Nuttall, A. M., and Wingham, D. J., 1999. Velocity structure, flow instability and mass flux on a large Arctic ice cap from satellite radar interferometry. Earth and Planetary Science Letters, 167(3-4), 131–140.

Dunse, T., Eisen, O., Helm, V., Rack, W., Steinhage, D., and Parry, V., 2008. Characteristics and small-scale variability of GPR signals and their relation to snow accumulation in Greenland's percolation zone. Journal of Glaciology, 54(185), 333–342.

Dyurgerov, M. and Meier, M., 2005. Glaciers and the changing Earth system: A 2004 snapshot, volume 58. Inst. of Arctic and Alpine Res. Univ. of Colorado, Boulder, Colorado.

Eiken, T., Hagen, J. O., and Melvold, K., 1997. Kinematic GPS survey of geometry changes on Svalbard glaciers. Annals of Glaciology, Vol 24, 1997, 24, 157–163.

Eisen, O., Harrison, W. D., Raymond, C. F., Echelmeyer, K. A., Bender, G. A., and Gorda, J. L. D., 2005. Variegated Glacier, Alaska, USA: a century of surges. Journal of Glaciology, 51(174), 399–406.

Eisen, O., Hofstede, C., Miller, H., Kristoffersen, Y., Blenkner, R., Lambrecht, A., and Mayer, C., 2010. A new approach for exploring ice sheets and sub-ice geology. Eos Trans. AGU, 91(46), 429–430.

Ekman, S. R., 1971. Seismic Investigations on the Nordaustlandet Ice Caps. Geografiska Annaler. Series A, Physical Geography, 53(1), pp. 1–13.

Evans, S., 1963. Radio techniques for the measurement of ice thickness. The Polar Record, 11(75), 406–411.

Førland, E., Hanssen-Bauer, I., and Nordli, P., 1997. Climate statistics & longterm series of temperature and precipitation at Svalbard and Jan Mayen. Technical report, Norwegian Meteorological Institute,. DNMI-report No. 02/97. 45 pp.

Gilpin, R., 1979. Model of the Liquid-like Layer Between Ice and A Substrate With Applications To Wire Regulation and Particle Migration. Journal of Colloid and Interface Science, 68(2), 235–251.

Glen, A. R., 1937. The Oxford University Arctic Expedition, North East Land, 1935-36. The Geographical Journal, 90(3), pp. 193–222.

Glen, A. R., 1939. The Glaciology of North East Land. Geografiska Annaler, 21, pp. 1–38.

Goldsby, D. L. and Kohlstedt, D. L., 2001. Superplastic deformation of ice: Experimental observations. Journal of Geophysical Research-Solid Earth, 106(B6), 11017–11030.

Greve, R., 1997. A continuum-mechanical formulation for shallow polythermal ice sheets. Philosophical Transactions of the Royal Society London A, 355(1726), 921–974.

Greve, R. and Blatter, H., 2009. Dynamics of Ice Sheets and Glaciers. Springer, Berlin, Germany etc.

Hagen, J., Eiken, T., Kohler, J., and Melvold, K., 2005. Geometry changes on Svalbard glaciers: mass-balance or dynamic response? Annals of Glaciology, 42, 255–261.

Hagen, J., Liestøl, O., Roland, E., and Jørgensen, T., 1993. Glacier Atlas of Svalbard and Jan Mayen. Norsk Polarinstitutt, Oslo, Norway.

Hagen, J. O., Kohler, J., Melvold, K., and Winther, J. G., 2003. Glaciers in Svalbard: mass balance, runoff and freshwater flux. Polar Research, 22(2), 145–159.

Hamilton, G. S. and Dowdeswell, J. A., 1996. Controls on glacier surging in Svalbard. Journal of Glaciology, 42(140), 157–168.

Heinrich, H., 1988. Origin and Consequences of Cyclic Ice Rafting In the Northeast Atlantic-ocean During the Past 130,000 Years. Quaternary Research, 29(2), 142–152.

Helsen, M. M., van den Broeke, M. R., van de Wal, R. S. W., van de Berg, W. J., van Meijgaard, E., Davis, C. H., Li, Y. H., and Goodwin, I., 2008. Elevation changes in Antarctica mainly determined by accumulation variability. Science, 320(5883), 1626–1629.

Hjort, C., Mangerud, J., Adrielsson, L., Bondevik, S., Landvik, J. Y., and Salvigsen, O., 1995. Radiocarbon dated common mussels Mytilus edulis from eastern Svalbard and the Holocene marine climatic optimum. Polar Research, 14(2), 239–243.

Hofmann-Wellenhof, B., Lichtenegger, H., and Wasle, E., 2008. GNSS Global Navigation Satellite Systems: GPS, GLONASS, Galileo, and more. Springer, Wien.

Humlum, O., Instanes, A., and Sollid, J. L., 2003. Permafrost in Svalbard: a review of research history, climatic background and engineering challenges. Polar Research, 22(2), 191–215.

Hutter, K., 1983. Theoretical Glaciology: Material Science of Ice and the Mechanics of Glaciers and Ice Sheets. D. Reidel Publishing Company, Dordrecht, The Netherlands.

Ignatieva, I. Y. and Macheret, Y. Y., 1991. Evolution of Nordaustlandet Ice Caps In Svalbard Under Climate Warming. International Association of Hydrological Sciences Publications (Symposium at St Petersburg 1990–Glaciers-Ocean-Atmosphere Interactions), 208, 301–312.

Isaksson, E., Kohler, J., Pohjola, V., Moore, J., Igarashi, M., Karlof, L., Martma, T., Meijer, H., Motoyama, H., Vaikmae, R., and van de Wal, R. S. W., 2005. Two ice-core delta O-18 records from Svalbard illustrating climate and sea-ice variability over the last 400 years. Holocene, 15(4), 501–509.

Jacobel, R. and Hodge, S., 1995. Radar internal layers from the Greenland summit. Geophysical Research Letters, 22(5), 587–590.

Jezek, K., Gogineni, P., and Shanableh, M., 1994. Radar Measurements of Melt Zones on the Greenland Ice Sheet. Geophysical Research Letters, 21(1), 33–36.

Jiskoot, H., Murray, T., and Boyle, P., 2000. Controls on the distribution of surge-type glaciers in Svalbard. Journal of Glaciology, 46(154), 412–422.

Kaakinen, A., Salonen, V. P., Kubischta, F., Eskola, K. O., and Oinonen, M., 2009. Weichselian glacial stage in Murchisonfjorden, Nordaustlandet, Svalbard. Boreas, 38(4), 718–729.

Kamb, B., 1987. Glacier Surge Mechanism Based On Linked Cavity Configuration of the Basal Water Conduit System. Journal of Geophysical Research-Solid Earth and Planets, 92(B9), 9083–9100.

Kanagaratnam, P., Gogineni, S., Gundestrup, N., and Larsen, L., 2001. High Resolution radar mapping of internal layers at the North Greenland Ice Core Project. Journal of Geophysical Research, 106(D24), 33,799–33,811.

Kaser, G., Cogley, J. G., Dyurgerov, M. B., Meier, M. F., and Ohmura, A., 2006. Mass balance of glaciers and ice caps: Consensus estimates for 1961-2004. Geophysical Research Letters, 33(19).

King, M., 2004. Rigorous GPS data-processing strategies for glaciological applications. Journal of Glaciology, 50(171), 601–607.

Kleiber, H. P., Knies, J., and Niessen, F., 2000. The Late Weichselian glaciation of the Franz Victoria Trough, northern Barents Sea: ice sheet extent and timing. Marine Geology, 168(1-4), 25–44.

Kohler, J., Moore, J., Kennett, M., Engeset, R., and Elvehøy, H., 1997. Using ground-penetrating radar to image previous years' summer surfaces for mass-balance measurements. Annals of Glaciology, 24, 355–360.

Kotlyakov, V. and Macheret, Y., 1987. Radio-echo sounding of sub-polar glaciers in Svalbard: some problems and results of Soviet Studies. Annals of Glaciology, 9, 151–159.

Kotlyakov, V. M., Arkhipov, S. M., Henderson, K. A., and Nagornov, O. V., 2004. Deep drilling of glaciers in Eurasian Arctic as a source of paleoclimatic records. Quaternary Science Reviews, 23(11-13), 1371–1390.

Kovacs, A., Gow, A., and Morey, R., 1995. The in-situ dielectric constant of polar firn revisited. Cold Regions Science and Technology, 23, 245–256.

Landvik, J. Y., Bondevik, S., Elverhoi, A., Fjeldskaar, W., Mangerud, J., Salvigsen, O., Siegert, M. J., Svendsen, J. I., and Vorren, T. O., 1998. The last glacial maximum of Svalbard and the Barents Sea area: Ice sheet extent and configuration. Quaternary Science Reviews, 17(1-3), 43–75.

Lauritzen, Ø. and Ohta, Y., 1984. Geological map of Svalbard, 1:500 000, Sheet 4G, Nordaustlandet. Norsk Polarinstitutt, Skrifter, 154 D, 14pp., 1 map.

Lefauconnier, B. and Hagen, J., 1991. Surging and Calving Glaciers in Eastern Svalbard. Norsk Polarinstitutt, Oslo, Norway.

Lefauconnier, B., Hagen, J., and Rudant, J., 1994. Flow Speed and Calving Rate of Kongsbreen Glacier, Svalbard, Using Spot Images. Polar Research, 13(1), 59–65.

Leslie, E. (Ed.), 1879. The Arctic voyages of Adolf Erik Nordenskjöld. Macmillan, London.

Li, J., Zwally, H. J., and Comiso, J. C., 2007. Ice-sheet elevation changes caused by variations of the firn compaction rate induced by satellite-observed temperature variations (1982-2003).

Liestøl, O., 1969. Glacier Surges In West Spitsbergen. Canadian Journal of Earth Sciences, 6(4P2), 895–&.

Liestøl, O., 1976. Pingos, springs and permafrost in Spitsbergen. Årbok Norsk Polarinstitutt 1975, pp. 7–29.

Loeng, H., 1991. Features of the Physical Oceanographic Conditions of the Barents Sea. Polar Research, 10(1), 5–18.

Luncke, B., 1949. Norges Svalbard- og Ishavs-undersøkelsers kartarbeider og anvendelsen fra skrå-photogrammer tatt fra fly. Norsk Polarinstitutt Medd., 68, 17 pp.

MacAyeal, D., 1993. Binge/purge oscillations of the Laurentide Ice Sheet as a cause of the North Atlantic's Heinrich events. Paleoceanography, 8(6), 775–784.

Macheret, Y., Bobrova, L., and Sankina, L., 1991. Volumetric hydrothermal state and regime of the Spitsbergen glaciers from airborne radio-echo sounding [In Russian with English summary]. Data of Glaciological Studies, 71, 40–53.

Macheret, Y. and Vasilenko, E., 1988. Pecularities of internal structure and regime of glaciers on Nordaustlandet by airborne radio-echo sounding data [In Russian with English summary]. Data of Glaciological Studies, 62, 44–56.

Meier, M. and Post, A., 1987. Fast tidewater glaciers. Journal of Geophysical Research-Solid Earth and Planets, 92(B9), 9051–9058.

Meier, M. F., Dyurgerov, M. B., Rick, U. K., O'Neel, S., Pfeffer, W. T., Anderson, R. S., Anderson, S. P., and Glazovsky, A. F., 2007. Glaciers dominate Eustatic sea-level rise in the 21st century. Science, 317(5841), 1064–1067.

Moholdt, G., Hagen, J., Eiken, T., and Schuler, T., 2010a. Geometric changes and mass balance of the Austfonna ice cap, Svalbard. The Cryosphere, 4(1), 21–34.

Moholdt, G., Nuth, C., J.O.Hagen, and Kohler, J., 2010b. Recent elevation changes of Svalbard glaciers derived from ICESat laser altimetry. Remote Sensing of Environment, 114, 2756–2767.

Morland, L., 1984. Thermomechanical balances of ice-sheet flows. Geophysical and Astrophysical Fluid Dynamics, 29(3), 237–266.

Murray, T., Stuart, G., Miller, P., Woodward, J., Smith, A., Porter, P., and Jiskoot, H., 2000. Glacier surge propagation by thermal evolution at the bed. Journal of Geophysical Research-Solid Earth, 105(B6), 13491–13507.

Nature 20, 1879. Nordenskjöld's Arctic Voyages. Nature, 20, 631–637.

Nick, F., Van der Veen, C., Vieli, A., and Benn, D., 2010. A physically based calving model applied to marine outlet glaciers and implications for the glacier dynamics. Journal of Glaciology, 56(199), 781–794.

Nordli, Ø. and Kohler, J., 2004. The early 20th century warming - Daily observations at Grønfjorden and Longyearbyen on Spitsbergen (2nd edition). Klima, Report No. 12/03.

Nuth, C., Moholdt, G., Kohler, J., Hagen, J., and Kääb, A., 2010. Svalbard glacier elevation changes and contribution to sea level rise. Journal of Geophysical Research, 115, F01008.

Nye, J., 1957. The Distribution of Stress and Velocity In Glaciers and Ice-sheets. Proceedings of the Royal Society of London Series A-mathematical and Physical Sciences, 239(1216), 113–133.

Paren, J. and Robin, G. d. Q., 1975. Internal reflections in polar ice sheets. Journal of Glaciology, 14(71), 251–259.

Paterson, W., 1994. The Physics of Glaciers. Elsevier Science Ltd, Oxford, UK, third edition.

Pfeffer, W. and Humphrey, N., 1996. Determination of timing and location of water movement and ice-layer formation by temperature measurements in sub-freezing snow. Journal of Glaciology, 42(141), 292–304.

Pinglot, J., Hagen, J., Melvold, K., Eiken, T., and Vincent, C., 2001. A mean net accumulation pattern derived from radioactive layers and radar soundings on Austfonna, Nordaustlandet, Svalbard. Journal of Glaciology, 47(159), 555–566.

Rabus, B. T. and Echelmeyer, K. A., 1998. The mass balance of McCall Glacier, Brooks Range, Alaska, USA; its regional relevance and implications for climate change in the Arctic. Journal of Glaciology, 44(147), 333–351.

Raymond, C., 1987. How do glaciers surge - a review. Journal of Geophysical Research-Solid Earth and Planets, 92(B9), 9121–9134.

Reeh, N., 2008. A nonsteady-state firn-densification model for the percolation zone of a glacier. Journal of Geophysical Research-Earth Surface, 113(F3), F03023.

Richardson-Näslund, C. and Holmlund, P., 1999. Spatial variablility in shallow snow-layer depths in central Dronning Maud Land, East Antarctica. Annals of Glaciology, 29, 10–16.

Ritz, C., 1987. Time dependent boundary conditions for temperature fields in ice sheets. In: Waddin, E. and Walder, J. (Eds.), The Physical Basis of Ice Sheet Modelling, number IAHS Publication No. 170, Wallingford, UK. IAHS Press.

Salvigsen, O., 1978. Holocene emergence and finds of pumice, whalebones, and driftwood at Svartknausflya, Nordaustlandet. Norsk Polarinst. Årbok 1977, pp. 217–228.

Sand, K., Winther, J. G., Marechal, D., Bruland, O., and Melvold, K., 2003. Regional variations of snow accumulation on Spitsbergen, Svalbard, 1997-99. Nordic Hydrology, 34(1-2), 17–32.

Sandford, K. S., 1929. The Glacial Conditions and Quaternary History of North-East Land. The Geographical Journal, 74(5), pp. 451–470.

Schuler, T., Crochet, P., Hock, R., Jackson, M., Barstad, I., and Johannesson, T., 2008. Distribution of snow accumulation on the Svartisen ice cap, Norway, assessed by a model of orographic precipitation. Hydrological Processes, 22(19), 3998–4008.

Schuler, T., Loe, E., Taurisano, A., Eiken, T., Hagen, J., and Kohler, J., 2007. Calibrating a surface mass-balance model for Austfonna ice cap, Svalbard. Annals of Glaciology, 46, 241–248.

Schytt, V., 1964. Scientific results of the Swedish glaciological expedition to Nordaustlandet, Spitsbergen, 1957 and 1958. Geografiska Annaler, 46(3), pp. 242–281.

Schytt, V., 1969. Some comments on glacier surges In eastern Svalbard. Canadian Journal of Earth Sciences, 6(4P2), 867–871.

Serreze, M. C., Carse, F., Barry, R. G., and Rogers, J. C., 1997. Icelandic low cyclone activity: Climatological features, linkages with the NAG, and relationships with recent changes in the Northern Hemisphere circulation. Journal of Climate, 10(3), 453–464.

Serreze, M. C., Walsh, J. E., Chapin, F. S., Osterkamp, T., Dyurgerov, M., Romanovsky, V., Oechel, W. C., Morison, J., Zhang, T., and Barry, R. G., 2000. Observational evidence of recent change in the northern high-latitude environment. Climatic Change, 46(1-2), 159–207.

Shreve, R., 1984. Glacier sliding at subfreezing temperatures. Journal of Glaciology, 30(106), 341–347.

Sinisalo, A., Grinsted, A., Moore, J., Kärkäs, E., and Petterson, R., 2003. Snow-accumulation studies in Antarctica with ground-penetrating radar using 50, 100 and 800 MHz antenna frequencies. Annals of Glaciology, 37, 194–198.

Smith, R. B. and Barstad, I., 2004. A linear theory of orographic precipitation. Journal of the Atmospheric Sciences, 61(12), 1377–1391.

Solheim, A., 1986. Submarine evidence of glacier surges. Polar Research, 4, 91–95.

Solheim, A., 1991. The depositional environment of surging sub-polar tidewater glaciers: a case study of the morphology, sedimentation and sediment properties in a surgeaffected marine basin outside Nordaustlandet, the Northern Barents Sea. Skrifter - Norsk Polarinstitutt, 194, 5–97.

Solheim, A. and Pfirman, S. L., 1985. Sea-floor morphology outside a grounded, surging glacier - Bråsvellbreen, Svalbard. Marine Geology, 65(1-2), 127–143.

Solomon, S., Qin, D., Manning, M., Chen, Z., Marquis, M., Averyt, K., Tignor, M., and Miller, H.L. (eds.), 2007. Climate Change 2007: The Physical Science Basis. Contribution of Working Group I to the Fourth Assessment Report of the Intergovernmental Panel on Climate Change. Cambridge University Press, Cambridge, United Kingdom and New York, NY, USA.

Sund, M., Eiken, T., Hagen, J., and Kääb, A., 2009. Svalbard surge dynamics derived from geometric changes. Annals of Glaciology, 50(52), 50–60.

Taurisano, A., Schuler, T., Hagen, J., Eiken, T., Loe, E., Melvold, K., and Kohler, J., 2007. The distribution of snow accumulation across the Austfonna ice cap, Svalbard: direct measurements and modelling. Polar Research, 26(1), 7–13.

Thompson, H., 1953. Oxford expeditions to Nordaustlandet (Northeast Land), Spitzbergen. Arctic, 6, 213–232.

Tiuri, M., Sihvola, A., Nyfors, E., and Hallikainen, M., 1984. The complex dielectric constant of snow at microwave frequencies. Journal of Oceanographic Engeniering, OE-9(5), 377–382.

Tsukernik, M., Kindig, D. N., and Serreze, M. C., 2007. Characteristics of winter cyclone activity in the northern North Atlantic: Insights from observations and regional modeling. Journal of Geophysical Research-atmospheres, 112(D3), D03101.

Unwin, B. and Wingham, D., 1997. Topography and dynamics of Austfonna, Nordaustlandet, Svalbard, from SAR interferometry. Annals of Glaciology, Vol 24, 1997, 24, 403–408.

van der Veen, C., 1996. Tidewater calving. Journal of Glaciology, 42(141), 375–385.

Vasilenko, E., Navarro, F., Dunse, T., Eiken, T., and Hagen, J., 2010. New low-frequency radio-echo soundings of Austfonna ice cap, Svalbard. In: Ahlstrøm, A. and Sharp, M. (Eds.), The Dynamics and Mass Budget of Arctic Glaciers. Extended abstracts. Workshop and GLACIODYN (IPY) meeting, 16−19 February 2009, Kananaskis, Canada., volume 127 of Danmarks og Grønlands geologiske undersøkelse rapport. GEUS, Copenhagen: IASC Working Group on Arctic Glaciology.

Vieli, A., Funk, M., and Blatter, H., 2001. Flow dynamics of tidewater glaciers: a numerical modelling approach. Journal of Glaciology, 47, 595–606.

Winther, J. G., Bruland, O., Sand, K., Killingtveit, A., and Marechal, D., 1998. Snow accumulation distribution on Spitsbergen, Svalbard, in 1997. Polar Research, 17(2), 155–164.

Wolff, E., 2000. Electrical stratigraphy of polar ice cores: principles, methods, and findings. In: Hondoh, T. (Ed.), Physics of Ice Core Records. International Symposium on Physics of Ice Core Records, 14–17 September 1998, Shikotsukohan, Japan, pp. 155–184, Kita 9, Nishi 8, Kita-ku, Sapporo 060-0809, Japan. Hokkaido University Press.

Zagorodnov, V. and Arkhipov, S., 1990. Studies of structure, composition and temperature regime of sheet glaciers of Svalbard and Severnaya Zemlya : methods and outcomes. Bulletin of glacier research, 8, 19–28.

Zagorodnov, V., Sinkevich, S., and Arkhipov, S., 1989a. Hydrothermal regime of the ice-divide area of Austfonna, Nordaustlandet[In Russian with English summary]. Data of Glaciological Studies, 68, 133–141.

Zagorodnov, V., Sinkevich, S., and Arkhipov, S., 1989b. Ice core express-analysis for structure and thermal regime studies of Austfonna [In Russian with English summary]. Data of Glaciological Studies, 66, 149–158.

Part II

Journal Publications

I

Recent fluctuations in the extent of the firn area of Austfonna, Svalbard, inferred from GPR*

Thorben DUNSE,[1] Thomas Vikhamar SCHULER,[1,2] Jon Ove HAGEN,[1] Trond EIKEN,[1] Ola BRANDT,[3] Kjell Arild HØGDA[4]

[1]*Department of Geosciences, University of Oslo, PO Box 1047, Blindern, NO-0316 Oslo, Norway*

E-mail: thorben.dunse@geo.uio.no

[2] *Norwegian Water Resources and Energy Directorate, PO Box 5091 Majorstua, NO-0301 Oslo, Norway*

[3]*Norwegian Polar Institute, Polar Environmental Centre, NO-9296 Tromsø, Norway*

[4]*Norut IT, PO Box 6434, Forskningsparken, NO-9294 Tromsø, Norway*

ABSTRACT. In spring during 2004–07 we conducted ground-penetrating radar (GPR) measurements on the Austfonna ice cap, Svalbard, with the original aim of mapping the thickness and distribution of winter snow. Here, we further exploit the information content of the data and derive a multi-year sequence of glacier-facies distribution that provides valuable spatial information about the total surface mass balance (SMB) of the ice cap, beyond the usually evaluated winter balance. We find that following an initial decrease in the extent of the firn area (2003–04), the firn line lowered within two subsequent years by ∼40–100 m elevation in the north and west and 150–230 m in the south and east of the ice cap, corresponding to a lateral expansion of the firn area along the profiles by up to 7.3 and 13.3 km, respectively. The growth of the firn area is in line with stake measurements from Etonbreen that indicate a trend towards less negative SMB over the corresponding period.

I.1 Introduction

Mass losses from glaciers and ice caps outside Antarctica and Greenland are estimated to have accounted for 0.50 ± 0.18 mm a^{-1} of the observed rate of global sea-level rise from 1961 to 2003 and 0.77 ± 0.22 mm a^{-1} for the period 1993-2003 alone (Solomon *et al.*,

* Annals of Glaciology 50(50), 155–162, 2009.

2007). The large uncertainty associated with these estimates calls for more accurate and spatially distributed measurements of glacier mass balance.

In order to cover the entire polar regions, surface mass-balance (SMB) observations are carried out from space (Zwally *et al.*, 2005; Shepherd and Wingham, 2007). One standard method to determine mass changes is provided by satellite radar altimetry. Surface elevation measurements are taken over several time intervals to yield volume changes (Wingham *et al.*, 2001). However, this technique is sensitive to ice topography and radar returns from beneath the surface (Scott *et al.*, 2006) and relies on ground-truth data. Volume backscatter that originates from inhomogeneities within the snow and firn leads to ambiguities in the detection of the surface reflection. Furthermore, knowledge of variations in snow and firn density is critical for accurate conversion of volume changes to mass changes. Both factors need particular consideration in areas where meltwater retention by refreezing is significant and highly variable in space and time.

The SMB of a glacier is reflected in the spatial distribution of its glacier facies. Following the usual textbook definition by Paterson (1994), areas exclusive of snow melt are referred to as dry snow facies, generally restricted to the interior of Greenland and Antarctica. The upper accumulation area of Arctic ice caps typically consists of the percolation facies. Here, surface melt occurs during the summer period and meltwater produced at the surface (or rain) infiltrates into the snow, where it refreezes. If, by end of the summer, the entire snowpack reaches pressure melting point, the area is referred to as wet snow facies. Here, meltwater might percolate below the last summer surface (LSS) into older layers of firn. The combined area of wet snow, percolation and, where applicable, dry snow facies, is often referred to as firn area. Below the lower boundary of the firn area lies the superimposed ice (SI) facies, i.e. ice, formed at the base of the snowpack on top of impermeable cold ice, whereas ice layers, lenses and glands within the snow and firn are termed internal accumulation (Hagen and Reeh, 2004).

For many Arctic glaciers, accumulation by internal refreezing and SI formation may be spatially and temporally highly variable, but generally represents a significant contribution to the SMB (Woodward *et al.*, 1997; Hagen *et al.*, 2003). This variability is expressed by changes of the glacier-facies distribution, and emphasizes the importance of ground truth data for analysis of space-borne data, especially if collected over Arctic glaciers and ice caps. As glacier facies arise from metamorphism and ablation of the winter snow, they relate to both winter and summer conditions.

Field studies of SMB often involve ground-penetrating radar (GPR) surveys at antennae frequencies ∼400-1500 MHz (P and L-band) with the primary goal of mapping the

distribution of snow (Kohler *et al.*, 1997; Taurisano *et al.*, 2007). The density contrast at the LSS causes an internal reflection horizon (IRH) that can be tracked along continuous profiles. Given adequate post-processing of the data, GPR also enables detailed studies of the near-surface firn stratigraphy (e.g. Dunse *et al.*, 2008) and provides a non-destructive method of mapping glacier facies (Wadham *et al.*, 2006; Brandt *et al.*, 2008). This technique has been used for validation of glacier facies inferred from synthetic-aperture radar (SAR) data (Langley *et al.*, 2007; Langley, 2007), but has not yet been directly applied as a tool of glacier monitoring.

In this study we present GPR data collected at 800 MHz along some 250 km of profiles across the Austfonna ice cap. We re-analyse GPR data from spring 2004 and 2005, published by Taurisano *et al.* (2007), and extend their time series by including measurements from spring 2006 and 2007. For each year, the thickness of the winter snow is mapped and the glacier facies beneath the winter snow are identified. In doing so, we produce a multi-year sequence of glacier-facies distribution.

I.2 Study Site

Austfonna is a polythermal ice cap, situated on Nordaustlandet, Svalbard. Centered at 79.7° N, 24.0° E it covers an area of 8120 km^2 (Fig. I.1). The ice cap has a simple dome-shaped topography with well defined drainage basins, several of which exhibit surge-type behaviour (Hagen *et al.*, 1993; Dowdeswell *et al.*, 1999). The maximum elevation of about 800 m a.s.l. in the central part coincides with the maximum ice thickness of about 580 m (Dowdeswell, 1986). Twenty-eight percent of Austfonna's bed lies below sea level and it is calving into the Barents Sea along a large portion of its boundary.

A number of investigations have been made during previous years with the focus on elevation changes and mass balance. Pinglot *et al.* (2001) inferred the annual mean SMB of the accumulation area of Austfonna for the period 1986 to 1998/99 from shallow ice cores dated by the detected radio-active fallout horizon from the Chernobyl accident. Maximum values of $\sim$0.5 m w.e. a^{-1} were measured in the summit area. Taurisano *et al.* (2007) mapped the winter snow cover using GPR data collected in spring 1999, 2004 and 2005. Like Pinglot *et al.* (2001), they found an asymmetry in SMB, in accordance to the distribution of snow, with twice as much accumulation in the southeast than as the northwest. Both studies conclude that this pattern results from the proximity of the Barents Sea in the east-southeast, providing a significant moisture source for precipitation. Taurisano *et al.* (2007) related snow thickness to all three spatial coordinates by multiple

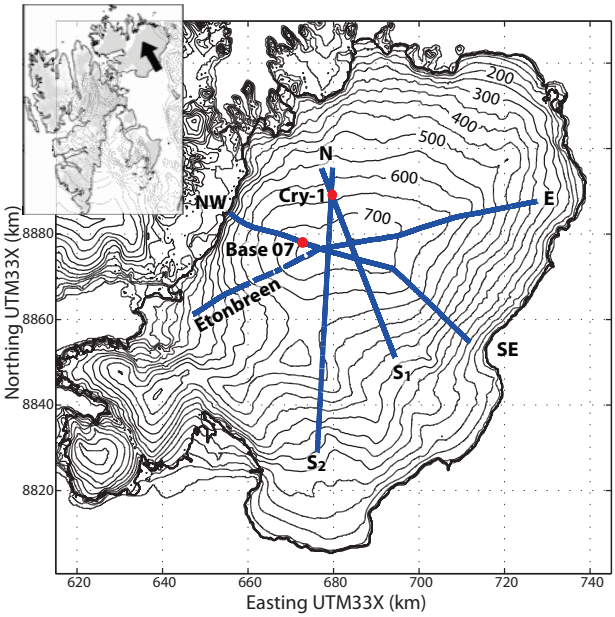

Figure I.1: Map of the Austfonna ice cap on Nordaustlandet. The blue lines indicate the GPR transects measured in 2007, while the red markers show the location of the base camp in 2007 and of study site Cry-1. The inset shows the location of Nordaustlandet within the Svalbard archipelago.

regression to derive an accumulation index for further use in a SMB model by Schuler *et al.* (2007). The distribution of snow across Austfonna is thus relatively well understood, whereas the fate of the snow throughout the summer-melt season is only known at a few points from shallow cores and mass balance stakes. Therefore, large uncertainties remain concerning the spatial and temporal variability of the firn-area extent, as well as the formation of SI and, hence, estimates of the equilibrium-line altitude (ELA).

Using airborne laser altimetry conducted in 1996 and 2002, Bamber *et al.* (2004) showed that Austfonna is thinning at lower elevations and thickening in the interior, and explained this by an increase in accumulation. Hagen *et al.* (2005) pointed out that elevation changes may be driven by both surface processes (accumulation and ablation) or ice dynamics (possible build-up towards surge activity). Bevan *et al.* (2007) suggested that slow ice dynamics is the key factor for the positive mass balance of the accumulation area, since the actual volume flux across the equilibrium line is only half of the balance flux.

I.3 Data Acquisition and Processing

Annual field studies were conducted in spring during 2004–07 with data collection over 2 week periods in late April and early May. GPR and global positioning system (GPS) data were collected along four major transects that cross the ice cap in different orientations with a total length of about 250 km (Fig. I.1). The start and end positions along the transects differ between years by up to 5 km, while the lateral offset is generally smaller than 10 m. Due to logistical and technical problems, no GPR data were collected south and southeast of the summit in 2005 and some data gaps occurred in 2006. GPR and GPS surveys were complemented by snow pit investigations (usually two to four pits for each transect in a particular year) and manual snow-depth sounding (every ∼2 km) using ordinary avalanche probes. Snow pits were excavated down to the LSS. In the ablation and SI area, the LSS was recognized as the snow/ice interface, wile in the firn area the LSS appears as either a distinct ice layer or a transition towards large refrozen ice crystals (>3 mm). At some locations in the firn area, the snow pits were extended by 0.5 m below the LSS. The bulk density was measured at 20 cm intervals, and snow stratigraphy, temperature, crystal size and hardness were logged.

I.3.1 Ground-penetrating radar and GPS

The GPR data were collected using a commercial impulse-radar system (RAMAC, Malå GeoScience) with shielded antennae at a frequency of 800 MHz. A GPS (global navigation satellite system, GNSS) receiver was operated together with the GPR for simultaneous kinematic positioning. The GPR control unit and the GPS system were mounted on one sledge, the GPR antennae on a separate unit made of fibreglass, and pulled by a snowmobile. A driving speed of $\sim$5 m s^{-1} and a constant triggering rate of the GPR resulted in a trace interval of 0.25–0.30 m. The receiving timewindow was set to 145 ns in 2007 and 126 ns in previous years, in order to image a depth range of at least 10 m. Every trace consists of 1024 samples corresponding to a sample intervals of 0.14 ns and 0.12 ns respectively. GPS measurements were logged at a rate of 1 Hz, and post-processed using a stationary GPS as reference. The accuracy of the post-processed GPS data is estimated to be typically better than 10 cm in all three spatial coordinates. Positions of individual traces were allocated by linear interpolation between the post-processed GPS coordinates.

Post-processing of the GPR data included static correction and frequency filtering. Constant time-delay clutter and system artefacts were eliminated using a horizontal filter. For visualization and interpretation of the data a gain function (energy-decay) was applied.

During data acquisition in spring the snow was entirely at sub-freezing temperatures. The effects of liquid water on the propagation of the radar signal are therefore neglected. The wave speed v of the radar signal in dry snow was derived from the permittivity ε'_r,

$$v = \frac{c}{\sqrt{\varepsilon'_r}} ,$$

where c the speed of light in vacuum. We used the empirical relation of Kovacs *et al.* (1995) to relate snow density ($\mathrm{kg\,m^{-3}}$) to permittivity:

$$\varepsilon'_r = (1 + 0.000845\rho)^2.$$

We derive the snow thickness using the two-way travel time (TWT) of the reflection occurring at the LSS and the wave speed. In situ information on snow depth from manual soundings and snow pits ensures that the correct IRH is associated with the LSS.

The error in the depth determination of the LSS mainly arises from lateral variability of the bulk-snow density, and hence wave speed, from the applied constant velocity. In 2007, bulk densities from measurements at 14 snow pits yielded a mean value and related standard deviation of $390 \pm 21\,\mathrm{kg\,m^{-3}}$. Applying the above equations yields a wave speed of $2.25 \pm 0.03\,\mathrm{m\,\mu s^{-1}}$. Values for the other years were determined following the same procedure.

The GPR system is designed such that the centre frequency corresponds approximately to the bandwidth. The wavelength λ in firn ($\rho = 600\,\mathrm{kg\,m^{-3}}$) is $\sim$0.25 m. The theoretical resolution of $\lambda/4$ is therefore about 0.06 m. However, this is limited by the length of the transmitted wavelets, comprising two cycles (approximately 2.5 ns), as interference of partial reflections from inhomogeneities within the length of the wavelets occurs. The effective interface resolution hence equals the wavelength, which for our domain varies from 0.21 m for glacier ice ($\rho = 900\,\mathrm{kg\,m^{-3}}$) to 0.29 m for windpacked snow ($\rho = 370\,\mathrm{kg\,m^{-3}}$).

I.3.2 Additional datasets

In 2007, vertical density profiles were obtained using a neutron-scattering probe (Morris and Cooper, 2003). Measurements were made while retrieving the probe from the bottom of a borehole. A radioactive source in the probe emits fast neutrons, which are slowed down by scattering as they move through the snow, firn or ice. Density profiles were determined from the measured count rate of slow neutrons returning to a detector within the probe (Morris, 2008). The count rate depends on the characteristics of the probe, the

snow/firn/ice density, temperature and the diameter of the borehole (Hawley *et al.*, 2008). The probe has a theoretical resolution of 1 cm. However, due to the relatively low number of returning neutrons it was necessary to increase the counter length to 13 cm. This means the recorded density profile represents a running average over 13 cm and thin ice layers or other abrupt density changes will not be correctly resolved. The boreholes were located within 100 m^2 in the vicinity of the base camp (79.94° N, 24.24° E) at an elevation of 775 m a.s.l. and at Cry-1 (79.85° N, 23.80° E) at an elevation of 659 m a.s.l. (Fig. I.1). The boreholes reached depths of 8–14 m. The vertical density profiles obtained from the boreholes cover all or a major portion of the GPR depth range and serve as validation of the conclusions drawn from the GPR data.

In order to compare the field measurements with an independent dataset, we employed data from the Advanced Synthetic Aperture Radar (ASAR) instrument on board the European Space Agency satellite, Envisat. ASAR operates in both ascending and descending orbits and with different look angles and polarization combinations at a centre frequency of 5.3 GHz (C-band). We selected all scenes (approximately 80) that covered the whole of Austfonna in winter during 2005–07 (October–April). During the winter season the snow is dry and therefore has little impact on the on the C-band backscatter (Langley, 2007). The individual scenes were calibrated and geocoded using an algorithm by Norut Tromsø, Norway, (Lauknes and Malnes, 2004) resulting in multilook images with 100 m resolution in both range and azimuth. The individual scenes were then averaged to produce a single two-dimensional (2-D) backscatter image.

In 2004 a network of mass balance stakes distributed over the ice cap was established. Several stakes were successfully remeasured in the following years, enabling calculation of specific SMB values at these locations. The winter balance is given directly by the snow water equivalent of the winter snow, while the total SMB is assessed from changes in stake height above the LSS and the snow water equivalent.

I.4 Mapping of Glacier Facies

Glacier facies relate to the surface properties of a glacier and are an expression of its SMB. Wadham *et al.* (2006), Langley *et al.* (2007) and Brandt *et al.* (2008) showed the potential of the GPR to map various glacier facies.

The accumulation area is characterized by either firn or SI. On Austfonna, the firn facies consists of wet snow. In certain years, some snow in the summit area might remain at sub-freezing temperatures throughout the entire summer, and a percolation facies may

form. The ablation area is typically composed of pure glacier ice. Firn, SI and glacier ice are recognized by their characteristic signal-reflection pattern (Fig. I.2) dependent on typical occurrence and strength of dielectric contrasts (Brandt *et al.*, 2008). Due to its homogeneous properties, pure, cold glacier ice is predominantly transparent to electromagnetic waves and signal reflections barely occur. In the firn area, the strong dielectric contrast between solid-ice clusters and an often coarse-grained firn matrix causes IRHs of strong amplitudes, while a varying air-bubble content in the SI causes IRHs of lower amplitude.

We use these properties to map the facies underneath the winter snowpack: firn (F), SI and glacier ice of the ablation area (GI) (Fig. I.2). We further sub-categorize the classification F into a long-term firn area (F1); a firn layer that originates from multiple years of accumulation, but lies in a zone of recent (∼10 years) variability of the firn line (F2); and a thin firn layer that apparently originates from one accumulation season only

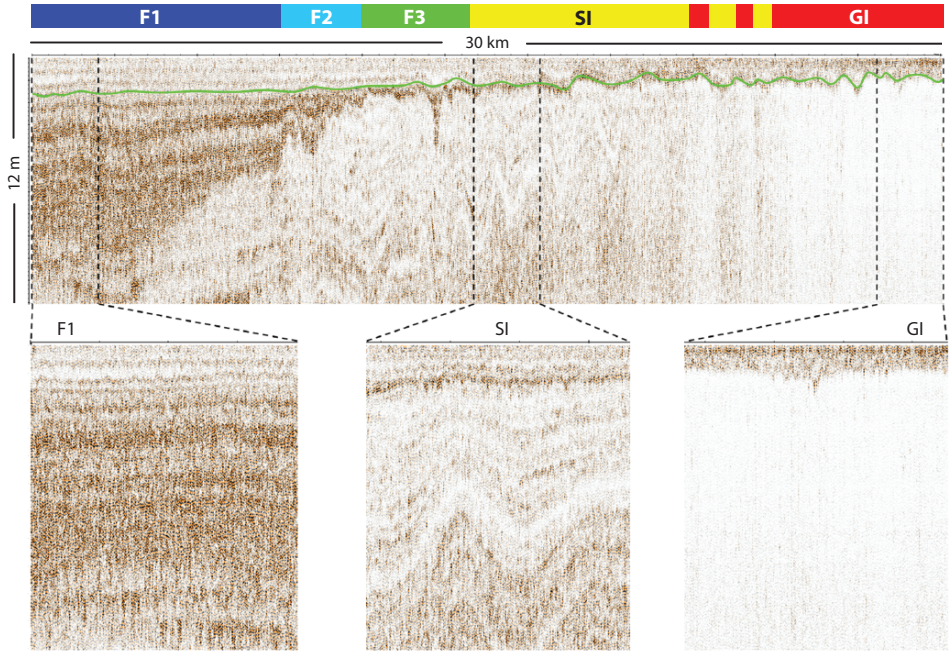

Figure I.2: GPR classification of glacier facies along a 30 km long transect from the summit area (F1) into the ablation area (GI) of Etonbreen. The green line indicates the position of the LSS. The Lower panels show close ups of 2 km GPR data with characteristic signal reflection patterns.

(F3). Regions where strong IRHs indicate firn over most of the depth range of the GPR image (6 m and more, corresponding to ∼10 or more mass-balance years) are classified as the long-term firn area. IRHs in F2 typically show a larger spatial variability than in F1 and typically converge with the LSS at lower elevations. IRHs in the SI area generally show an even larger spatial variability. The formation of SI requires ponding of free water and is therefore strongly controlled by local topography (Brandt *et al.*, 2008). According to the above definition, direct transition from F2 to SI is possible. Transition from SI to F2, on the other hand, involves at least two consecutive years of firn accumulation at a particular location. SI has to be initially covered with a thin layer of firn in one year (F3) to reach the F2 classification in the subsequent year.

In the following, the term glacier facies always relates to the glacier facies beneath the winter snowpack. GPR measurements in spring (year n) therefore yield the thickness of the winter snow accumulation (year n) and the extent of the glacier facies at the end of the previous summer (year $n-1$). Measurements of snow accumulation are related to the winter balance only. Glacier facies result from a combination of snow accumulation and subsequent metamorphism and ablation of the winter snow cover. Therefore, the above method of detecting glacier facies also provides a measure of summer conditions. In re-analysing the GPR data from 2004 to 2007, we derive a multi-year sequence of glacier-facies distribution along the transects that allows us to study their interannual fluctuations. It should be noted, that the classification of GPR data is a somewhat subjective process. However, the same processing has been applied to the entire dataset and the classification was performed by a single person to ensure consistent interpretation.

I.5 Validation

To gain more confidence in our interpretation of the GPR data, we first compare the GPR images with the vertical density profiles from neutron probing, and find a clear relation between the observed density profiles and the signal reflection pattern in the radar image. We then compare the GPR-derived glacier facies with radar zones in the SAR image of Austfonna.

I.5.1 Neutron-scattering probe

The six density profiles recovered at the base camp are shown in Figure I.3a. The site lies in an area classified as F1, the long-term firn area. The winter snowpack is characterized by

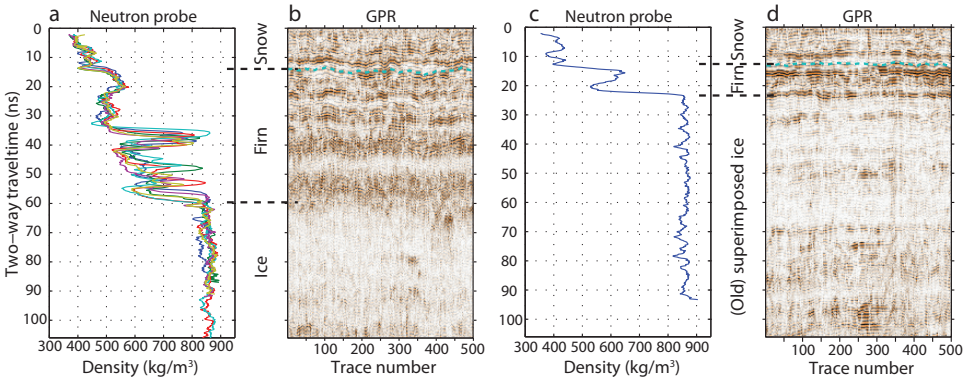

Figure I.3: Comparison of vertical density profiles, inferred from neutron-scattering probing with GPR signal reflections obtained along ∼120 m sections at (a, b) base camp and (c, d) Cry-1. The dashed lines in the GPR images indicate the position of the LSS as confirmed from snow pits and manual snow-depth soundings.

densities between 350 and 450 kg m^{-3}, in agreement with measurements in a nearby snow pit. The LSS is recognizable as a sharp density increase at approximately 14 ns TWT, corresponding to a depth of 1.7 m. The digitized LSS from GPR is at the same depth (Fig. I.3b). From the LSS down to 33 ns the densities are in the range 470–570 kg m^{-3}, which is typical for firn. Values in the range of 550–850 kg m^{-3}occur between 33 and 60 ns and indicate firn and ice layers. In the GPR image, this depth range is characterized by strong reflection amplitudes, without resolving individual IRHs. At ∼60 ns (∼6 m depth) the firn-ice transition is reached. Below this depth range, the density varies ∼860 kg m^{-3}, and the signal reflections in the GPR image are much weaker.

The classification at Cry-1, north of the summit, is F3 for summer 2005 and F2 for 2006. The neutron-probe profile reveals densities between 500 and 630 kg m^{-3} from the LSS at 13 ns down to 22 ns TWT (Fig. I.3c). Below, the density sharply increases to approximately 850 kg m^{-3} indicating the firn-ice transition at a depth of about 2.4 m. In the GPR data, the transition produces an IRH at that depth (Fig. I.3d), separating a region of strong reflection amplitudes above (firn) from lower reflection amplitudes below (ice).

I.5.2 SAR zones

To compare the backscatter zones of the SAR image with the GPR results, we plot the colour-coded glacier facies, inferred from GPR, on top of the 2-D backscatter image

(Fig. I.4). The backscatter intensities of the SAR signal represent an integral of all backscatter sources from the illuminated volume (König *et al.*, 2002). While the dry winter snow has only minor effects of the signal, the properties of the firn and ice below the LSS control the penetration depth of the signal. In the firn area, volume scatter from inclusions of solid ice clusters dominates and results in high backscatter intensities (light grey shades/white). In the ablation area, volume backscatter from relatively homogeneous glacier ice is insignificant and a distinct snow-ice interface leads to specular reflection of energy away from the side-looking instrument, resulting in low backscatter intensities (dark grey shades). SI is characterized by a varying air-bubble content that causes medium backscatter intensities.

The most striking feature of the comparison is that sections of the GPR transects classified as F1 fall within the limits of the high-backscatter area. Furthermore, the

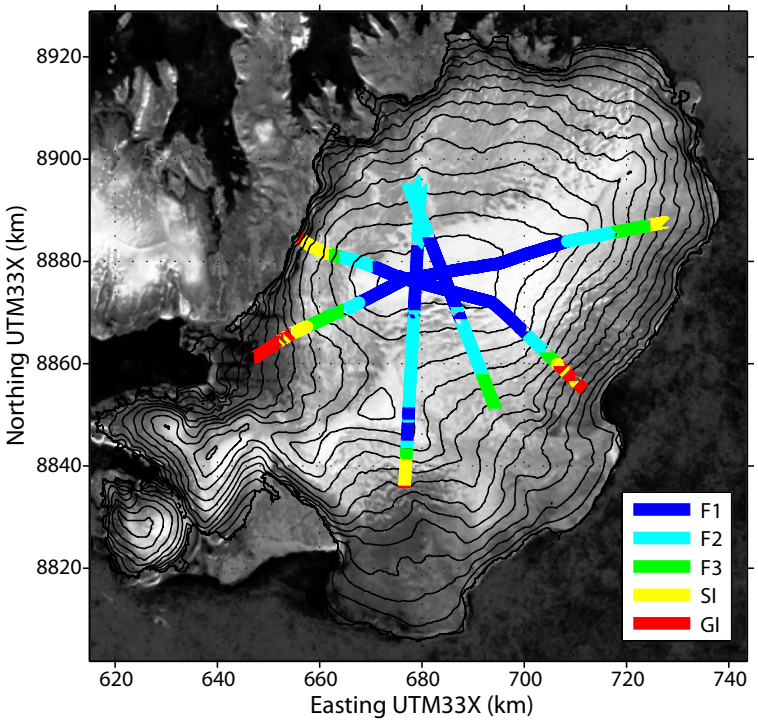

Figure I.4: Comparison of GPR-derived glacier facies distribution in summer 2006 with a 2-D backscatter SAR image. The image is an average of a number of winter scenes acquired during 2005–07.

transition between F1 and F2 coincides with the boundary that separates areas of high backscatter from areas of medium backscatter. Sections of the GPR transects classified as GI coincide with areas of low backscatter. The good agreement with the SAR data gives further confidence in the GPR-based glacier-facies classification, as previous studies have shown that SAR and GPR systems yield very similar results (Langley *et al.*, 2007; Brandt *et al.*, 2008).

I.6 Results

The observed distribution of snow accumulation in 2006 and 2007 reconfirms the asymmetric snow distribution found by Pinglot *et al.* (2001) and Taurisano *et al.* (2007). Figure I.5 shows two transects running from the western to the eastern margin. In the 4 year period 2004–07, the snow thickness typically varied from 0.5 to 1.5 m in the west, and 1.5 to 3 m in the east. The lowest snow accumulation was measured in spring 2004, with a mean

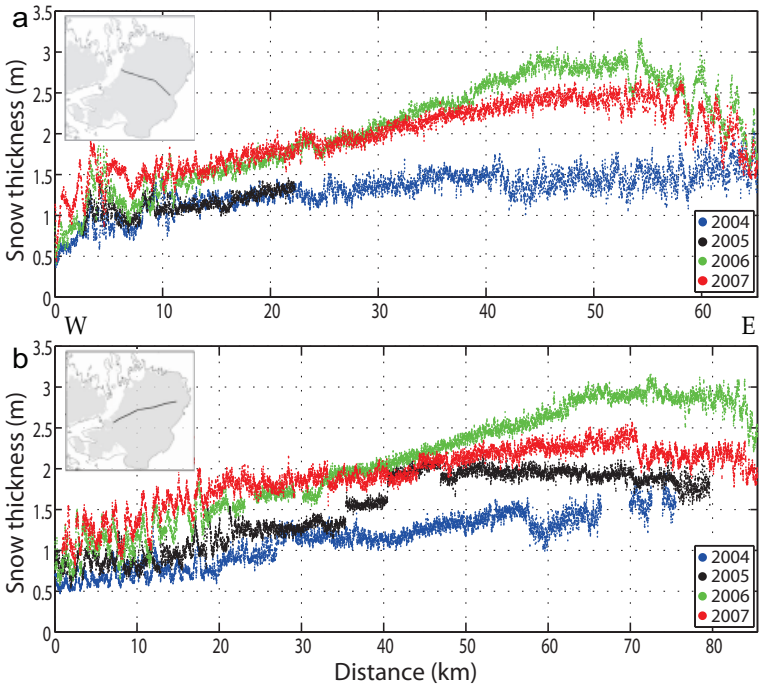

Figure I.5: Snow thickness profiles for spring 2004–07: (a) along the northwest-southeast and (b) southwest-east transect.

thickness of 1.21 m over the entire length of the two transects. In spring 2006, a mean thickness of 2.01 m was measured over the same distance.

I.6.1 Glacier facies and their temporal variation

Collected in spring during 2004–07, the GPR data yield the extent of the glacier facies at the end of the summer from 2003 to 2006. We investigate fluctuations during this period by plotting the colour-coded facies on top of a contour map of Austfonna (Fig. I.6). The most striking feature is a significant increase in the extent of the firn area, starting winter

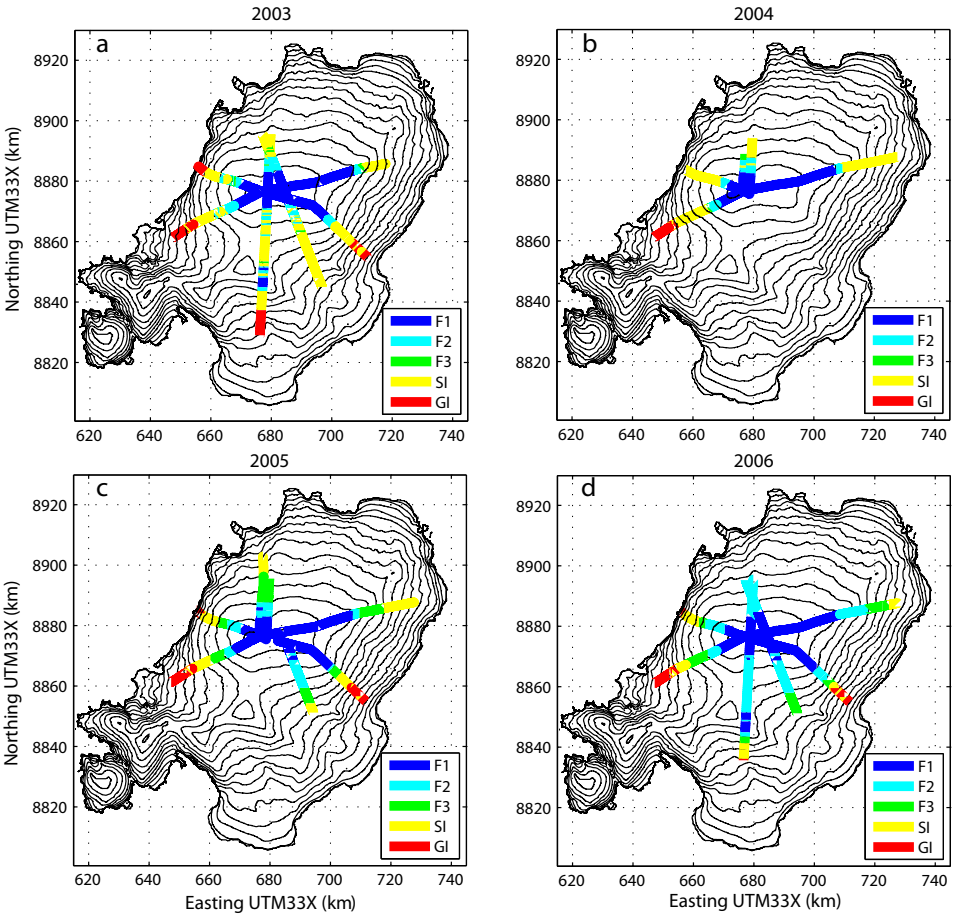

Figure I.6: Colour-coded glacier facies in end-of-summer 2003–06 along the GPR transects in spring 2004–07, plotted on top of a contour map of Austfonna with 50 m contour interval.

Table I.1: Approximate firn-line elevations along the GPR profiles from end of the summer 2003 to 2006, total change during that period and corresponding lateral expansion (estimates of the ELA from mass balance stakes on Etonbreen are given).

Profile	Firn-line elevation (m)				Difference (m)	Expansion (km)
	2003	2004	2005	2006	2006–2003	2003–2006
Eton ELA	–	650	500	470	180	8.5
Eton	650	660	590	550	100	5.2
NW	680	720	650	640	40	1.9
N	650	650	550	–	100	7.3
E	620	640	500	390	230	13.1
SE	600	–	540	450	150	6.1
$\mathbf{S}_1$	650	–	490	440	210	13.3
$\mathbf{S}_2$	650	–	–	500	150	10.6

2004/2005. In 2003 and 2004, the firn facies was confined to the summit area and SI was exposed along large portions of the transects (Fig. I.6a and b). In the subsequent two years, SI became to a large extent covered by firn (Fig. I.6c and d). We further note firn pockets (F2) within the upper parts of the SI in 2003, which were no longer present in 2004. The lower boundary and the total change of the firn area, both in vertical and lateral dimension are listed for each profile in Table I.6.1. No differentiation was made as to whether the firn originates from the previous year or not. In addition, estimates of the ELA inferred from the mass-balance stakes on Etonbreen are provided. Between 2003 and 2006, the firn line decreased by ∼40–100 m elevation in the north and west of Austfonna and 150–230 m in the south and east. This corresponds to a lateral expansion of the firn area by up to 7.3 km along profiles in the north and west and up to 13.3 km for the southern and eastern profiles.

To visualize the interannual changes in more detail, and to allow to direct comparison between measurements from different years, we select a transect along which data were collected in all years. We plot the extent of the glacier facies along the profile that runs from Etonbreen in the west via the summit towards the east (Fig. I.7). The increase of the area classified as F2 or F3 in the period summer 2004 to summer 2006 is clearly seen. For each year, a progressively larger portion of the sections classified as SI is covered by an expanding and thickening layer of firn. However, the sections with deep firn F1 show little interannual variation. This highlights the fact that F1 originates as an integral of many years of firn accumulation. The only notable change in the extent of F1 occurs between 2005 and 2006, when it advances slightly. The minimum extent of the total firn area

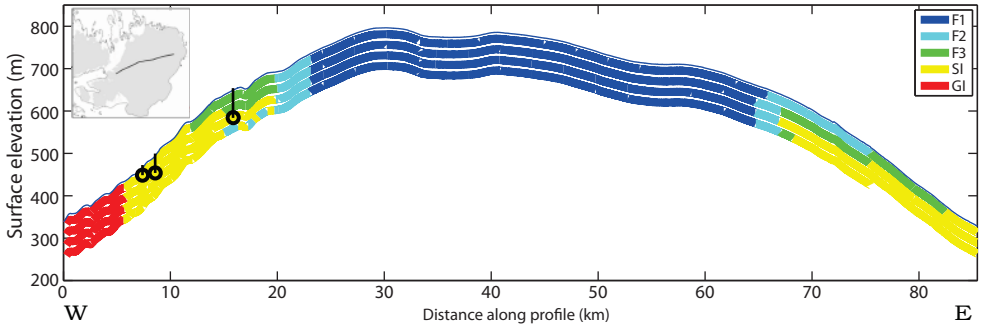

Figure I.7: Colour-coded glacier facies along the transect from Etonbreen in the west via the summit area towards the east. Each stripe represents the classification for a particular year in chronological order with 2006 at the top and 2003 at the base. Note that the thickness of the stripes are not related to the actual snow thickness or depth. Black markers indicate ELA estimates inferred from mass balance stakes on Etonbreeen for the period 2004–06.

(F1, F2 and F3) in the period summer 2003 to summer 2006 is reached in summer 2004. A large portion of SI is exposed along the transect. In 2003, several firn pockets (F2) between 1 and 3 m thick and with cross-sectional lengths of tens to hundreds of meters (likely originating from multiple years of firn accumulation) overlie the SI (15–20 km). In 2004, no such pockets were identified, indicating that they have been melted away or transformed into SI. Figure I.7 also indicates estimates of the ELA, inferred from mass balance stakes on Etonbreen, in the western part of the transect. The ELA decreased from 650 m in 2004 to 500 m in 2004 and 470 m in 2006. These elevations fall within the zone classified as SI in the corresponding year.

We also tracked characteristic IRHs within the firn over time. These represent the summer surfaces from the previous year. This analysis is not as robust as the mapping of glacier facies, but we found that the position of the IRHs in relation to the LSS remains apparently unchanged in the period spring 2004 to spring 2005. In subsequent years, the IRHs are progressively buried at a rate of the order of 1 m a^{-1}.

I.7 Concluding Remarks

Comparing the sequence of glacier-facies distribution with direct SMB measurements, we have to bear in mind some limitations on the information content of the mapped facies. Theoretically, the ELA corresponds to the lower boundary of the SI in a particular year. The fact that the ELAs from the mass balance stakes lie above the GPR-derived

transition from SI to GI (Fig. I.7) illustrates the limitation of the GPR data to pinpoint the exact position of the ELA. Although SI can be identified from the GPR data, it remains undetermined whether this is old SI and subject to ablation, or newly formed SI that contributes positively to the SMB. A similar limitation applies to detection of the recent firn line (the snow line by the end of the previous summer). In the case of a growing firn area, the firn line coincides with the lower boundary of the firn area. In the case of a shrinking firn area, as in summer 2004, the recent firn line might retreat to a position within the multi-year firn (F1 and F2) and its determination may be ambiguous. Although the position of the ELA cannot be directly inferred from an individual facies distribution, its interannual variation is captured in the multi-year sequence.

The observed increase in the extent of the firn area, beginning in summer 2004, is in line with a lowering ELA, as derived from the mass balance stakes on Etonbreen over the same time period (Table I.6.1). Between summer 2003 and summer 2006, the firn line lowered by ∼40–100 m elevation in the north and west and 150–230 m in the south and east of the ice cap, corresponding to a lateral expansion of the firn area along the profiles by up to 7.3 and 13.3 km, respectively. The apparently constant position of characteristic IRHs in spring 2004 and spring 2005 indicates that the entire winter snow has been heavily affected by summer melt, such that it is not recognizable in the GPR data. The concurrent disappearance of several firn pockets within the SI area provides further evidence of strong surface melt in summer 2004. This does not necessarily represent a complete absence of net accumulation, since it is likely that meltwater was retained through internal accumulation and SI formation.

This study demonstrates GPR as a non-destructive and useful tool to map glacier facies. As well as measuring the amount of winter snow, we obtained a multi-year sequence of glacier facies distribution. This can be interpreted in terms of SMB variations. In addition, these facies provide valuable ground-truth data for validation and interpretation of satellite radar altimetry data, such as from Envisat or the upcoming CryoSat-2.

Acknowledgements

This paper is a contribution to the International Polar Year project GLACIODYN, The dynamic response of Arctic glaciers to Global Warming and to the validation of CryoSat under the direction of Duncan Wingham (University College London). The work was funded by the Norwegian Research Council, the Norwegian Space Center, the European Space Agency and the UK Natural Environment Research Council through grant

NER/O/S/2003/00620. T. Dunse was supported through an Arktisstipend allocated by the Svalbard Science Forum. We thank E. Morris (Scott Polar Research Insitute) for placing the neutron probe at our disposal and for assistance with the data, G. Moholdt for his energetic dedication in the field (2006, 2007), A. Taurisano for collecting GPR data in 2004 and 2005 and E. Malnes (Norut) for geocoding the SAR scenes. Furthermore, we acknowledge numerous helpful comments by K. Langley and the two reviewers, A. Chapuis and M. Huss.

References

Bamber, J., Krabill, W., Raper, V., and Dowdeswell, J., 2004. Anamolous recent growth of part of a large Arctic ice cap: Austfonna, Svalbard. Geophysical Research Letters, 31(12), L12402.

Bevan, S., Luckman, A., and Murray, T., 2007. Positive mass balance during the late 20th century on Austfonna, Svalbard revealed using satellite interferometry. Annals of Glaciology, 46, 117–122.

Brandt, O., Kohler, J., and Luthje, M., 2008. Spatial mapping of multi-year superimposed ice on the glacier Kongsvegen, Svalbard. Journal of Glaciology, 54(184), 73–80.

Dowdeswell, J., 1986. Drainage-basin characteristics of Nordaustlandet ice caps, Svalbard. Journal of Glaciology, 32(110), 31–38.

Dowdeswell, J. A., Unwin, B., Nuttall, A. M., and Wingham, D. J., 1999. Velocity structure, flow instability and mass flux on a large Arctic ice cap from satellite radar interferometry. Earth and Planetary Science Letters, 167(3-4), 131–140.

Dunse, T., Eisen, O., Helm, V., Rack, W., Steinhage, D., and Parry, V., 2008. Characteristics and small-scale variability of GPR signals and their relation to snow accumulation in Greenland's percolation zone. Journal of Glaciology, 54(185), 333–342.

Hagen, J., Eiken, T., Kohler, J., and Melvold, K., 2005. Geometry changes on Svalbard glaciers: mass-balance or dynamic response? Annals of Glaciology, 42, 255–261.

Hagen, J., Liestøl, O., Roland, E., and Jørgensen, T., 1993. Glacier Atlas of Svalbard and Jan Mayen. Norsk Polarinstitutt, Oslo, Norway.

Hagen, J., Melvold, K., Pinglot, F., and Dowdeswell, J., 2003. On the net mass balance of the glaciers and ice caps in Svalbard, Norwegian Arctic. Arctic Antarctic and Alpine Research, pp. 264–270.

Hagen, J. and Reeh, N., 2004. Mass Balance of the Cryosphere: Observations and Modelling of Contemporary and Future Changes. In: Bamber, J. and Payne, A. (Eds.), In situ measurement techniques: land ice , pp. 11–41. Cambridge University Press.

Hawley, R., Brandt, O., Morris, E., Kohler, J., Shepherd, A., and Wingham, D., 2008. Instruments and Methods. Techniques for measuring high-resolution firn density profiles: a case study from Kongsvegen, Svalbard. Journal of Glaciology, 54, 463–468.

Kohler, J., Moore, J., Kennett, M., Engeset, R., and Elvehøy, H., 1997. Using ground-penetrating radar to image previous years' summer surfaces for mass-balance measurements. Annals of Glaciology, 24, 355–360.

König, M., Wadham, J., Winther, J., Kohler, J., and Nuttall, A., 2002. Detection of superimposed ice on the glaciers Kongsvegen and midre Lovenbreen, Svalbard, using SAR satellite imagery. Annals of Glaciology, 34, 335–342.

Kovacs, A., Gow, A., and Morey, R., 1995. The in-situ dielectric constant of polar firn revisited. Cold Regions Science and Technology, 23, 245–256.

Langley, K., 2007. Glacier Subsurface Interpretation Combining Ground Penetrating Radar and Satellite Synthetic Aperture Radar, Ph.D Thesis, volume 645. Faculty of Mathematics and Natural Sciences, University of Oslo.

Langley, K., Hamran, S., Høgda, K., Storvold, R., Brandt, O., Hagen, J., and Kohler, J., 2007. Use of C-band ground penetrating radar to determine backscatter sources within glaciers. Ieee Transactions On Geoscience and Remote Sensing, 45(5), 1236–1246.

Lauknes, I. and Malnes, E., 2004. Automatical geocoding of SAR products. In: Lacoste, H. and Ouwehand, L. (Eds.), Envisat and ERS Symp., pp. CD–ROM. Salzburg, Austria, Sep. 6-10, 2004.

Morris, E., 2008. A theoretical analysis of the neutron-scattering method for measuring snow and ice density. Journal of Geophysical Research, 113, F03019.

Morris, E. and Cooper, J., 2003. Density measurements in ice boreholes using neutron scattering. Journal of Glaciology, 49(167), 599–604.

Paterson, W., 1994. The Physics of Glaciers. Elsevier Science Ltd, Oxford, UK, third edition.

Pinglot, J., Hagen, J., Melvold, K., Eiken, T., and Vincent, C., 2001. A mean net accumulation pattern derived from radioactive layers and radar soundings on Austfonna, Nordaustlandet, Svalbard. Journal of Glaciology, 47(159), 555–566.

Schuler, T., Loe, E., Taurisano, A., Eiken, T., Hagen, J., and Kohler, J., 2007. Calibrating a surface mass-balance model for Austfonna ice cap, Svalbard. Annals of Glaciology, 46, 241–248.

Scott, J., Nienow, P., Mair, D., , Parry, V., Morris, E., and Wingham, D., 2006. The importance of seasonal and annual layers in controlling backscatter to radar altimeters across the percolation zone of an ice sheet. Geophysical Research Letters, 33, L24502.

Shepherd, A. and Wingham, D., 2007. Recent Sea-Level Contributions of the Antarctic and Greenland Ice Sheets. Science, 315(5818), 1529–1532.

Solomon, S., Qin, D., Manning, M., Chen, Z., Marquis, M., Averyt, K., Tignor, M., and Miller, H.L. (eds.), 2007. Climate Change 2007: The Physical Science Basis. Contribution of Working Group I to the Fourth Assessment Report of the Intergovernmental Panel on Climate Change. Cambridge University Press, Cambridge, United Kingdom and New York, NY, USA.

Taurisano, A., Schuler, T., Hagen, J., Eiken, T., Loe, E., Melvold, K., and Kohler, J., 2007. The distribution of snow accumulation across the Austfonna ice cap, Svalbard: direct measurements and modelling. Polar Research, 26(1), 7–13.

Wadham, J., Kohler, J., Hubbard, A., Nuttall, A., and Rippin, D., 2006. Superimposed ice regime of a high Arctic glacier inferred using ground-penetrating radar, flow modeling, and ice cores. Journal of Geophysical Research, 111, F01007.

Wingham, D., Forsberg, R., Laxon, S., Lemke, P., Miller, H., Raney, K., Sandven, S., Scharroo, R., Vincent, P., and Rebhan, H., 2001. CryoSat calibration and validation concept. Technical report, ESA.

Woodward, J., Sharp, M., and Arendt, A., 1997. The influence of superimposed-ice formation on the sensitivity of glacier mass balance to climate change. Annals of Glaciology, 24, 186–190.

Zwally, H., Giovinetti, M., Li, J., Cornejo, H., Beckley, M., Brenner, A., Saba, J., and Yi, D., 2005. Mass changes of the Greenland and Antacrctic ice sheets and shelves and contributions to sea-level rise: 1992-2002. Journal of Glaciology, 51(175), 509–527.

II

Continuous GPS surface velocity measurements on two fast flowing outlet glaciers of Austfonna, Svalbard

Thorben DUNSE[1], Thomas Vikhamar SCHULER[1], Jon Ove HAGEN[1],Carleen H. Reijmer[2]

[1]*Department of Geosciences, University of Oslo, P.O. Box 1047, Blindern, NO-0316 Oslo, Norway*

E-mail: thorben.dunse@geo.uio.no

[2]*Institute for Marine and Atmospheric Research, Utrecht University, Prinetonplein 5, 3584 CC Utrecht, The Netherlands*

ABSTRACT. A large part of the ice flux within Arctic ice caps occurs through spatially limited flow units that may operate in a mode of steady flow or cyclic surge behaviour. At Austfonna, the largest ice cap on Svalbard, previous ice-surface velocity maps rely on data acquired in the mid-1990s with limited information concerning the temporal variability. Despite a surface mass-balance close to zero, Austfonna has recently experienced net mass loss due to calving and retreat of the marine ice margin. We present continuous Global Positioning System (GPS) observations along the central flowlines of two fast flowing outlets of Austfonna during 2008–2010. The data shows prominent summer speed-ups with ice-surface velocities as high as 240 % of the pre-summer mean. Acceleration follows the onset of the summer melt period, indicating enhanced basal motion due to input of surface meltwater into the subglacial drainage system. In 2009, the relation between ice-surface velocities and surface melt is more complex, probably related to a transition towards a hydraulically more efficient drainage system. During 2009–2010, Basin-3 has accelerated by about 30 %, compared to 2008–2009. The observed annual mean ice-surface velocities triple those measured by InSAR in the mid 1990s and imply increased mass loss through calving of icebergs into the Barents Sea. With measured summer velocities up to 2 m d^{-1}, Basin-3 is neck and neck with Kronebreen, often referred to as the fastest glacier on Svalbard.

II.1 Introduction

Spatially limited fast-flow units are a typical feature of many Arctic ice caps and play an important role in their mass balance. Fast-flow units are responsible for most of the ice flux from the ice-cap interior/accumulation area towards the margins/ablation area. At the margin, the ice is exposed to increased surface melt (climatically forced ice mass loss). Marine-terminating outlets also loose mass through iceberg calving, to which extent depending on ice flux towards the calving front and the position change of the terminus (dynamically-forced ice mass loss). Iceberg calving allows for rapid ice mass loss that may exceed surface melt also in a warming climate. Yet, its potential contribution to eustatic sea-level rise (SLR) is excluded from the last consensus estimate (0.18–0.6 m until 2100) of the Intergovernmental Panel on Climate Change (IPCC) Fourth Assessment (Solomon *et al.*, 2007). Pfeffer *et al.* (2008) strengthens the importance of calving loss associated with increased ice flux towards the calving front, but suggested an upper limit of <2 m contribution to SLR until 2100, considering kinematic constraints.

Fast glacier flow is achieved by basal motion rather than by internal deformation and requires basal temperatures at or near the pressure-melting point. Basal motion refers to sliding of the ice base over bedrock (Clarke, 1987) or deformation of subglacial sediments (Clarke *et al.*, 1984; Tulaczyk *et al.*, 2000a). For temperate glaciers, the relation between basal motion and effective basal normal pressure, i.e. ice overburden reduced by basal water pressure, explains much of the variations on shorter timescales (hours to weeks) (Meier and Post, 1987). Excessive charge of the subglacial hydrological drainage system early in the summer melt season reduces the effective normal pressure which in turn weakens the ice-bed coupling (Iken and Bindschadler, 1986) and promotes high velocities in excess of those during winter. Early in the melt season, the basal drainage system is hydraulically inefficient and characterized by a system of interconnected cavities. A particularity of such a drainage system is that basal water pressure increases with water discharge (Walder, 1986) and consequently, water is distributed along the ice-bed interface, effectively weakening the ice-bed coupling over a large area. Given sustained input of meltwater, a hydraulically efficient drainage system consisting of large 'Röthlisberger' channels may evolve later in the melt season (Iken *et al.*, 1983; Mair *et al.*, 2001). If overcharged, a channelized system may also respond with increased water pressure, but typically, water pressure is low (Röthlisberger, 1972). Water is hence drawn from towards the major channels, the effective normal pressure increases and the bed-coupling strengthens. Recent observations underpin that a simple linear relation between sur-

face melt and glacier acceleration does not exist. Sustained input of large volumes of meltwater may hamper rather than enhance glacier motion, as recently observed in SW Greenland (Sundal *et al.*, 2011), if it permits transition from a hydraulically inefficient to an efficient drainage system in the first place. Model results confirm that a switch in the characteristics of the basal drainage system can explain such observations (Schoof, 2010b).

Nevertheless, enhanced ice-surface velocities following surface melt was reported not only for temperate glaciers, but also for the Greenland ice sheet (Zwally *et al.*, 2002) and several Arctic glaciers with polythermal/predominately cold thermal regimes (Copland *et al.*, 2003; Rippin *et al.*, 2005; Nuttall and Hodgkins, 2005). This indicates that surface meltwater may reach the bed even through a substantial layer of cold ice. Arctic glaciers usually flow at lower rates, compared to their temperate counterparts, and widespread formation of surface crevasses is less likely. Supraglacial runoff is the dominant drainage mechanism, but englacial tunnels may form by downward melting and closure from the snow and ice above (Fountain and Walder, 1998). Particular for polythermal glaciers is the presence of a thermal barrier for subglacial water flow at the transition from temperate to cold-based ice regions. At the beginning of the melt season, meltwater refreezes in the snowpack and runoff does not occur, before the cold-content of the snow (and firn) is diminished. At John Evans Glacier, Arctic Canada, glacier acceleration typically occurs one month after the onset of the summer melt season and a connection between the supraglacial and englacial/subglacial drainage system is established (Copland *et al.*, 2003). Abrupt and vigorous meltwater input may follow drainage events of supraglacial lakes, that are known to form at the surface of many Arctic glaciers during summer.

Velocity variations not only arise from effects of the subglacial hydrology. Significant calving events at the marine terminus (Thomas, 2004) or buoyancy perturbations due to ocean tides (O'Neel *et al.*, 2003) may change the backstress exerted on the upglacier ice through longitudinal stress coupling to marginal ice, indicating that non-local forces may influence the velocity at a particular location (Price *et al.*, 2008; Nick *et al.*, 2009). On long timescales (years to centuries), the geometric evolution of the glacier may become important, given that the actual ice flux differs from the balance flux required to maintain a steady state surface profile. Glacier thickening and ice-surface steepening raise the local shear stress, thereby increasing strain heating, in addition to providing increased insulation from the cold atmosphere. For polythermal glaciers, geometric changes drive changes in the extent of basal ice at or near the pressure-melting point. This in turn, controls the contribution of basal motion to the overall ice flow. Abrupt changes in basal

motion, in connection to such a thermal switch, also provides a mechanism for surge-type behaviour (Clarke, 1976; Murray *et al.*, 2000).

Direct observations of glacier flow are usually restricted to observations of surface motion. Ice-surface velocity maps of good spatial resolution can be determined by satellite radar interferometry (InSAR, e.g. Rott (2009)) or speckle/intensity tracking of SAR intensity images (Strozzi *et al.*, 2002). A disadvantage of these methods is that suitable data is only available for limited time periods. Continuous or repeated ground-based Global Positioning System (GPS) observations, yield displacement rates of specific surface points. GPS measurements hence provide velocity time series of the desired temporal resolution and at high accuracy, however, with limited information on the spatial variability.

At Austfonna, the largest ice cap on Svalbard, InSAR revealed distinct fast-flow units embedded in a slow moving bulk of the ice cap (Dowdeswell *et al.*, 1999; Bevan *et al.*, 2007). These studies rely on data acquired during the winter months of the mid 1990s. Very limited information is available on the temporal variability in glacier flow. Repeated GPS measurements of mass balance stakes are available for 1998/99 (Pinglot *et al.*, 2001) and on an annual basis since 2004, but the stakes were deployed at dynamically inactive areas. In recent years, the surface mass balance of Austfonna has been close to zero and most of the mass loss is attributed to calving from the marine ice margins (Dowdeswell *et al.*, 2008; Moholdt *et al.*, 2010a). The calving estimate of about $2.5 \pm 0.5\,\mathrm{km^3\,a^{-1}}$ w.e. published by Dowdeswell *et al.* (2008) rely on these mid 1990s surface-velocities snapshots. In the present study, we present continuous GPS-measurements along the central flowlines of two of these fast-flow units, namely Duvebreen and Basin-3. The present GPS records span a two-year time period, and allow investigation of seasonal and year-to-year changes in flow velocities. Basin-3 was reported to have undergone a short-lived flow-instability or mini-surge in the early 1990s (Dowdeswell *et al.*, 1999). We investigate the validity and significance of the mid 1990s ice-surface velocities along the surveyed flowlines with respect to current ice dynamics. Furthermore, we aim at elucidating annual flow variability on multiple-days to seasonal timescales. We consider the temperature record of a nearby automatic weather station to investigate a possible relationship between surface melt and flow dynamics.

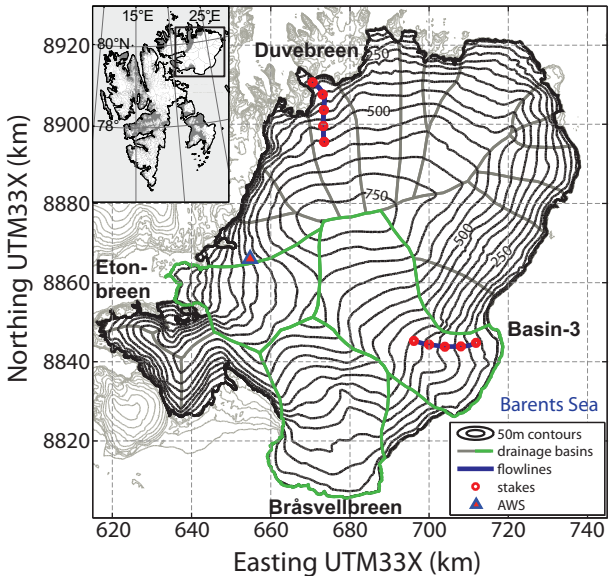

Figure II.1: Surface topography of Austfonna with 50 m elevation contours according to a new DEM by Moholdt and Kääb (A new DEM of the Austfonna ice cap by combining differential SAR interferometry with ICESat laser altimetry. Manuscript submitted for publication.). The black rectangle in the inset indicates the location within the Svalbard archipelago. Drainage basins are outlined in solid grey, in the case of the known surge-type basins in solid green. The survey routes along the central flowlines of Duvebreen and Basin-3 are marked in solid blue, the position of stakes with red dots and the AWS on Etonbreen with a triangle.

II.2 The Austfonna ice cap

Austfonna is a $\sim$8000 km^2 large ice cap centered at 79.7 °N, 24.0 °E on the island Nordaustlandet, in the northeast of Svalbard (Fig. II.1). The ice cap represents the largest ice body on the highly glacierized archipelago. It consists of one main dome that rises to 800 m a.s.l. and where the ice thickness reaches its maximum at about 580 m (Dowdeswell *et al.*, 1986). A main ice divide separates northwestern basins, predominantly terminating on land or in narrow fjords, from southeastern basins, that are to a large extent grounded below sea level and form an almost continuous calving front towards the Barents Sea (Dowdeswell, 1986; Hagen *et al.*, 1993). The general ice-surface velocity pattern derived from InSAR data acquired in January 1994 is typical for a slow moving arctic ice cap. The bulk of the ice is moving at slow velocities $< 10\,\mathrm{m\,a^{-1}}$, interrupted by spatially

limited flow units characterized by enhanced ice surface velocities in the range of about 50–250 m a^{-1} (Dowdeswell *et al.*, 1999). The flow units coincide with subglacial valleys or troughs and model results suggest that the large ice thickness found here, allows for temperate basal conditions, and accordingly, basal motion is the dominant mechanism of ice flow (Dunse *et al.*, 2011). Three basins are known to have surged in the past, specifically Etonbreen, Bråsvellbreen (both during/prior to the 1930s) and Basin-3 (mid 19th century) (Schytt, 1969; Lefauconnier and Hagen, 1991). Currently observed elevation changes with interior thickening at rates of up to 0.5 m a^{-1} and marginal thinning at 1–3 m a^{-1} (Bamber *et al.*, 2004; Moholdt *et al.*, 2010a) can be explained by inefficient glacier dynamics of basins in their quiescent phase (Hagen *et al.*, 2005; Bevan *et al.*, 2007). Geodetically derived mass balance for the time period 2002–2008 suggest a net surface mass balance close to zero with a mean ELA about 450 m a.s.l. for northwestern and 300 m a.s.l. for southeastern basins (Moholdt *et al.*, 2010a). Yet, the net mass balance of Austfonna is clearly negative, $-1.3 \pm 0.5\,\mathrm{km^3\,a^{-1}}$, due to calving and retreat of the marine margin at rates of several tens of meters per year during the past few decades (Dowdeswell *et al.*, 2008).

A major subglacial valley stretches from Wahlenbergfjorden, adjacent to the terminus of Etonbreen, eastwards, and encompasses the basins of Etonbreen and Basin-3. The ice divide of those basins coincides with a peak elevation of the glacier bed >150 m, that drops below sea level on both sides. A geological map of Nordaustlandet published by the Norwegian Polar Institute (NPI) indicates that an E-W line, closely north of the valley, forms a boundary between old and hard lithologies in the north and younger sedimentary successions in the south (Lauritzen and Ohta, 1984). We therefore expect the basal environment beneath Duvebreen being predominantly characterized by a hard bedrock (so long not underlain by marine sediments) and that of Basin-3 by soft sediments. Deformable beds, when thawed and pressurized, significantly expedite basal motion (Tulaczyk *et al.*, 2000). Statistical model results of Svalbard glaciers assign highest surge-probability to polythermal glaciers resting on deformable beds (Hamilton and Dowdeswell, 1996; Jiskoot *et al.*, 2000). Numerical modelling indicates that a frozen bed restricts glacier flow during the quiescent phase until glacier thickening and ice-surface steepening led to basal temperatures at or near the pressure-melting point and high basal shear stress and significant basal motion is initiated (Dunse *et al.*, 2011). Drastic enhancement of basal motion, e.g. through plastic deformation of soft sediments, was a requirement to generate surge-type behaviour.

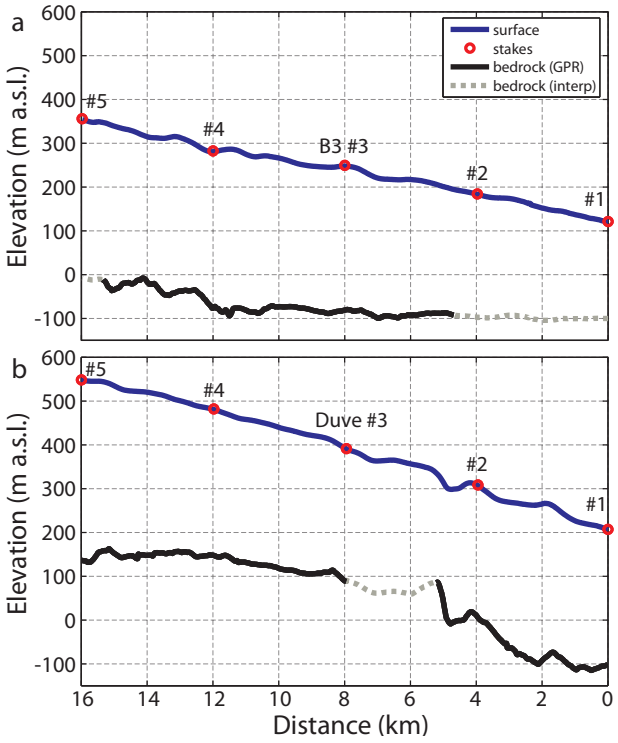

Figure II.2: Glacier geometry along central flowlines of Basin-3 (a) and Duvebreen (b). Surface elevation (solid blue) in m a.s.l. is based on kinematic GPS measurements, GPR-derived ice thickness subtracted to yield bedrock elevation (solid black and dashed grey). Stake positions are marked with red dots.

II.2.1 Basin-3

Historic reports of the first traverse of Austfonna by the Swedish explorer A.E. Nordenskiöld in 1873 and additional evidence from submarine glacial landforms (Solheim, 1986) have led to the conclusion that Basin-3 has surged some years prior to 1873 (Lefauconnier and Hagen, 1991). The observed surface profile is relatively flat (Dowdeswell, 1986). This may be indicative for considerable contribution of basal motion to the overall ice flow or post-surge stagnation and thinning of the receiving area (Meier and Post, 1969). Basin-3 coincides with the eastern half of the major valley that runs west-eastwards across Nordaustlandet and that lies to a large extent below sea level, down to depths of ∼150 m and the terminus calves into the Barents Sea (Dowdeswell, 1986). InSAR analysis

based on SAR scenes acquired in the early 1990s revealed a distinct flow unit of 5–6 km width that snuggles against Isdomen, a prominent subglacial hill to the north (Dowdeswell *et al.*, 1999). Winter velocities in 1992 were as high as 140 m a^{-1}, whereas in 1994, only 80 m a^{-1} were reached. Visible Landsat imagery indicated that the flow unit was fairly inactive between 1973–91 and that fast flow was initiated after 1991. Calculated balance velocities were one order of magnitude smaller than those observed, indicating that the ice flux cannot be sustained under the present climate. Dowdeswell *et al.* (1999) thus interpreted the observed excursion in flow velocities as a short-lived flow instability or mini-surge initiated after 1991.

The observed surface elevation along the flowline of Basin-3 rises from 121 m at B3♯1 (km 0, ca. 5 (/5.3) km from the calving front)) to 356 m at B3♯5 (km 16) with a mean surface slope of 0.84° (Fig. II.2 a). The glacier is grounded below sea level along the entire section. The bedrock is relatively flat between stakes B3♯1–4 (km 0–12), with bedrock elevations ranging from –100 to –70 m a.s.l. Above B3♯4 it rises to near sea level, with bedrock hills at km 12.6 and 14.2. The ice thickness gradually thickens upglacier from 220 m at B3♯1 to 361 m at B3♯5, with a mean of 313 ± 42 m.

II.2.2 Duvebreen

Duvebreen forms a narrow basin in the northwest of Austfonna that drains into the narrow Duvefjord where the terminus forms a ∼2 km wide calving front towering ∼30 m a.s.l. Previously observed velocities range from 20–80 m a^{-1} along the central flowline (Dowdeswell *et al.*, 1999). The surface elevation along the surveyed section of the central flowline ranges from 207 m a.s.l. at Duve♯1, at the lower end, 4–5 km upglacier from the calving front, to 548 m a.s.l. at the higher end (16 km), with a mean surface slope of 1.22° (Fig. II.2 b). The ice thickness is ∼300 m along the lower 10–12 km of the profile and gradually thickens further upglacier to >400 m at Duve♯5. The mean ice thickness is 328 ± 32 m. The bedrock topography is relatively flat in the upper half (8.4–16 km), with elevations ranging from 100–160 m a.s.l. Further downglacier, between 4.8–5.2 km, the bedrock abruptly drops from ∼100 m a.s.l. down to sea level. The bedrock elevation further decreases gradually down to –100 m at 2.1 km and -114 m below (0–1.1 km), with bedrock protrusions of several 100 m in diameter and 20-30 m heights at 4.2 and 1.7 km. These protrusions promote local increase in ice-bed coupling and hence, compressive flow. Convex ice-surface undulations therefore appear slightly upglacier from bedrock protrusions. Vice-versa, concave surface elevations coincide with downglacier sloping bedrock. A very prominent surface depression lies upglacier from the steep bedrock drop between 4.8–5.2 km. Field inspec-

tions in spring 2008 suggest that a supra-glacial lake may form within the depression after the onset of summer melt and drains later in the melt season, once a connection to the englacial/subglacial drainage system is established.

Traditional mass balance measurements from stake height above snow surface/last summer melt surface indicate an unusual low ELA in summer 2008, below the lowermost stakes of both Duvebreen and Basin-3 (Moholdt *et al.*, 2010a). When the units were revisited on August 25, 2008, a continuous snow cover was found down to sea-level. In 2009 the ELA was positioned higher up, but still quite low, about 200 m a.s.l. on both Duvebreen and Basin-3.

II.3 Methods

II.3.1 Continuous Global Positioning System (GPS) observations

We have established a series of stakes along the central flowlines of the two fast-flowing outlets Duvebreen and Basin-3 presented in the previous section and that coincide with

Table II.1: Survey locations of stakes along the central flowlines of Basin-3 (B3 ♯1–5) and Duvebreen (Duve ♯1–5) and their glacier-geometric characteristics. Positions are measured directly and the associated absolute error given in the last raw is constant. Ice thickness and hence, bedrock elevation are indirectly measured, the associated error is ice-thickness depended and provided directly along with a given value.

Stake (no.)	**Latitude** (decim. ° N)	**Longitude** (decim. ° E)	**Surface alt.** (m a.s.l.)	**Ice thickness** (m a.s.l.)	**Bedrock elev.** (m)
B3 ♯1	79.4992370	25.468043	121.18	219.99 ± 13.84*	-98.81 ± 13.94*
B3 ♯2	79.4976114	25.273292	184.21	280.78 ± 14.03*	-96.57 ± 14.13*
B3 ♯3	79.5032166	25.077680	249.41	328.95 ± 2.58	-79.54 ± 2.68
B3 ♯4	79.5136708	24.889501	282.38	357.10 ± 2.66	-74.72 ± 2.76
B3 ♯5	79.5279278	24.710116	355.86	360.94 ± 14.26*	-5.08 ± 14.36*
Duve ♯1	80.1421759	23.958117	207.15	309.00 ± 2.52	-101.854 ± 2.62
Duve ♯2	80.1117554	24.063358	308.36	301.67 ± 2.50	6.685 ± 2.60
Duve ♯3	80.0760756	24.047865	391.36	299.82 ± 2.49	91.541 ± 2.59
Duve ♯4	80.0406765	24.007224	482.06	333.16 ± 2.59	148.897 ± 2.69
Duve ♯5	80.0047962	23.989474	548.42	410.96 ± 2.82	137.461 ± 2.92
Error	±0.05 m	±0.05 m	±0.10 m	* interpolated values (see Sec. II.7)	

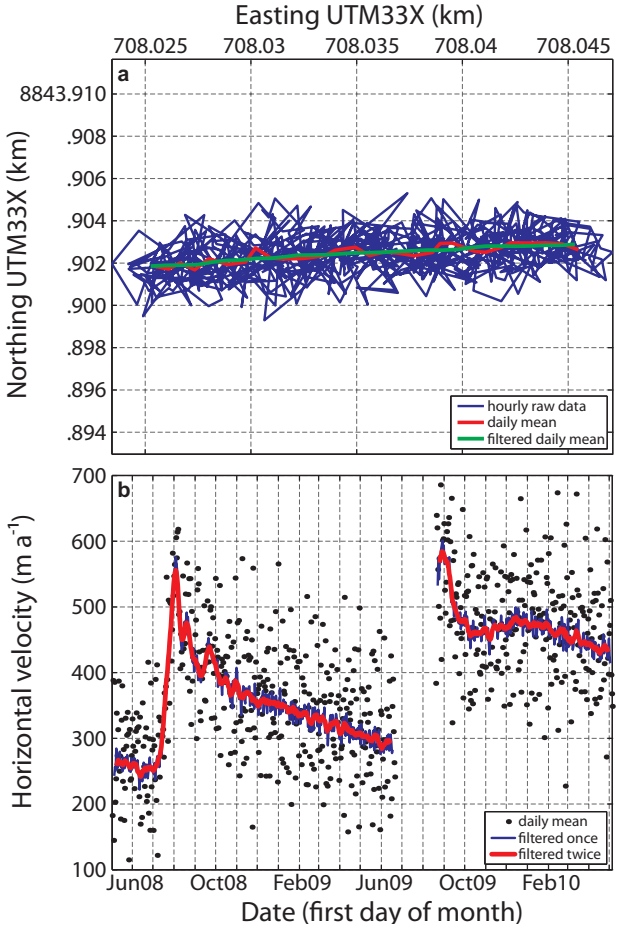

Figure II.3: Processing of continuous GPS observations. Positioning of stake Basin-3 ♯3 during June 2008 (a): hourly GPS raw-data (blue), daily-mean values (red) and after application of an additional 7 day running mean filter (green). Flow velocities derived from displacement of GPS positions (b), utilizing daily mean (black scatters) or 7 day filtered positions with/without additional 7 day filtering of the computed velocities (red/blue solid lines).

profiles earlier investigated by Dowdeswell *et al.* (1999). Each flowline is surveyed at 5 stakes drilled in the glacier ice at 4 km intervals, numbered ♯$1-5$ in upglacier direction II.2. Each stake is equipped with a GPS receiver, deployed in May 2008 with maintenance and data retrieval in early May 2009 and 2010 during the annual ground-based field season. The lower units are positioned in highly crevassed areas with a thin snow cover

in May 2009, and hence weak snow bridges, prohibiting access of all units on Basin-3 (B3 ♯1–5) and the lowermost one on Duvebreen (Duve ♯1). These units were accessed by helicopter in August 2009. Unfortunately, insufficient power-supply caused a gap in the observations between June and August 2009.

We utilize single-frequency GPS receivers that operate unmaintained over time periods of 1 year or longer (van de Wal *et al.*, 2008; den Ouden *et al.*, 2010). The receivers switch on every hour for a period of 3 minutes to allow the system to stabilize. Positions are computed within the receiver and only the geographical position and time is logged. Based on the standard deviation of the average position of a reference station in central Spitsbergen during 2006 − 2009, the horizontal accuracy of the system was determined to be 1.62 m (den Ouden *et al.*, 2010). Post-processing capabilities are restricted by the limited information stored, i.e. we do not apply correction with respect to atmospheric effects such as ionospheric and tropospheric delay, clock information or satellite configuration. Instead, the simple broadcast orbits with the WGS84 reference frame are used and a running average is used to remove high frequency signals at the cost of temporal resolution. Our measurement period largely overlaps with the period investigated by den Ouden *et al.* (2010) and is characterized by a solar ionospheric minimum. A greater error associated with the neglected ionospheric delay and hence, uncertainty in the positioning is to be expected in years with higher solar activity.

The raw data consists of hourly records of the geographical position and the associated date and time. Outliers and data gaps are identified by determining the standard deviations within a moving filter window of 72 hours. An individual dataset entry is disregarded, if it raises the standard deviation of either the latitude or longitude above a specified threshold (e.g. 10 %). Outliers and data gaps may result from loss of energy supply, bad satellite reception, e.g. due to severe riming of the antennas or external disturbances of the satellite signal, such as ionospheric effects. See den Ouden *et al.* (2010) for a more thorough discussion of error sources. Daily displacements in the range of 0.1–1 m are within the uncertainty of the system's position measurements. Thus, data averaging over multiple days is required to yield meaningful results. The cleaned raw data is converted to UTM33X and blocked in 24 hours (hour 0 to hour 2300), yielding a daily mean position (hour 1200). If less than 12 samples of a particular day have passed the quality check, no value is assigned. The daily averages are characterized by significant noise reduction, compared to the hourly raw data (Fig. II.3 a). A 7 day running mean filter is applied independently to the daily Easting and Northing. This further enhances the robustness of the position measurement, however, at the cost of the temporal resolution. Daily dis-

placements and hence velocities are calculated from the averaged positions utilizing the theorem of Pythagoras, neglecting the curvature of the Earth. This is allowed for the small horizontal scales discussed here. Finally, the velocity is smoothed applying once more a 7-day running-mean filter (Fig. II.3 b). den Ouden *et al.* (2010) showed that daily averaging reduces the standard deviation in the position measurement to <0.5 m. The maximum error in the displacement between consecutive days is therefore $1\,\mathrm{m\,d^{-1}}$($365\,\mathrm{m\,a^{-1}}$). The error in displacement between two arbitrary daily mean positions, e.g. at the beginning and end of a 1 year period, remains unaffected and the accuracy increases significantly, i.e. to $1\,\mathrm{m\,a^{-1}}$. Annual velocities according to the mean of the filtered daily velocities are very similar to the annual velocities inferred by this begin-end method, indicating that the filtering of the GPS data provides robust estimates of ice-surface velocities. Annual displacements were also measured independently by dGPS.

II.3.2 Additional data

Low-frequency ground-penetrating radar (GPR) and kinematic Global Navigation Satellite System (GNSS) observations are combined to derive glacier geometry along the flowlines as shown and discussed in Section II.2. Both datasets were collected in spring 2008, while the stakes carrying the continuous GPSs were drilled in. Where GPR measurements are lacking, values are interpolated utilizing additional information from an existing bedrock map at 1 km horizontal resolution (Dunse *et al.*, 2011). A detailed description of the data is provided in the appendix.

The air temperature record from an automatic weather station (AWS; Schuler *et al.*, 2007) was used to derive time series of cumulative positive degree-days (PDD) over the summer months. The station is located in the western part of Austfonna, at 510 m a.s.l. (Fig. II.1). The annual PDD is the sum of daily mean air temperatures above melting over the period of an entire melt season (counted in °C d) and an indicator for surface melt (Reeh, 1989). The temperature record has not been modified to account for the specific location or surface elevation of individual stakes, e.g. by application of a constant temperature lapse rate. Doing so, would have resulted primarily in a shift in the absolute PDD values, but not affected the timing of significant melt periods. In summer 2008, the PDD reached 52 °C d, with maximum diurnal temperatures up to ∼2.5 °C, while in 2009, a PDD was significantly larger, ∼78 °C d and with maximum temperatures reaching ∼3.5 °C in summer.

II.4 Results

The continuous GPS records span the time period from May 2008 to May 2010 and allows for year-to-year intercomparison of ice-surface velocities as well as investigation of seasonal changes, including the summer speed-up of Basin-3 in 2008 and of Duvebreen, in 2008 and 2009.

II.4.1 Ice-surface velocities: 2008/09 vs. 2009/10

At both Basin-3 and Duvebreen, ice-surface velocities decrease with distance upglacier along the central flowline. At Basin-3 during summer 2008, a prominent speed-up oc-

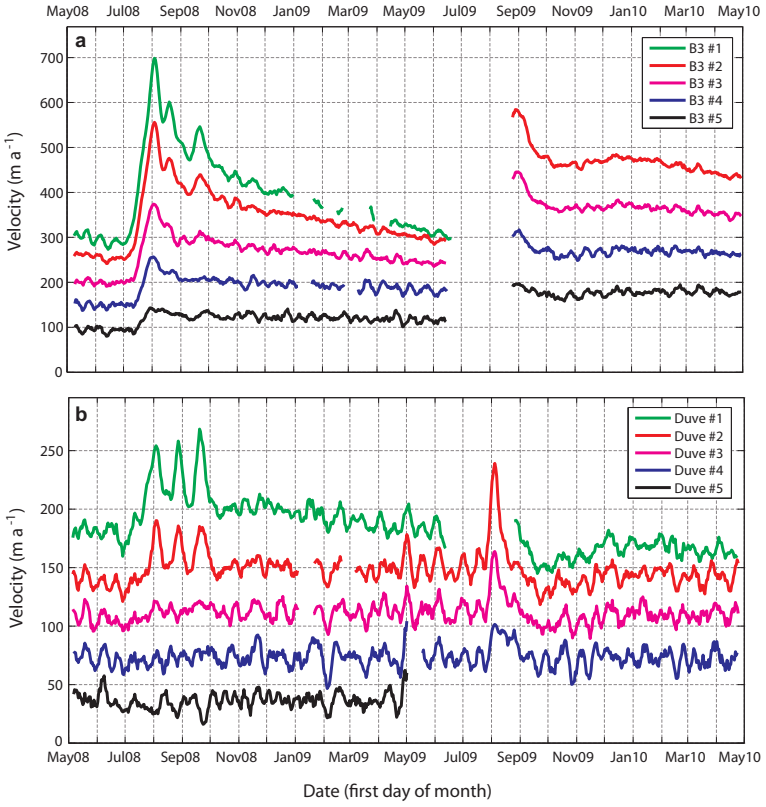

Figure II.4: Flow velocities along the central flowline of Basin-3 (a) and Duvebreen (b), during May 2008–10.

Table II.2: Annual mean velocities for the period May 2008–09 and May 2009–10 based either on all available daily values (V_{mean}) or the first and last day's position at the beginning and end of the respective year (V_{be}). The velocity factor, V_{fac}, refers to current vs. previous year's V_{be}. At Basin-3, data is lacking between ∼15 June–25 August, including both the pre-summer minimum and summer speed-up/maximum. The corresponding entry for V_{mean} is marked by a-superscript.

Stake (no.)	**Period** dd/mm/yyyy	**Flow dir.** (°azimuth)	$\mathbf{V}_{\mathrm{mean}}$ ($\mathrm{m\,a^{-1}}$)	$\mathbf{V}_{\mathrm{be}}$ ($\mathrm{m\,a^{-1}}$)	$\mathbf{V}_{\mathrm{fac}}$
B3 ♯1	04/05/2008–30/04/2009	72.99	415.6 ± 99.4	402.5	–
B3 ♯2	04/05/2008–30/04/2009	87.75	349.4 ± 65.5	348.3	–
B3 ♯3	05/05/2008–30/04/2009	98.47	264.9 ± 39.3	263.9	–
B3 ♯4	05/05/2008–30/04/2009	118.39	190.5 ± 25.5	189.7	–
B3 ♯5	05/05/2008–30/04/2009	119.50	118.1 ± 14.1	117.0	–
B3 ♯1	01/05/2009–23/06/2009	70.76	–	–	–
B3 ♯2	01/05/2009–30/04/2010	86.91	444.1 ± 68.7^{a}	444.4	1.28
B3 ♯3	01/05/2009–30/04/2010	96.56	349.8 ± 48.7^{a}	349.6	1.32
B3 ♯4	01/05/2009–30/04/2010	116.64	256.3 ± 33.8^{a}	255.2	1.34
B3 ♯5	01/05/2009–30/04/2010	118.11	168.2 ± 23.6^{a}	165.3	1.41
Duve ♯1	01/05/2008–30/04/2009	295.50	198.8 ± 19.3	198.1	–
Duve ♯2	01/05/2008–30/04/2009	344.01	150.0 ± 12.5	149.4	–
Duve ♯3	01/05/2008–30/04/2009	357.08	111.1 ± 6.8	110.2	–
Duve ♯4	01/05/2008–30/04/2009	356.29	72.9 ± 7.7	71.6	–
Duve ♯5	01/05/2008–30/04/2009	345.65	35.8 ± 6.9	31.7	–
Duve ♯1	01/05/2009–26/04/2010	296.28	167.7 ± 11.1	174.1	0.88
Duve ♯2	01/05/2009–27/04/2010	341.63	147.2 ± 16.9	146.7	0.98
Duve ♯3	01/05/2009–27/04/2010	357.33	111.5 ± 11.0	110.7	1.00
Duve ♯4	01/05/2009–26/04/2010	355.89	74.1 ± 9.4	73.5	1.03
Duve ♯5	01/05/2009–04/05/2009	360.00	–	–	–

curred at all stations (Fig. II.4). Ice-surface velocities gradually decrease from their maxima in summer 2008 maintaining relatively high speeds during the winter months (compared to V_{JUN}). Apart from the lowermost stake (B3♯1), velocities in June 2009 are above those observed in June 2008. Unfortunately, the summer speed-up in 2009 was not captured, but measured velocities from late summer 2009 until May 2010 appear to be shifted to higher values, compared to the corresponding period of the previous year. Annual mean velocities during May 2008 to May 2009 range from ca. $120\,\mathrm{m\,a^{-1}}$ at B3 ♯5

to 400 m a^{-1} at B3 ♯1 (Tab. II.2). Over the period May 2009–10, velocities have increased by 30–40 %.

At Duvebreen, ice-surface velocities seem to maintain a steady level over the two-year period, with short-lived summer speed-ups most prominent at the lower locations (Fig. II.4). After the summer maximum, velocities return back to pre-summer values, within a few weeks. Annual mean velocities range from 40 m a^{-1} at Duve ♯5 to 200 m a^{-1} at Duve ♯1. In 2009/10, the annual mean velocity appears to have decreased by ca. 10 % at the lowermost stake (Duve ♯1), while velocities at the other measured locations ((Duve ♯2–4)) have not changed significantly.

II.4.2 Summer speed-up 2008 and 2009

Ice-surface velocities at Basin-3 show a clear annual cycle with lowest velocities preceding a prominent summer speed-up (Fig. II.4). At Duvebreen, the summer speed-up is less pronounced, albeit noticeable at the locations further downglacier along the flowline.

Table II.3: Characteristics of the summer speed-up, following the pre-summer minimum in June, V_{JUN}, in terms of the onset date, timing and value of measured maximum velocities, V_{max}, and the normalized maximum flow enhancement relative to pre-summer velocities, V_{fac}.

Stake (no.)	$\mathbf{V}_{\mathrm{JUN}}$ (m a^{-1})	**Onset** (dd/mm/yyyy)	**Summer max.** (dd/mm/yyyy)	$\mathbf{V}_{\mathrm{max}}$ (m a^{-1})	$\mathbf{V}_{\mathrm{fac}}$ ($V_{\mathrm{max}}/V_{\mathrm{JUN}}$)
B3 ♯1	290.6 ± 8.8	09/07/2008	03/08/2008	698.5	2.40
B3 ♯2	253.2 ± 5.6	09/07/2008	03/08/2008	556	2.20
B3 ♯3	198.6 ± 3.7	13/07/2008	02/08/2008	374.1	1.88
B3 ♯4	149.0 ± 4.7	17/07/2008	02/08/2008	256.8	1.72
B3 ♯5	93.3 ± 6.4	20/07/2008	29/07/2008	143.2	1.53
Duve ♯1	178.0 ± 7.4	21/07/2008	03/08/2008	254.2	1.43
Duve ♯2	134.6 ± 6.2	28/07/2008	03/08/2008	190.2	1.41
Duve ♯3	105.0 ± 5.1	01/08/2008	01/08/2008	121.5	1.16
Duve ♯4	71.2 ± 7.6	–	–	–	–
Duve ♯5	37.8 ± 9.0	–	–	–	–
Duve ♯1	180.6 ± 10.2	–	–	–	–
Duve ♯2	150.7 ± 9.4	29/07/2009	04/08/2009	239.1	1.59
Duve ♯3	113.2 ± 8.6	31/07/2009	04/08/2009	163.8	1.45
Duve ♯4	74.8 ± 7.0	01/08/2009	04/08/2009	101.5	1.36
Duve ♯5	–	–	–	–	–

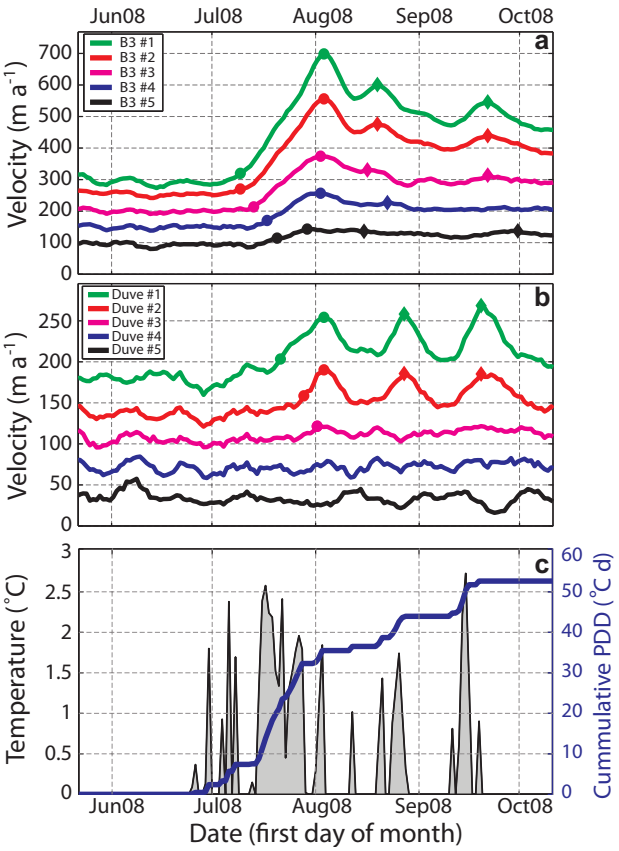

Figure II.5: Summer speed-up along the central flowline of Basin-3 (a) and Duvebreen (b) in summer 2008. Markers indicate the occurrence of the onset of summer speed-up and principle and secondary velocity peaks (see also Tab. II.3). Positive daily mean air temperature and cumulative PDD at the AWS on Etonbreen is shown in (c).

During June, the velocities are characterized by a quasi-stationary pre-summer low and the associated monthly means and standard deviations (of daily values) provide a reference against which to compare maximum summer velocities (Fig. II.5). We define the onset of the summer speed-up at a particular location as the day where velocities are in excess of three standard deviations from the pre-summer mean. The summer speed-up is initiated at the lowest location and occurs with several days delay between stations located further upglacier. The summer maximum, however, is reached at about the same day at all

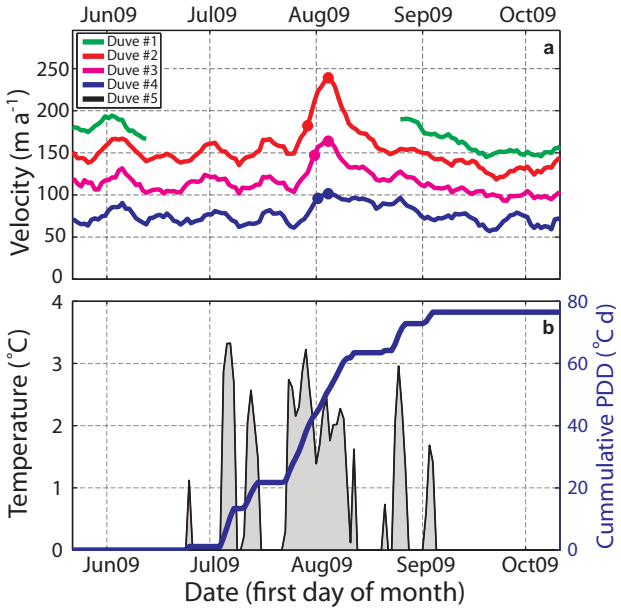

Figure II.6: Summer speed-up along the central flowline of Duvebreen in summer 2009 (a) with markers indicating the occurrence of onset of summer speed-up and peak velocity. Positive daily mean air temperature and cumulative PDD is shown in (b).

locations of a particular flowline (Tab. II.3). At Basin-3, in summer 2008, a summer speed-up was detected at all locations with a onset-delay of 11 days at the highest location (B3 ♯5) compared to the lowermost (B3 ♯1). The maximum summer velocity was reached 9–25 days after the onset date, in the beginning of August (29 July–03 August) and ranges from 143.2 m a^{-1} to 698.5 m a^{-1}, corresponding to an increase of 53–140 % compared to the pre-summer mean, with increasing acceleration downglacier.

Where a summer speed-up is noticeable, the ice-surface velocity record from summer 2008 is characterized by 3 distinct peaks, concurrent at all locations. The second and third peaks follow ca. 2 and 7 weeks after the primary summer maxima. (Fig. II.5 a,b). The initial summer speed-up coincides with the first prolonged period with air temperatures above 0 °C in the second half of July (Fig. II.5 c). The two other velocity peaks coincide with a second and third period of melting that lead to a significant rise in cumulative PDD. In 2009, summer velocities are only available from 3 locations of Duvebreen (Duve ♯2–4). The summer speed-up at these locations is of higher amplitude (Tab. II.3) and also

detected further upglacier than in 2008, where only the two lowermost stakes showed significant acceleration (Duve ♯1–2).

II.5 Discussion

II.5.1 Surface-velocities fluctuations

The distinct characteristics of the summer-speed up in 2008 and 2009 can be explained by the total volume of surface-generated meltwater and the timing of the input into the subglacial drainage system. Summer 2008 was characterized by relatively low air temperatures, yielding a low cumulative PDD and hence, little surface melt. Snow cover persisted over the ice cap during the entire summer season and is likely to have reduced surface melt through increasing the surface albedo. The input of small volumes of melt water to the subglacial system may not have been sufficient to establish an effective drainage system. Consequently, renewed melt water input during late-summer melt periods, associated with a distinct increase in cumulative PDD, presumably provoke rising subglacial water pressure and enhanced hydraulic lubrication. In 2009, air temperatures were significantly higher, yielding a cumulative PDD of 78 °C d, compared to only 52 °C d in 2008. The summer speed-up in 2009 coincides with a strong increase in cumulative PDD. A second significant melt period in the end of August has no clear effect on the observed surface motion, in contrast to comparable melt periods in 2008. This indicates that in 2009, the basal drainage system is capable to accommodate the increased input of meltwater likely associated with the warm events, without weakening the ice-bed coupling. This in turn implies that a hydraulically efficient drainage system has probably evolved earlier in summer during the principle melt period (late July to early August). At both flowlines an upglacier propagation of the onset of the summer speed-up was observed. This can be explained by a later onset of surface melt and hence local input of meltwater into the englacial/subglacial drainage system. Alternatively, longitudinal coupling may take place, with increased delay in the response of upglacier ice regions to a speed-up initiated further downglacier.

At Basin-3, the decrease from the summer-2008 velocity peak is slow and gradual. This indicates that basal water pressure is maintained over a long time period. An inefficient drainage system may have retained a significant fraction of basal water throughout the winter months, thereby facilitating continuous though diminishing basal lubrication or plastic deformation of water-saturated, pressurized sediments. The bedrock along the

surveyed profile is gentle and lies below sea level along its entire length and provides little topographic resistance to basal motion. The fast-flow unit is confined to the north by a distinct bedrock protrusion, but is otherwise embedded within slow moving/stagnat ice, from which it is separated by distinct lateral shear margins. Furthermore, a smooth bedrock profile and likely presence of soft sediments permit for unopposed longitudinal coupling to dynamic process initiated at the ice margin. This may explain why the summer speed-up is noticeable at all locations, albeit at decreasing amplitude further upglacier. The observed acceleration of Basin-3 in 2009/10 compared to 2008/09 could be explained by a general shift of the basal water pressure towards higher values, but this remains speculative, as no information of basal hydrology is available.

At Duvebreen, the multiple summer speed-ups in 2008 and the single one in 2009 are short-lived in nature. The surface velocity quickly returns to pre-summer values. This may be explained by a rapid transition from a hydraulically inefficient, distributed drainage system to a hydraulically efficient, channelized system. Also a channelized system, if abruptly overcharged, may weaken ice-bed coupling by reducing the effective normal pressure (Schoof, 2010a). Another explanation is provided by the specific topography, which is fundamentally different than those for Basin-3. At the uppermost 3 stakes on Duvebreen (Duve ♯3–5) the glacier is grounded about 100 m a.s.l. (Fig. II.2). Duve ♯2 is located just downglacier of a steep drop into the narrow Duvefjord, where bedrock elevations reach deeper than –100 m a.s.l. (Duve ♯1). The steep valley walls may possess significant lateral drag upon the lower section of the glacier, i.e. below Duve ♯2. Additional basal lubrication has to compensate for the lateral drag. This may only be fulfilled in periods where the basal water pressure exceeds a certain threshold. Lateral shear may thus stabilize the terminus of Duvebreen and make the glacier less prone to terminus fluctuations and/or longitudinal coupling of changes in terminus dynamics, initiated at the calving front. The steep bedrock topography at Duve ♯2 promotes the formation of surface crevasses (those have also been observed in the field) and facilitates meltwater routing to the bed. The presence of soft sediments and a reduction in effective normal pressure may alternatively explain the sensitivity of the marine grounded section to flow perturbations as also suggested by recent model experiments (Dunse *et al.*, 2011). In 2009, surface melt and input of meltwater into the englacial/subglacial drainage system may have occurred at higher elevation, causing noticeable summer speed-up also at higher stations.

II.5.2 Implications on ice flux/discharge

Dowdeswell *et al.* (1999) investigated the ice flux of Basin-3 across a ca. 5 km×240 m cross section ∼7.5 km upglacier from the marine ice margin. Assuming a depth-averaged velocity of 85 % of the measured surface velocity (90 m a^{-1} in winter 1992, 50 m a^{-1} in winter 1994), the figure was to 0.1 (0.05) km^3 a^{-1}in 1992 (1994). A more recent calving estimate of Basin-3 of 0.15 km^3 a^{-1} (Dowdeswell *et al.*, 2008), includes marginal retreat in addition to the estimated ice-flux towards the calving front. Given the three-fold velocity increase presented in the present study (annual mean of $400 - 450$ m a^{-1}) and the assumption of an unchanged fluxgate area, the ice discharge of Basin-3 into the Barents Sea presumably increased significantly. Even without further retreat of the marine ice margin, the figure is about 0.3 km^3 a^{-1}. The flow velocities of the terminus of Duvebreen are very similar to those by Dowdeswell *et al.* (2008), drastic changes in terminus position are not observed and thus the ice discharge is unlikely to have changed significantly.

II.6 Conclusions

Duvebreen flows at similar velocities as in the 1990s and the spatial velocity pattern and the characteristics of summer speed-up appear to be controlled by the distinct topography with the lower part of the glacier flowing over an escarpment and being channeled into a deep and narrow fjord. Basin-3 has accelerated by about factor three compared to the 1990s and showed also an acceleration of 30–40 % from 2008/09 to 2009/10. Velocities measured during summer 2008 reach up to 2 m d^{-1} (700 m a^{-1}) within 5 km from the calving front and are as high as those reported from Kronebreen, often referred to as the fastest tidewater glacier on Svalbard, with annual mean velocities up to 1.5 m d^{-1} (550 m a^{-1}) (Lefauconnier *et al.*, 1994) and recent summer maxima of 2.5 m d^{-1} measured at the calving front (Rolstad *et al.*, 2009).

In 2008, the observed summer speed-up of both Basin-3 and Duvebreen appears closely linked to positive diurnal air temperatures/cumulative PDD, a proxy for surface melt and potential input of meltwater into the englacial/subglacial drainage system. In 2009, GPS observations only cover the speed-up of Duvebreen. Summer 2009 was significantly warmer than summer 2008 with a pronounced principle melt period (late July to early August) and the relationship between ice-surface velocity and air temperature is more complex. Meltwater volumes produced later in the melt season do not lead to positive excursions in glacier flow. This indicates that a hydraulically effective drainage system has established in the course of the principle melt period and increased meltwater input

can therefore be accommodated without raising basal water pressure and enhancing basal lubrication.

II.7 Appendix: derivation of glacier geometry along flowlines

To derive the glacier geometry along the flowlines, we combine surface elevation profiles from ground-based kinematic Global Navigation Satellite System (GNSS; GPS and GLONASS) with low-frequency ground penetrating radar (GPR) measurements of ice thickness. Kinematic GNSS observations were logged at a rate of 1 Hz (approx. every 5.5 m) and differentially post-processed using a stationary GNSS as reference, yielding an accuracy of typically better than 5 cm in horizontal position and 10 cm in height (Eiken *et al.*, 1997). GPR (VIRL-6) measurements were triggered every 2 m by means of an odometer. Navigation data was recorded simultaneously with the GPR data using a GPS Garmin II Plus receiver (Vasilenko *et al.*, 2010). The radar transmitter generates pulses of 25 ns duration with a center frequency of 20 MHz, resulting in a system resolution of approximately 2 m (assuming a radio-wave velocity of $0.168 \pm 0.0005\,\mathrm{m\,ns^{-1}}$, typical for cold ice). The precision of the ice thickness measurements was estimated to $\sim$1.6 m, based on the standard deviation in ice thickness at more than 34000 crossover points from the entire Austfonna survey (personal communication G. Moholdt, Department of Geosciences, University of Oslo, Oslo, Norway, 2011). The precision represents the error in ice thickness due to the uncertainty in the time measurement (digitization of bedrock reflection). The accuracy in ice thickness is determined when adding an absolute error of about 0.3 % (3 mm per meter ice) to the precision value. This absolute error is related to the uncertainty of radio-wave velocity. For an ice thickness of 350 m this corresponds to an error of about 1 m ($2000\,\mathrm{ns} \times 0.0005\,\mathrm{m\,ns^{-1}}$) yielding an accuracy of the GPR-derived ice thickness of about 2.6 m.

To link kinematic GPS and GPR measurements along the flowline, linear legs between consecutive stake positions have been taken as benchmark distance. A correction factor, specific for each dataset and leg (typically between 0.98 and 1) is then applied to all distance increments so that the cumulative distance along the measured tracks matches the benchmark distance. Both datasets are resampled at 10 m intervals to allow subtraction of ice thickness from surface elevation to derive bedrock elevation. Gaps in the GPR record are padded by extracting values from an ice thickness map at 1 km horizontal resolution (Dunse *et al.*, 2011). Values were extracted for positions corresponding to 1 km intervals

along the flowlines and corrected for a mean bias, determined from the overlapping sections (mean and standard deviation of -16.61 ± 11.59 m in the case of Basin-3; -1.11 ± 7.80 m in the case of Duvebreen).

Acknowledgements

This study is a contribution to the International Polar Year project GLACIODYN funded by the Norwegian Research Council (grant 176076/S30). The final stage was supported by funding to the ice2sea project from the European Union 7th Framework Programme, grant number 226375, ice2sea contribution number 029. T. Dunse was supported by an Arctic field grant through the Svalbard Science Forum (field work). We thank G. Moholdt and M. Sund for assistance in retreiving the GPS data. E. Vasilenko and F. Navarro are greatly acknowledged for collecting low-frequency GPR data along the flowlines and extracting bedrock information.

References

Bamber, J., Krabill, W., Raper, V., and Dowdeswell, J., 2004. Anamolous recent growth of part of a large Arctic ice cap: Austfonna, Svalbard. Geophysical Research Letters, 31(12), L12402.

Bevan, S., Luckman, A., and Murray, T., 2007. Positive mass balance during the late 20th century on Austfonna, Svalbard revealed using satellite interferometry. Annals of Glaciology, 46, 117–122.

Clarke, G., 1976. Thermal regulation of glacier surging. Journal of Glaciology, 16(74), 231–250.

Clarke, G., 1987. Fast glacier flow - ice streams, surging, and tidewater glaciers. Journal of Geophysical Research-Solid Earth and Planets, 92(B9), 8835–8841.

Clarke, G., Collins, S., and Thompson, D., 1984. Flow, thermal structure, and subglacial conditions of a surge-type glacier. Canadian Journal of Earth Sciences, 21(2), 232–240.

Copland, L., Sharp, M. J., and Nienow, P. W., 2003. Links between short-term velocity variations and the subglacial hydrology of a predominantly cold polythermal glacier. Journal of Glaciology, 49(166), 337–348.

den Ouden, M., Reijmer, C., Pohjola, V., van de Wal, R., Oerlemans, J., and Boot, W., 2010. Stand-alone single-frequency GPS ice velocity observations on Nordenskiöldbreen, Svalbard. The Cryosphere, 4(4), 593–604.

Dowdeswell, J., 1986. Drainage-basin characteristics of Nordaustlandet ice caps, Svalbard. Journal of Glaciology, 32(110), 31–38.

Dowdeswell, J., Drewry, D., Cooper, A., Gorman, M., Liestøl, O., and Orheim, O., 1986. Digital mapping of the Nordaustlandet ice caps from airborne geophysical investigations. Annals of Glaciology, 8, 51–58.

Dowdeswell, J. A., Benham, T. J., Strozzi, T., and Hagen, J. O., 2008. Iceberg calving flux and mass balance of the Austfonna ice cap on Nordaustlandet, Svalbard. Journal of Geophysical Research-Earth Surface, 113(F3), F03022.

Dowdeswell, J. A., Unwin, B., Nuttall, A. M., and Wingham, D. J., 1999. Velocity structure, flow instability and mass flux on a large Arctic ice cap from satellite radar interferometry. Earth and Planetary Science Letters, 167(3-4), 131–140.

Dunse, T., Greve, R., Schuler, T., and Hagen, J., 2011. Permanent fast flow vs. cyclic surge behavior: numerical simulations of the Austfonna ice cap, Svalbard. Journal of Glaciology, 57(202), 13 pp.

Eiken, T., Hagen, J. O., and Melvold, K., 1997. Kinematic GPS survey of geometry changes on Svalbard glaciers. Annals of Glaciology, Vol 24, 1997, 24, 157–163.

Fountain, A. G. and Walder, J. S., 1998. Water flow through temperate glaciers. Reviews of Geophysics, 36(3), 299–328.

Hagen, J., Eiken, T., Kohler, J., and Melvold, K., 2005. Geometry changes on Svalbard glaciers: mass-balance or dynamic response? Annals of Glaciology, 42, 255–261.

Hagen, J., Liestøl, O., Roland, E., and Jørgensen, T., 1993. Glacier Atlas of Svalbard and Jan Mayen. Norsk Polarinstitutt, Oslo, Norway.

Hamilton, G. S. and Dowdeswell, J. A., 1996. Controls on glacier surging in Svalbard. Journal of Glaciology, 42(140), 157–168.

Iken, A. and Bindschadler, R. A., 1986. Combined Measurements of Subglacial Water-pressure and Surface Velocity of Findelengletscher, Switzerland - Conclusions About Drainage System and Sliding Mechanism. Journal of Glaciology, 32(110), 101–119.

Iken, A., Röthlisberger, H., Flotron, A., and Haerberli, W., 1983. The Uplift of Unteraargletscher At the Beginning of the Melt Season - A Consequence of Water Storage At the Bed. Journal of Glaciology, 29(101), 28–47.

Jiskoot, H., Murray, T., and Boyle, P., 2000. Controls on the distribution of surge-type glaciers in Svalbard. Journal of Glaciology, 46(154), 412–422.

Lauritzen, Ø. and Ohta, Y., 1984. Geological map of Svalbard, 1:500 000, Sheet 4G, Nordaustlandet. Norsk Polarinstitutt, Skrifter, 154 D, 14pp., 1 map.

Lefauconnier, B. and Hagen, J., 1991. Surging and Calving Glaciers in Eastern Svalbard. Norsk Polarinstitutt, Oslo, Norway.

Lefauconnier, B., Hagen, J., and Rudant, J., 1994. Flow Speed and Calving Rate of Kongsbreen Glacier, Svalbard, Using Spot Images. Polar Research, 13(1), 59–65.

Mair, D., Nienow, P., Willis, I., and Sharp, M., 2001. Spatial patterns of glacier motion during a high-velocity event: Haut Glacier d'Arolla, Switzerland. Journal of Glaciology, 47(156), 9–20.

Meier, M. and Post, A., 1969. What are glacier surges. Canadian Journal of Earth Sciences, 6(4P2), 807–817.

Meier, M. and Post, A., 1987. Fast tidewater glaciers. Journal of Geophysical Research-Solid Earth and Planets, 92(B9), 9051–9058.

Moholdt, G., Hagen, J., Eiken, T., and Schuler, T., 2010. Geometric changes and mass balance of the Austfonna ice cap, Svalbard. The Cryosphere, 4(1), 21–34.

Murray, T., Stuart, G., Miller, P., Woodward, J., Smith, A., Porter, P., and Jiskoot, H., 2000. Glacier surge propagation by thermal evolution at the bed. Journal of Geophysical Research-Solid Earth, 105(B6), 13491–13507.

Nick, F., Vieli, A., Howat, I., and Joughin, I., 2009. Large-scale changes in Greenland outlet glacier dynamics triggered at the terminus. Nature Geoscience, 2(2), 110–114.

Nuttall, A. M. and Hodgkins, R., 2005. Temporal variations in flow velocity at Finsterwalderbreen, a Svalbard surge-type glacier. Annals of Glaciology, Vol 42, 2005, 42, 71–76.

O'Neel, S., Echelmeyer, K. A., and Motyka, R., 2003. Short-term variations in calving of a tidewater glacier: LeConte Glacier, Alaska, USA. Journal of Glaciology, 49(167), 587–598.

Pfeffer, W. T., Harper, J. T., and O'Neel, S., 2008. Kinematic constraints on glacier contributions to 21st-century sea-level rise. Science, 321(5894), 1340–1343.

Pinglot, J., Hagen, J., Melvold, K., Eiken, T., and Vincent, C., 2001. A mean net accumulation pattern derived from radioactive layers and radar soundings on Austfonna, Nordaustlandet, Svalbard. Journal of Glaciology, 47(159), 555–566.

Price, S. F., Payne, A. J., Catania, G. A., and Neumann, T. A., 2008. Seasonal acceleration of inland ice via longitudinal coupling to marginal ice. Journal of Glaciology, 54(185), 213–219.

Reeh, N., 1989. Parameterization of melt rate and surface temperature on the Greenland ice sheet. Polarforschung, 59(3), 113–128.

Rippin, D. M., Willis, I. C., Arnold, N. S., Hodson, A. J., and Brinkhaus, M., 2005. Spatial and temporal variations in surface velocity and basal drag across the tongue of the polythermal glacier midre Lovenbreen, Svalbard. Journal of Glaciology, 51(175), 588–600.

Rolstad, C., Chapuis, A., and Norland, R., 2009. Electromagnetic interference in ground-based interferometric radar data from Kronebreen (Svalbard) calving front due to multipath scattering and tidal cycles. Journal of Glaciology, 55(193), 943–945.

Röthlisberger, H., 1972. Water pressure in intra- and subglacial channels. Journal of Glaciology, 11(62), 177–203.

Rott, H., 2009. Advances in interferometric synthetic aperture radar (InSAR) in earth system science. Progress In Physical Geography, 33(6), 769–791.

Schoof, C., 2010a. GLACIOLOGY Beneath a floating ice shelf. Nature Geoscience, 3(7), 450–451.

Schoof, C., 2010b. Ice-sheet acceleration driven by melt supply variability. Nature, 468(7325), 803–806.

Schuler, T., Loe, E., Taurisano, A., Eiken, T., Hagen, J., and Kohler, J., 2007. Calibrating a surface mass-balance model for Austfonna ice cap, Svalbard. Annals of Glaciology, 46, 241–248.

Schytt, V., 1969. Some comments on glacier surges In eastern Svalbard. Canadian Journal of Earth Sciences, 6(4P2), 867–871.

Solheim, A., 1986. Submarine evidence of glacier surges. Polar Research, 4, 91–95.

Solomon, S., Qin, D., Manning, M., Chen, Z., Marquis, M., Averyt, K., Tignor, M., and Miller, H.L. (eds.), 2007. Climate Change 2007: The Physical Science Basis. Contribution of Working Group I to the Fourth Assessment Report of the Intergovernmental

Panel on Climate Change. Cambridge University Press, Cambridge, United Kingdom and New York, NY, USA.

Strozzi, T., Luckman, A., Murray, T., Wegmuller, U., and Werner, C. L., 2002. Glacier motion estimation using SAR offset-tracking procedures. Ieee Transactions On Geoscience and Remote Sensing, 40(11), 2384–2391.

Sundal, A. V., Shepherd, A., Nienow, P., Hanna, E., Palmer, S., and Huybrechts, P., 2011. Melt-induced speed-up of Greenland ice sheet offset by efficient subglacial drainage. Nature, 469(7331), 522–U83.

Thomas, R. H., 2004. Force-perturbation analysis of recent thinning and acceleration of Jakobshavn Isbræ, Greenland. Journal of Glaciology, 50(168), 57–66.

Tulaczyk, S., Kamb, W. B., and Engelhardt, H. F., 2000a. Basal mechanics of Ice Stream B, West Antarctica 1. Till mechanics. Journal of Geophysical Research-Solid Earth, 105(B1), 463–481.

Tulaczyk, S., Kamb, W. B., and Engelhardt, H. F., 2000b. Basal mechanics of Ice Stream B, West Antarctica 2. Undrained plastic bed model. Journal of Geophysical Research-Solid Earth, 105(B1), 483–494.

van de Wal, R. S. W., Boot, W., van den Broeke, M. R., Smeets, C. J. P. P., Reijmer, C. H., Donker, J. J. A., and Oerlemans, J., 2008. Large and rapid melt-induced velocity changes in the ablation zone of the Greenland Ice Sheet. Science, 321(5885), 111–113.

Vasilenko, E., Navarro, F., Dunse, T., Eiken, T., and Hagen, J., 2010. New low-frequency radio-echo soundings of Austfonna ice cap, Svalbard. In: Ahlstrøm, A. and Sharp, M. (Eds.), The Dynamics and Mass Budget of Arctic Glaciers. Extended abstracts. Workshop and GLACIODYN (IPY) meeting, 16−19 February 2009, Kananaskis, Canada., volume 127 of Danmarks og Grønlands geologiske undersøkelse rapport. GEUS, Copenhagen: IASC Working Group on Arctic Glaciology.

Walder, J. S., 1986. Hydraulics of Subglacial Cavities. Journal of Glaciology, 32(112), 439–445.

Zwally, H. J., Abdalati, W., Herring, T., Larson, K., Saba, J., and Steffen, K., 2002. Surface melt-induced acceleration of Greenland ice-sheet flow. Science, 297(5579), 218–222.

III

Permanent fast flow vs. cyclic surge behaviour: numerical simulations of the Austfonna ice cap, Svalbard[†]

Thorben DUNSE,[1] Ralf GREVE,[2] Thomas Vikhamar SCHULER,[1] Jon Ove HAGEN,[1]

[1]*Department of Geosciences, University of Oslo, PO Box 1047, Blindern, NO-0316 Oslo, Norway*

E-mail: thorben.dunse@geo.uio.no

[2]*Institute of Low Temperature Science, Hokkaido University, Sapporo 060-0819, Japan*

ABSTRACT. A large part of the ice flux within ice caps occurs through spatially limited fast flowing units. Some of them permanently maintain fast flow, whereas others operate in an oscillatory mode, characterized by short-lived active phases followed by long quiescent phases. This surge-type behaviour results from intrinsic rather than external factors, thus complicating estimates of glacier response to climate change. Here, we present numerical model results from Austfonna, an ice cap on Svalbard that comprises several surge-type basins. Previous studies have suggested a thermally controlled soft-bed surge mechanism for Svalbard. We systematically change the parameters that govern the nature of basal motion and thereby control the transition between permanent and oscillatory fast flow. Surge-type behaviour is realized by a relatively abrupt onset of basal sliding when basal temperatures approach the pressure-melting point and enhanced sliding of marine grounded ice. Irrespective of the dynamic regime, the absence of considerable volumes of temperate ice, both in the observed and simulated ice cap, indicates that fast flow is accomplished by basal motion over a temperate bed. Given an idealized present-day climate, the equilibrium ice cap size varies significantly, depending on the chosen parameters.

[†] Journal of Glaciology, 57(202), 13 pp., 2011.

III.1 Introduction

The role of glaciers as indicators of climate change and their major contribution to sea level rise is widely acknowledged. However, extraction of climate signals from glaciers is not straightforward, because the history, current state and future evolution of glaciers result from the interplay of external factors, e.g. changes in surface air temperature or precipitation, and also intrinsic glacier dynamics (Hagen *et al.*, 2005; Yde and Paasche, 2010). Surge-type glaciers illustrate this affinity in a drastic way. Periodically, they experience significant changes in glacier dynamics and geometry that are largely decoupled from climate variability, challenging both observational glaciologists and modellers to deliver estimates about their response to climate change. This is especially true for predictions on decadal timescales, in great demand by the public in general and decision makers in particular.

Surface velocities of the order of several $100-1000\,\mathrm{m\,a^{-1}}$ are typical for glaciers during the surge phase. Such high flow velocities are achieved through basal motion (Clarke, 1987) and require a temperate glacier bed, i.e. basal temperatures at the pressure-melting point (PMP). For a frozen bed, ice deformation is the exclusive mode of glacier motion, typically yielding moderate surface velocities of the order of $1-10\,\mathrm{m\,a^{-1}}$, depending on shear stress and ice temperature. If conditions for basal motion are maintained, the dynamics of a glacier may be characterized by permanent fast flow, such as observed for ice streams, otherwise a temporal pattern of alternating fast and slow glacier flow may evolve. These different dynamic regimes have an impact on the glacier's net mass balance. Surge-type glaciers are characterized by an oscillatory mode of equilibrium and do not maintain a steady mass flux that equals the theoretical balance flux to maintain a steady-state surface profile (Clarke, 1987). Instead, their dynamics are characterized by a long quiescent phase of inefficient ice flow, undershooting the balance flux, and a short-lived surge phase of super-efficient ice flow, greatly overshooting the balance flux. During the quiescent phase, the glacier can be divided into an active thickening zone, the 'reservoir zone', and an almost stagnant depleted zone, the 'receiving zone', separated by the dynamic balance line (DBL) (Meier and Post, 1969; Dolgoushin and Osipova, 1975). The reservoir and receiving zones do not usually coincide with the glacier's accumulation and ablation zones, which are separated by the equilibrium line altitude (ELA), instead the DBL marks a boundary zone where glacier outflow is restricted (Clarke *et al.*, 1984). The distribution of mass from the reservoir zone into a receiving zone during the surge may be accompanied by a significant advance of the terminus (Meier and Post, 1969).

Observations on Variegated Glacier in Alaska suggest that 95 % of the motion during the surge in 1982–83 was due to basal sliding and only ∼5 % due to internal deformation (Kamb *et al.*, 1985). Basal processes are therefore considered fundamental in initiating and maintaining glacier surges. Factors determining the absolute contribution of basal motion to the overall ice flow include the thermal regime at the glacier base, basal shear stress, basal water pressure and the lithology of the underlying bedrock, as well as the presence of deformable sediments. Kamb (1987) and Raymond (1987) discussed implications of different basal hydraulic-drainage systems and pointed out that a highly pressurized system of linked cavities may facilitate fast flow and prevail during a surge, while a switch to a hydrologically efficient channel system reduces the basal water pressure and may cause surge termination. Clarke *et al.* (1984) suggested the presence of highly-deformable, water-saturated sediments as an alternative explanation of highly enhanced basal motion. Basal motion of polythermal ice bodies is spatially and temporarily restricted to basal areas at PMP. The cold basal areas are frozen to the ground and basal motion is negligible on timescales ≪100 ka (Shreve, 1984). Therefore, the thermal evolution of the bed plays a decisive role (Clarke, 1976).

The occurrence of surge-type glaciers worldwide is spatially limited to several clusters, suggesting that certain regional conditions favour surge behaviour (Meier and Post, 1969; Dolgoushin and Osipova, 1975). One such cluster is found on Svalbard, a highly glacierized archipelago in the Eurasian Arctic (Fig. III.1). Statistical model results indicate a thermally controlled soft-bed surge mechanism with largest surge probability for long polythermal glaciers resting on unlithified or easily erodible beds (Hamilton and Dowdeswell, 1996; Jiskoot *et al.*, 2000). The sparse observations on glacier surges that are available conform with these theoretical results. Murray *et al.* (2000) found that the advance of the surge front of Bakaninbreen, a 17 km long surge-type glacier in southern Svalbard, has been associated with the down-glacier expansion of a temperate ice base. Furthermore, they found evidence for subglacial sediments within the area affected by the surge. Observations of soft beds underlying polythermal surge-type glaciers are also available from other areas of Svalbard (e.g. Glasser and Hambrey, 2001).

Large-scale surge behaviour bears the potential for abrupt ice sheet disintegration. Ice-rafted debris found in marine sediment cores from the North Atlantic provide a record of exceptional iceberg-calving events. These events, known as 'Heinrich events', occurred at time intervals of ∼7 ka and have been proposed to be associated with periodic surges ('binge-purge oscillations') of the prehistoric Laurentide Ice Sheet (MacAyeal, 1993) that covered large parts of North America between ∼95 and 20 ka BP. Oscillatory ice sheet

behaviour similar to Heinrich events has been generated with a number of models for simplified set-ups (MacAyeal, 1993; Payne, 1995; Hindmarsh and Le Meur, 2001; Calov *et al.*, 2002, 2010; Greve *et al.*, 2006). Calov *et al.* (2010) compare nine thermomechanical ice-sheet models, one model utilizing a combination of the shallow-shelf (SSA) and shallow-ice approximation (SIA), the others being purely SIA type, and showed that seven models including the SSA/SIA model, are capable of producing oscillatory behaviour. The oscillations were characterized either by single- or multi-peaked spectra, however differences in periodicity are large. Although a discrete switch from no-slip conditions to full basal sliding is not required for the occurrence of oscillations (Calov *et al.*, 2010), the smoothing of the transition over a broad subfreezing-temperature range may prohibit oscillatory behaviour (Greve *et al.*, 2006). The amplitude of the oscillations increased with increased enhancement of basal sliding (Calov *et al.*, 2010). Furthermore, the influence of changed climate conditions was tested. No clear relationship between oscillatory behaviour and air temperature was found, but an increase in accumulation, leading to an increased ice thickness, forced some of the models from an oscillatory mode to a mode of steady fast flow. For the remaining models that exhibited oscillatory behaviour, the period of the oscillations decreased, associated with a decrease in time required for the build up of a critical ice thickness in the reservoir zone at which the surge is released (Calov *et al.*, 2010).

Here we present numerical simulations of Austfonna, a large polythermal ice cap in Svalbard (Fig. III.1). Several of the drainage basins of this ice cap are known to have surged in the past. The aim is to generate an ice cap that is similar in size and dynamic behaviour to present-day Austfonna and that provides suitable initial conditions for prognostic model runs in future studies. We investigate a number of model parameters that exert controls on the nature of the dynamics of the simulated ice cap. In light of the suggested surge mechanism for Svalbard, we focus, in particular, on the description of basal sliding and the role of the basal thermal regime.

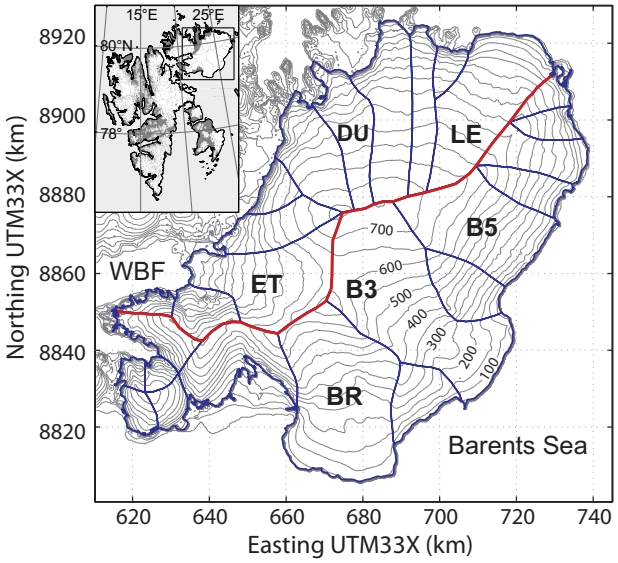

Figure III.1: Map of the Austfonna ice cap and its location within the Svalbard archipelago (inset). Contours show surface elevations (m a.s.l.) blue solid lines indicate drainage basins and the red solid line the main ice divide. Basins of interest are marked with bold letters: the three known surge-type basins Etonbreen (ET), terminating into Wahlenbergfjorden (WBF) and Bråsvellbreen (BR) and Basin-3 (B3), terminating into the Barents Sea. Other basins of interest are Duvebreen (DU), Leighbreen (LE) and Basin-5 (B5).

III.2 The Austfonna ice cap

Austfonna (the Norwegian name means 'eastern ice cap'), is located on the island Nordaustlandet, at 80° N, in the northeast of Svalbard (Fig. III.1). Covering an area of >8000 km^2 it is by far the largest individual ice body on the highly glacierized archipelago.

III.2.1 Ice cap geometry and geometric changes

Surface elevation and ice thickness, and thereby bed topography, were extensively mapped by airborne radio-echo sounding (RES) in 1983 (Dowdeswell *et al.*, 1986). Austfonna consists of a main central dome merging with a somewhat smaller dome to its south that together feed a number of drainage basins (Figs. III.1 and III.2a). A main ice divide oriented southwest/northeast forms a natural border between the northwestern basins, predominately terminating on land or in fjords, and the southeastern basins that are to

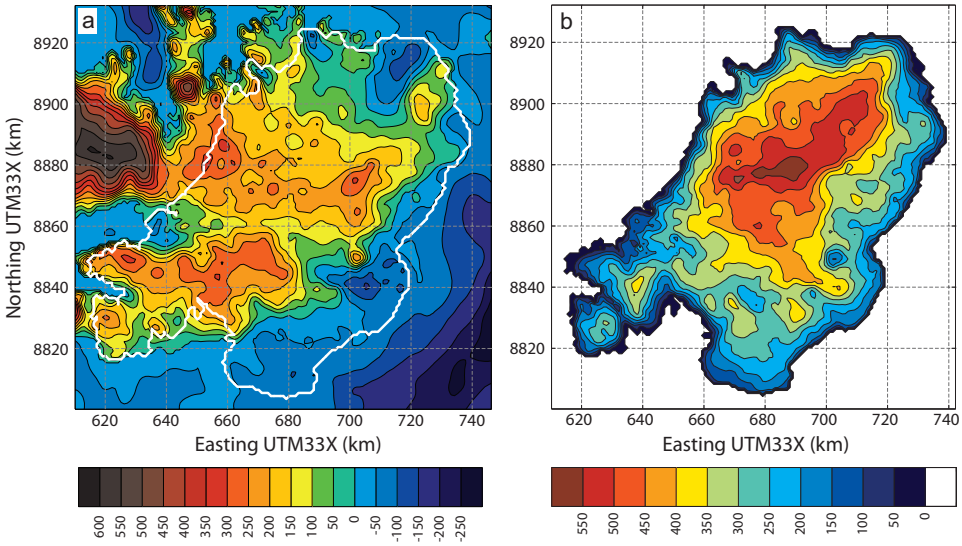

Figure III.2: Maps of (a) the bedrock topography and (b) modern observed ice thickness. The white solid line in (a) indicates the modern observed glacier outline. Contours are spaced at 50 m.

a large extent grounded below sea level and form a continuous calving front towards the Barents Sea. Several of the drainage basins are known to have surged in the past, specifically Etonbreen (1938 or earlier) in the west and Bråsvellbreen (1937–38) and Basin-3 (between 1850 and 1873; Fig. III.1)in the southeast. Observations do not span one entire surge cycle of any of these basins. Based on the approximate mass transfer from the reservoir into the receiving zone, the duration of the quiescent phase has been estimated as ∼150–500 a (Schytt, 1969; Solheim, 1991), considerably longer than for smaller glaciers in western Svalbard or other areas in general (Dowdeswell *et al.*, 1991). Over 28 % of the entire area covered by Austfonna lies below sea level (Dowdeswell, 1986), while for individual basins, headed by Bråsvellbreen, the figure is as large as 57 %. The lowest bedrock elevations, >150 m below sea level, are found in depressions below the lower reaches of Basin-3 and Leighbreen (Fig. III.2). The calving margins of the marine grounded ice add up to a total length of ∼230 km (Dowdeswell *et al.*, 2008).

The ice cap is undergoing surface elevation changes that are potentially attributed to a build-up during a quiescent phase with interior thickening of up to $0.5\,\mathrm{m\,a^{-1}}$ and marginal thinning of $1{-}3\,\mathrm{m\,a^{-1}}$(Moholdt *et al.*, 2010a). Marginal thinning encompassing the stagnant receiving zones of the three known surge-type basins, which are characterized

by depleted ice-surface profiles and low driving stresses, are both indicative of glaciers in an early quiescent phase (Dowdeswell, 1986). Basins with steep ice-surface profiles and relatively high marginal shear stresses are interpreted to be frozen to their beds and may also be surge-type, particularly if they contain ice regions grounded below sea level (Dowdeswell, 1986). Space-borne radar interferometry of Austfonna from the mid-1990s revealed a velocity structure of a slow-moving polar ice cap ($<10\,\mathrm{m\,a^{-1}}$) interrupted by distinct fast flow units having velocities $>100\,\mathrm{m\,a^{-1}}$ (Dowdeswell *et al.*, 1999). Bevan *et al.* (2007) suggested that slow ice motion is the key factor for the interior thickening, since the actual ice flux across the equilibrium line appeared to be only half the balance flux. Changes in the accumulation/ablation pattern have been suggested as an alternative mechanism of the observed geometric changes (Bamber *et al.*, 2004). This is not supported by observations of surface mass balance (SMB). In situ data from shallow ice cores do not indicate a significant trend in the net SMB of the accumulation area for the time period 1963–86 and 1986–98/99 (Pinglot *et al.*, 2001), although large interannual variations in the total amount of snow accumulation have been observed in recent years (Taurisano *et al.*, 2007; Dunse *et al.*, 2009). These observations also indicate a clear asymmetry in snow accumulation that is reflected in the net SMB (Schuler *et al.*, 2007) and, hence, the ELA: about 450 m a.s.l. in the northwest and 300 m a.s.l. in the southeast (Moholdt *et al.*, 2010a). Geodetically derived mass balance over the time period 2002–08 suggests a net SMB close to zero (Moholdt *et al.*, 2010a). However, the net mass balance of Austfonna is negative, $-1.3 \pm 0.5\,\mathrm{km^3\,a^{-1}}$, due to significant retreat of the marine margins (Dowdeswell *et al.*, 2008; Moholdt *et al.*, 2010a).

III.2.2 Thermal regime

Austfonna's thermal structure is described as polythermal (Dowdeswell *et al.*, 1986), although no direct evidence of a considerable temperate ice volume is available. In the firn area, latent heat release from internal refreezing of surface meltwater contributes significantly to warming the near-surface firn and ice. Current near-surface (10 m) temperatures in the firn area exceed those in the ablation area, despite lower air temperatures (e.g. Zagorodnov *et al.*, 1989a, and as evident in our thermistor measurements in the ablation area of Etonbreen and at the summit from 2006–10; T.V. Schuler). Direct measurements of the temperature distribution throughout an entire ice column are available from a borehole at the summit area, drilled in 1987 (Zagorodnov *et al.*, 1989a). The vertical temperature profile shows that the bulk of the 567 m thick ice column is cold, underlain by an isothermal basal layer ∼30 m thick that is close to PMP. A temperature minimum

of −8°C at ∼160 m depth at the drilling site is associated with lower temperatures during the Little Ice Age, when firn warming was presumably insignificant (Zagorodnov *et al.*, 1989b). The temperature gradient in the lower 400 m suggest a moderate geothermal heat flux of ∼40 mW m^{-2} (Ignatieva and Macheret, 1991). Information on the thermal structure of the ice cap is also contained in the airborne RES data (Macheret *et al.*, 1991). An internal reflection horizon (IRH), separating a transparent zone above and a zone of high backscatter below, may be associated with the cold-temperate-transition surface (CTS). Such IRHs are characteristic for many glaciers in Spitsbergen/western Svalbard (Björnsson *et al.*, 1996). The Institute of Geography, USSR Academy of Sciences, collected such data in 1984 (Macheret and Vasilenko, 1988). Similar to the RES data of Dowdeswell *et al.* (1986), the absence of a continuous IRH indicates that significant volumes of temperate ice do not exist. Kotlyakov and Macheret (1987) and Macheret and Vasilenko (1988) noted that the absence of continuous IRHs does not exclude the presence of a thin bottom layer of temperate ice, nor the occurrence of water at the ice/bed interface, because a thin layer of temperate ice may not be resolved by the radar system. The vanishing of bedrock returns in some regions, such as Leighbreen, may indicate the presence of a localized basal temperate layer. A simple theoretical consideration leads to a similar result: given a constant temperature gradient determined by the geothermal heat flux, an ice thickness >500 m, which is about the maximum ice thickness of the ice cap, is required to approach PMP when internal strain heating is neglected. Without a significant contribution from strain heating or latent heat release by infiltrating surface meltwater, the bulk of the ice cap is expected to be cold, but potentially underlain by a temperate base.

III.2.3 Basal properties

Turbid meltwater plumes arising from several points beneath the marine ice margin of Austfonna provide evidence that the marine grounded areas are, at least to some extent, underlain by soft sediments and subjected to basal water flow (Macheret and Vasilenko, 1988; Dowdeswell *et al.*, 1999). Furthermore, Solheim and Pfirman (1985) and Solheim (1986) mapped continuous submarine sediment ridges in front of Bråsvellbreen and Basin-3 and conclude that these ridges were partly pushed up by the advancing surge front and partly deposited by vigorous meltwater drainage along the entire surge front during the period of maximum extension. A rhombohedral pattern of linear, discontinuous sediment ridges and mounds is interpreted as being formed by a squeeze-up process, filling bottom crevasses that opened during surge advance. After surge termination, the surge

lobe was stagnant and subglacial features have been preserved. These subglacial sediments may originate from glacial erosion of the underlying bedrock and/or marine sedimentation during periods when the glacier extent over the seabed was considerably smaller then today, e.g. the Holocene Optimum ∼9 to 5 ka BP (Hjort *et al.*, 1995; Blake, 2006). A geological map of Nordaustlandet published by the Norwegian Polar Institute (NPI) indicates that an east-west line along Wahlenbergfjorden separates hard bedrock types in the north, i.e. Late Precambrian Hecla Hoek rocks and Caledonian granite/migmatide complexes, from soft bedrock types in the south, i.e. flat lying young sediments of Middle Carboniferous to Lower Cretaceous age (Lauritzen and Ohta, 1984). Information on bedrock type for presently glacierized areas is not available but it is noteworthy that the known surge-type basins Etonbreen and Bråsvellbreen are located adjacent to the soft, easily erodible bedrock types.

III.3 Model

We employ the ice sheet model SICOPOLIS (SImulation COde for POLythermal Ice Sheets; http://sicopolis.greveweb.net/), which solves the thermomechanically coupled field equations: the equations of mass, momentum and energy, along with Glen's flow law as constitutive equation and boundary conditions for the free surface and the bed.

Table III.1: Physical parameters used in all model experiments.

Quantity	**Value**
Gravitational acceleration, g	$9.81\,\mathrm{m\,s^{-2}}$
Density of ice, ρ	$910\,\mathrm{kg\,m^{-3}}$
Density of sea water, ρ_{sea}	$1028\,\mathrm{kg\,m^{-3}}$
Flow law exponent, n	3
Rate factor, $A(T')$	Arrhenius law in the form of Greve *et al.* (1998)
Flow enhancement factor, E	3
Melting point at atm. pressure, T_0	273.15 K
Heat conductivity of ice, κ	$9.828\ \mathrm{e}^{-0.0057\,T\,[\mathrm{K}]}\,\mathrm{W\,m^{-1}\,K^{-1}}$
Specific heat of ice, c	$(146.3 + 7.253\,T\,[\mathrm{K}])\,\mathrm{J\,kg^{-1}\,K^{-1}}$
Latent heat of ice, L	$335\,\mathrm{kJ\,kg^{-1}}$
Clausius-Clapeyron constant	$8.7 \times 10^{-8}\,\mathrm{K\,Pa^{-1}}$
Geothermal heat flux	$40\,\mathrm{mW\,m^{-2}}$
Sliding parameter, C_{b}	
– for hard rock, C_{r}	$10^5\,\mathrm{a^{-1}}$
– for soft sediments, C_{s}	$500\,\mathrm{a^{-1}}$

In addition, a jump condition is solved for the cold-temperate transition surface that separates cold and temperate ice regions (Greve, 1997). The model takes advantage of the simplification of the field equations known as the shallow-ice approximation (Hutter, 1983; Morland, 1984). Under the assumption that typical length scales exceed vertical scales, the stress in the ice reduces to the shear stress, τ, in the horizontal plane, and the hydrostatic pressure $P = \rho g(h - z)$, where ρ is the ice density, g the gravitational acceleration, h the surface elevation and z the height within the ice column counted positive upward. The resulting effective stress $\sigma = P|\nabla h|$ reveals that ice flow only depends on local ice thickness and surface slope and is aligned with the surface gradient. The total ice flow is the sum of the ice flow by internal deformation and basal sliding, the latter will be discussed in more detail in Section III.3.1.

The thermomechanical coupling of the model equations stems from the dependence of the rate factor on ice temperature and water content. The temperature evolution in the cold ice is balanced by horizontal and vertical advection, vertical heat conduction and dissipative strain heating. In the temperate ice, the temperature follows directly from the pressure field and the energy balance is provided by an evolution equation for the water content. Basal melting is computed by balancing the heat fluxes from the ice and the lithosphere and the heat generated by basal sliding. The geothermal heat flux is applied as a boundary condition 5 km below the ice base to account for the thermal inertia of the lithosphere (Ritz, 1987). Isostatic adjustment of the lithosphere due to changes in ice load is computed by the elastic lithosphere/relaxing asthenosphere approach (see Greve and Blatter, 2009, and references therein).

Simulations are run on a fixed rectangular grid at 2 km horizontal resolution encompassing 69×67 gridpoints in the horizontal plane. The vertical resolution comprises 81 gridpoints in the cold ice column, with increased spatial resolution towards the base, and 11 equally distributed grid points each in the temperate part of the ice column, if applicable, and the lithosphere. A fixed time-step of 0.025 years is used for all simulations in this study, except when a different value is stated. The values of relevant physical parameters are listed in Table III.1. The model is forced by monthly mean air temperature, monthly mean precipitation, sea level stand and geothermal heat flux. See Greve (1997) for more details on how SICOPOLIS computes the surface mass balance from the given input fields and accounts for firn warming and superimposed-ice formation.

III.3.1 Basal sliding

The dynamic boundary condition at the glacier bed is given by a Weertman-type sliding law (Greve and Blatter, 2009). Typically, sliding is enabled for a temperate ice base and no-slip conditions prevail for a cold base frozen to the ground. Here, we use a modified expression of the basal sliding velocity, v_b, following Hindmarsh and Le Meur (2001) and Greve (2005), that allows for partial sliding as the basal temperature approaches PMP, termed 'submelt sliding':

$$v_\mathrm{b}(T'_\mathrm{b}) = -\frac{C_\mathrm{b}}{\rho g}\frac{|\tau_\mathrm{b}|^{p-1}}{N_\mathrm{b}^q}\tau_\mathrm{b}\exp\left(\frac{T'_\mathrm{b}}{\gamma}\right) \tag{III.1}$$

where τ_b is the basal shear stress, N_b the basal pressure, C_b, p and q are the sliding law coefficient and exponents and T'_b the basal temperature relative to PMP. Full sliding is enabled for a temperate ice base and exponentially decreases when basal temperatures drop below PMP. The transition between no-slip and slip conditions at the glacier base is prescribed by a submelt-sliding parameter, γ, expressed in °C. It defines the temperature deviation from PMP, for which full sliding is reduced by a factor e^{-1}. A large positive value of γ allows for initiation of sliding well below PMP in a smooth way. A small positive value, leads to abrupt onset of sliding close to PMP. The basal pressure is given either by the full hydrostatic ice-overburden pressure P_f,

$$P_\mathrm{f} = \rho g H_\mathrm{i}, \tag{III.2}$$

or by the reduced basal pressure P_r, the difference between the ice-overburden pressure and the basal water pressure. To account for the buoyancy force exerted upon the ice volume submerged below sea level, the basal water pressure is assumed to equal the sea water pressure,

$$P_\mathrm{r} = P_\mathrm{f} - \rho_\mathrm{sw} D_\mathrm{w}, \tag{III.3}$$

where ρ_sw is the density of the sea water and D_w the water depth. Note that drainage of basal water from beneath the marine terminus requires an additional pressure head in order to overcome the sea water pressure (Pfeffer, 2007). To assure numerical stability and to keep sliding velocities given by Equation III.1 within a reasonable range, P_r is constrained to be $\geq 0.2 \times P_\mathrm{f}$.

III.3.2 Calving

Grounded marine-ice margins typically constitute a vertical calving front that fulfils a certain stability criterion, i.e. the actual ice thickness must exceed the flotation thickness at all times ($H_\mathrm{i} \geq \rho_\mathrm{sw}\,\rho^{-1}\,D_\mathrm{w}$). Otherwise the grounded margin will either disintegrate or form a floating ice tongue or ice shelf. Models using a fixed grid in the map plane usually lack the ability to track the position of the calving front on a subgrid scale. Nevertheless, the models can simulate a retreat of a marine ice margin by setting H_i at particular gridpoints to zero. Advances of the calving front, however, require the marine-ice margin to protrude at least one gridcell in one single time-step while overcoming the stability criterion. This cannot be realized at reasonable flow velocities. To bypass this shortcoming, models usually allow the ice to extend underwater without becoming afloat. Here, this 'underwater ice' is treated as regular ice, but is further subjected to calving that acts on its surface as an additional ablation term. We employ a modified version of the calving parameterization of Marshall *et al.* (2000) that relates the calving flux, Q_c, to the water depth, D_w, to some power k and the ice thickness, H_i, to some power l:

$$Q_c = k_c {D_w}^k {H_i}^l, \tag{III.4}$$

where k_c is a calving parameter that may include effects of margin geometry, longitudinal stress gradients, ice temperature or hydraulic fracturing. Here we keep it simple and set k_c to $10^{-4}\,\mathrm{m}^{-1}\,\mathrm{a}^{-1}$, and $k = l = 1$. This parameter choices enable retreat and advance cycles of marine grounded ice margins within a bathymetric range comparable with modern observed values. Increasing of the calving parameter to $k_\mathrm{c} = 10^{-3}\,\mathrm{m}^{-1}\,\mathrm{a}^{-1}$ leads to retreat of the marine grounded basins to shallow waters, as characteristic for the fjord heads in the northwest, while the deeper southeastern areas become completely and permanently deglacierized.

This treatment of marine ice represents an improvement to earlier approaches in large-scale ice sheet models that limit the marine ice extent by defining a bathymetric contour at which the ice is simply cut-off, either described by a constant value (Tarasov and Peltier, 1997) or a function of sea-level (Zweck and Huybrechts, 2005). A new concept of subgrid parameterization of ice-front motion that maintains a vertical calving front has recently been applied to another large-scale finite-difference ice sheet model (Albrecht *et al.*, 2010). This approach provides a promising basis for implementation of physical based calving laws such as the waterline crevasse-depth model of (Benn *et al.*, 2007).

III.3.3 Input data and initialization

The required model input consists of surface and bedrock topography, providing the initial ice cap geometry, the climate forcing in terms of precipitation and air temperature fields, sea level stand and geothermal heat flux.

The surface elevations above sea level are based on a 1 : 250 000 map of Svalbard (Sheet 3) published by NPI in 1998. The bathymetry is represented by the publicly available International Bathymetric Chart of the Arctic Ocean, Version 2.0 (Jakobsson *et al.*, 2008) having a horizontal resolution of 2 km (Figs. III.1 and III.2a). The maximum ice thickness of almost 600 m coincides with the central dome (Fig. III.2b). The bedrock beneath the ice cap is derived by subtracting scattered ice-thickness data from the surface topography. We supplement the airborne RES data published by Dowdeswell *et al.* (1986) with two new datasets from spring 2008. The Danish National Space Centre acquired 60 MHz airborne RES data, while a ground team collected 20 MHz ground-penetrating radar data along profiles of ∼800 km length (Vasilenko *et al.*, 2010). The profiles follow the routes investigated by the University of Oslo and NPI for mass-balance purposes since 1998 (Schuler *et al.*, 2007; Taurisano *et al.*, 2007; Dunse *et al.*, 2009) and cover special areas of interest, such as Duvebreen and Basin-3.

We have derived an idealized present-day climate based on field data acquired since 1998 and ERA-40 and ERA-Interim re-analysis. The air temperature input is based on a 5-year record (2004–09) collected by an automatic-weather station on Etonbreen at an elevation of 510 m a.s.l., 50–100 m above the recent mean ELA. Monthly mean temperatures are distributed over the entire model domain using a mean lapse rate of $-0.0045\,\mathrm{K\,m^{-1}}$ (Schuler *et al.*, 2007). The precipitation field is based on ERA-40/ERA-Interim re-analysis at a 6 hour temporal resolution for the period 1960–06. Monthly mean precipitation fields have been downscaled using a simple precipitation model (Smith and Barstad, 2004; Schuler *et al.*, 2008). The precipitation fields are kept constant over the entire model period while we allow the surface temperature to adjust for changes in ice-surface elevation given the constant lapse rate. Application of this idealized present-day climate on the present-day topography leads to a net SMB close to zero ($+0.07\,\mathrm{m\,w.e.\,a^{-1}}$), in agreement with recent observations for the time period 2002–08 (Moholdt *et al.*, 2010a).

The vertical temperature profile through the ice at the summit presented by Zagorodnov *et al.* (1989b) indicates a geothermal heat flux of $\sim 40\,\mathrm{mW\,m^{-2}}$ (Ignatieva and Macheret, 1991). The ice temperature for the initial state assumes a steady-state temperature gradient according to the geothermal heat flux, while the annual mean air temperature constrains the temperature at the ice surface. The temperature within the ice volume is

limited to the basal PMP determined by the ice-overburden pressure. At the summit, good agreement of the initial temperature profile with the observed one is achieved for the lower 400 m. In the upper layer, the initial ice temperatures are too low. However, after ∼100 model years, the firn-warming routine of SICOPOLIS has established a temperature profile in the summit area similar to the observed one, throughout the entire ice column.

III.3.4 Model experiments

We define a series of model experiments (Exp ♯1–♯5), each characterized by a unique combination of the sliding-law parameters C_b, p, q and N_b. The individual experiments represent a broad range of potential basal environments, facilitating basal motion to a varying degree, from hard rock or completely immobile sediment/permafrost to soft water-saturated sediments. Table III.3.4 lists relevant parameter used in all model experiments. Exp ♯1 considers sliding over hard rock everywhere with basal pressure given by the hydrostatic ice-overburden pressure. Exp ♯2 also considers sliding over hard rock everywhere, but reduced basal pressure applied for the marine grounded parts of the ice cap. Exp ♯3 and ♯4 differ from Exp ♯1 and ♯2 by a 3-fold enhancement of basal sliding of the marine grounded ice. Exp ♯5 applies a linear sliding law to the marine grounded ice and represents fast basal motion by plastic deformation of water-saturated sediments (Hindmarsh, 1997; Tulaczyk *et al.*, 2000). Each experiment was run four times using different values of γ: 0.05, 0.2, 0.5 and 1.0°C, describing a progressively smoother transition from no-slip to full basal sliding.

Table III.2: Sliding-law parameter combinations of the 5 model experiments. The sliding-law coefficient C_b (C_r for hard rock and C_s for soft sediments as specified in Table III.1) and the exponents p and q are first given for ice areas resting on land, than for the ice areas grounded below sea level. N_b is either the full (P_f) or reduced basal pressure (P_r). Note that in the case of a linear sliding law (marine grounded ice in Exp ♯5) basal sliding is independent of the basal pressure (because of exponent $q = 0$).

Exp	$\boldsymbol{C}_\mathrm{b}$	$\boldsymbol{p}$	$\boldsymbol{q}$	$\boldsymbol{N}_\mathrm{b}$
♯1	$C_\mathrm{r} \mid C_\mathrm{r}$	3 | 3	2 | 2	$P_\mathrm{f} \mid P_\mathrm{f}$
♯2	$C_\mathrm{r} \mid C_\mathrm{r}$	3 | 3	2 | 2	$P_\mathrm{f} \mid P_\mathrm{r}$
♯3	$C_\mathrm{r} \mid 3{\times}C_\mathrm{r}$	3 | 3	2 | 2	$P_\mathrm{f} \mid P_\mathrm{f}$
♯4	$C_\mathrm{r} \mid 3{\times}C_\mathrm{r}$	3 | 3	2 | 2	$P_\mathrm{f} \mid P_\mathrm{r}$
♯5	$C_\mathrm{r} \mid C_\mathrm{s}$	3 | 1	2 | 0	$P_\mathrm{f} \mid$–

All model experiments take the present-day geometry of Austfonna as the initial condition. The present-day reference climate is applied as external forcing. We run the model for 30 ka and evaluate the last 5 ka when all runs have reached a state with negligible long-term trends, i.e. the temporal evolution of a particular variable is described by a stationary signal.

III.4 Results

In Section III.4.1 we provide an overview of all experiments (Exp ♯1 – ♯5) over the full range of γ. Based on the temporal variability of ice cap variables we then present particular runs that generate an ice cap characterized by permanent fast flow (Sec. III.4.2) and oscillatory fast flow, including cyclic surge-type behaviour (Sec. III.4.3), and show contour maps of selected field variables as well as the temporal evolution of the ice thickness at specific locations to provide indicators of individual basin activity.

III.4.1 Mean ice cap size and variability

Total ice volume, areal extent and basal area at PMP are presented in Figure III.3. The left panels (a, b, c) give mean values while the associated variability is shown to the right (d, e, f). The temporal variability is expressed in terms of two standard deviations normalized by their respective mean value to capture the amplitudes of the stationary signal ($\sim$95 % of the respective output variable is then contained, assuming a normal distribution). Both progressively increasing enhancement of basal sliding (Exp ♯1 – ♯5) as well as an increasing value of γ lead to a smaller ice cap in terms of volume and areal extent, a consequence of increasing mass transport from the interior of the ice cap towards the margins. The dashed lines (Fig. III.3a and b) indicate a $\pm$10 % region around the current ice volume and areal extent, marked by solid lines. Assuming that Austfonna is close to equilibrium, model runs using $\gamma = 0.2$°C generally provide the best fit of simulated to current ice-cap size. For Exp ♯5, best fit is achieved using $\gamma = 0.05$°C. The simulated temperate basal area is largest in the case of Exp ♯1, sliding over hard rock, and smallest in the case of Exp ♯5, deformation of soft sediments, coinciding with the largest and smallest ice volume, thickest and thinnest ice, respectively.

Concerning the temporal variability, an abrupt onset of basal sliding, represented by a small value of γ, leads to large fluctuations in the presented quantities (Fig. III.3d, e, f). Comparing the different experiments for a given γ, Exp ♯5, the experiment with most

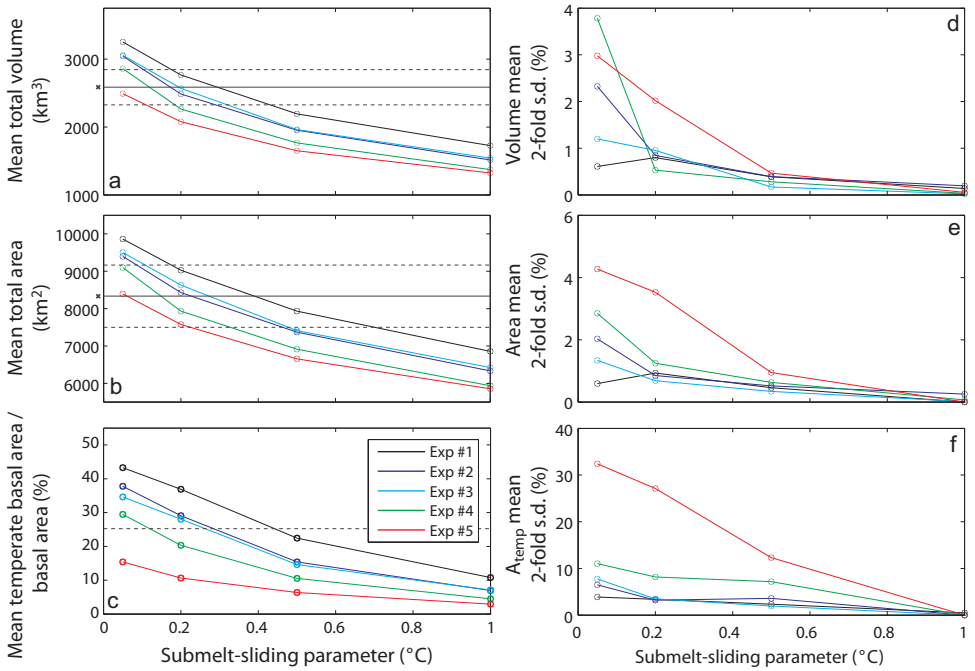

Figure III.3: Comparison of all five model experiments with varied submelt-sliding parameter, γ. Mean values of (a) total volume, (b) total glacierized area and (c) percentage of temperate basal area relative to the total area for the time period 25–30 ka and their associated two-fold standard deviation normalized with respect to the mean (d, e, f). The grey dashed lines envelope model results within 10 % of the modern observed values (a, b) marked by a solid grey line. The modern basal area at PMP (dashed line in panel c) follows from theoretical considerations using ice cap geometry and geothermal heat flux.

enhanced basal motion, yields largest variability. The fluctuations rapidly decrease for progressively smoother onset of basal motion, and for $\gamma = 1$°C the variability has vanished in all experiments. For Exp ♯5, significant variability also exists for $\gamma = 0.2$ and 0.5°C. In terms of normalized standard deviations, the fluctuations in areal extent are up to two times larger than those in volume, indicating that mass redistribution dominates over mass changes. This redistribution is effected by an ice flux far in excess of the balance flux. Fluctuations in basal areal extent at PMP are even larger than fluctuations in total areal extent, as high as 32.4 % in the case of Exp ♯5 with $\gamma = 0.05$°C.

Figure III.4 demonstrates the effect of abruptness in sliding onset (described by different values of γ) on the temporal evolution of the ice cap by means of time series of the areal

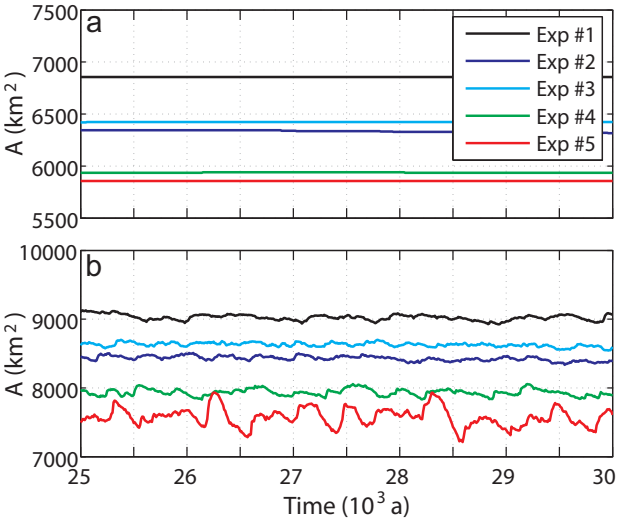

Figure III.4: Time series of total glacierized area for a quasi-steady-state time period of model year 25 to 30 ka and all model experiments. Model runs with (a) γ set to 1°C, and (b) γ set to 0.2°C, below.

extent, for two values of γ. Figure III.4a presents results for model runs using a smooth transition ($\gamma = 1.0$°C), and Figure III.4b presents those for an abrupt transition from no sliding to full sliding ($\gamma = 0.2$°C). When $\gamma = 1.0$°C (Fig. III.4a), the areal extent is constant over time and lacks temporal variability, whereas for $\gamma = 0.2$°C ((Fig. III.4b), temporal variability in areal extent exists for all experiments. For Exp ♯1 to Exp ♯4 fluctuations are clustered between 0.7 (Exp ♯3) and 1.2 % (Exp ♯4), while for Exp ♯5 they are significantly higher, at 3.5 % (Fig. III.3e).

III.4.2 Permanent fast flow

Based on the absence of temporal variability in scalar variables, Exp ♯1 with $\gamma = 1.0$°C is classified as permanent fast flow. Figure III.5 shows the basal velocity field and the basal temperature relative to PMP in the steady state. This experiment did not yield temporal fluctuations, hence only one arbitrary time slice is shown. Basal sliding dominates the overall flow everywhere and the surface velocity field (not provided here) looks very similar. The bulk of the ice cap is slow ($<10\,\mathrm{m\,a^{-1}}$), interrupted by several fast flow units with moderate velocities of 50–150 $\mathrm{m\,a^{-1}}$. The flow units coincide with the warmest basal areas, but sliding is already initiated at basal temperatures ∼2°C below PMP. The flow

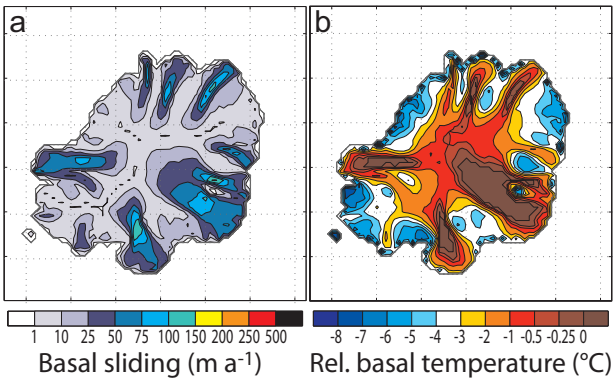

Figure III.5: (a) Steady-state basal velocity and (b) basal temperature relative to PMP for Experiment ♯1 with γ set to 1°C. The modelled glacier outline is indicated by the grey solid line.

units also coincide with valleys and troughs of the bed topography where ice thickness is greatest, facilitating enhanced basal shear and basal temperatures.

An intriguing result is the absence of significant volumes of temperate ice, indicating that regional fast flow is accomplished exclusively by basal motion in regions where the glacier base is near PMP. This result agrees with the observations of the thermal structure of Austfonna.

III.4.3 Oscillatory fast flow

Experiment ♯5 reveals the largest variability in ice-cap geometry, suggesting that spatial and temporal variability exist in ice-cap dynamics. Using $\gamma = 0.2$°C leads to a variability similar in magnitude to that found using the extreme case of $\gamma = 0.05$°C. We discuss the case of $\gamma = 0.2$°C as this model run illustrates oscillatory fast flow including cyclic surge behaviour very well (Fig. III.6).

Some drainage basins, e.g. Leighbreen and Basin-3 (Fig. III.1 for location), are active at all given instances, but with variable flow intensity. Basin-3 seems capable of generating large-scale surges (Fig. III.6d; 29.67 ka). Other basins are only active at short periods in time when they show very high basal velocities ($> 500\,\mathrm{m\,a^{-1}}$ up to several $\mathrm{km\,a^{-1}}$) but otherwise have very low activity for most of the time, e.g. Etonbreen (Fig. III.6a; 29.2 ka) and Basin-5 (Fig. III.6b; 29.43 ka). As in the runs that produce permanent fast flow (Section III.4.2), no significant volumes of temperate ice exist. Fast flow is now

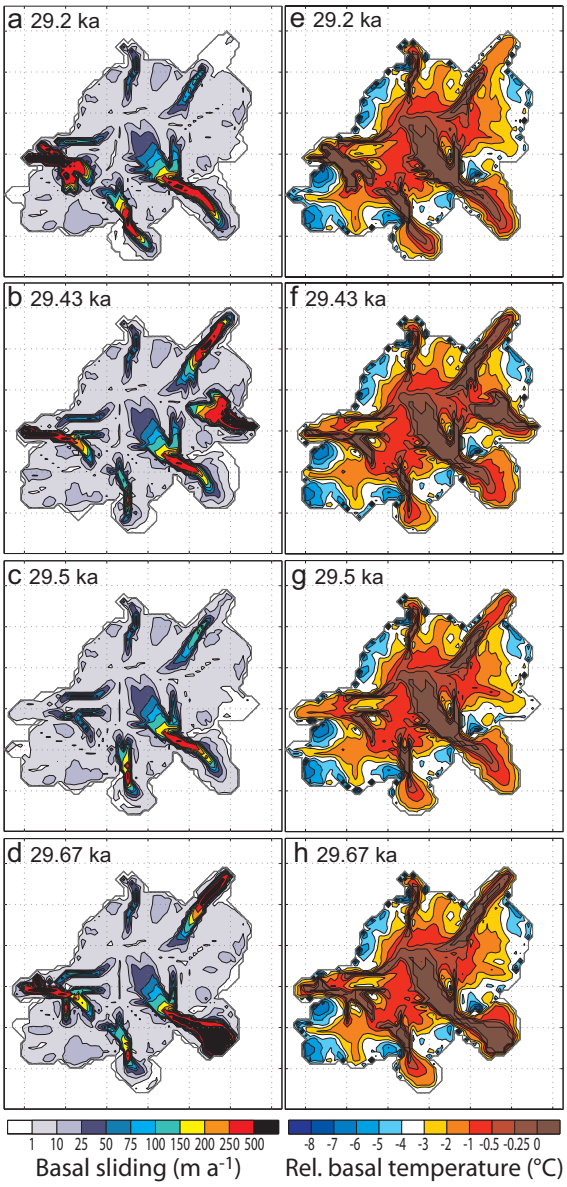

Figure III.6: Snapshots of the basal velocity (left panels) and basal temperature relative to PMP (right panels) at indicated model years for Experiment ♯5 with γ set to 0.2°C.

strictly confined to the basal areas at or very close to PMP and large variations in basal temperature are observed for the surging basins. The active phase is associated with a bed at or close to PMP and entails massive mass fluxes along the flowlines, whereas basal temperatures are below PMP during the quiescent phase. Figs. III.6b and f represent a time when the ice cap is characterized by increased fast-flow and surges (29.43 ka) before the activity reduces again and the surge lobe of Basin-5 has become stagnant (Fig. III.6c and g; 29.5 ka).

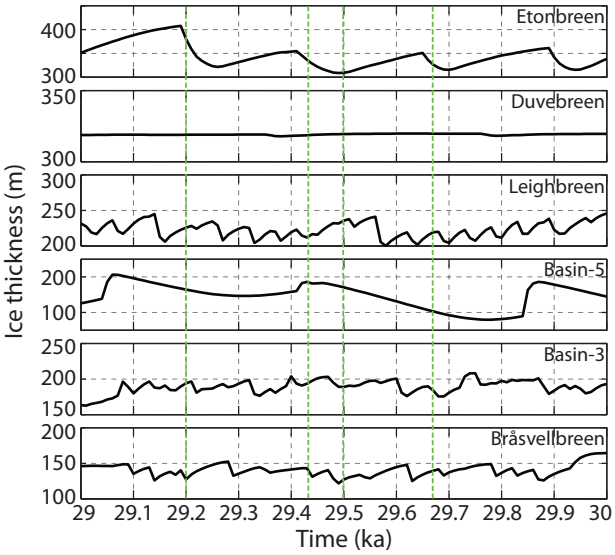

Figure III.7: Mean ice-thickness evolution at specific points fixed in space on individual basins during Experiment ♯5 with γ set to 0.2°C. The dashed green lines indicate the times represented in Fig III.6.

To investigate the behaviour of individual drainage basins and the periodicity of their oscillations, we present temporal ice thickness variations at specific locations, lined up in 2 km intervals along the modern ELA, i.e. the elevation contour of 450 m a.s.l. in the northwest and 300 m a.s.l. in the southeast. These points are fixed in space and change their relative position in the course of the simulation both with respect to both the simulated ELA and DBL. Groups of 7–12 specific points are selected to represent a particular basin. Individual points within the group may show different behaviour, e.g. some points may become ice-free, periodically, and only glacierized in the case of a considerable advance of the terminus during a large-scale surge event. Temporal variations in the ice thickness of

individual basins differ in both period and amplitude (Fig. III.7). Etonbreen and Basin-5 show very marked oscillations of regular frequency and large amplitudes of up to ∼100 m. Etonbreen shows gradual thickening followed by abrupt thinning, whereas Basin-5 is characterized by abrupt thickening followed by gradual thinning. The contrasting behaviour of periodic thickening and thinning can be explained by the migration of the simulated ice divide towards the northwest, moving the specific points from their location along the modern ELA well into the reservoir zone (Etonbreen) or receiving zone (Basin-5). Leighbreen, Basin-3 and Bråsvellbreen show fluctuations of smaller amplitude and at higher frequencies, while Duvebreen shows very little change in time. Spectral analysis of the individual time series reveals principal periods in the range of 200–500 years for all basins, in conformity with the estimated periods of large-scale surge events (150–500 years). While Etonbreen and Basin-5 show typical surge-type behaviour with short-lived surge events following long quiescent phases, Leighbreen, Basin-3 and Bråsvellbreen may be also be surge-type, but they maintain spatially limited fast flow with minor oscillations on a decadal timescale between large-scale surge events.

III.5 Discussion

We have shown that by choosing distinct combinations of the parameters in the basal-sliding law, representing a relatively abrupt onset of basal motion and enhanced sliding of marine grounded ice, SICOPOLIS generates an ice cap with similar dynamics to Austfonna. With regards to the observational evidence, the experiment describing soft sediments beneath marine grounded ice is considered the most realistic scenario. However, a perfect match of the simulated and modern observed ice cap in terms of glacier outline, geometry and surface velocities is not achieved. Each experiment represents homogeneous idealizations of the basal conditions, whereas actual basal conditions, such as bedrock lithology, thickness and water-saturation of subglacial sediments vary both spatially and temporarily. Therefore, sliding parameters should ideally be functions of space and time, rather than constants. Furthermore, variations in basal water pressure associated with changes in the basal hydraulic system will occur beneath the real ice cap, but are not taken into account in the model. Nevertheless, the evolution of the subglacial hydrology is expected to go hand in hand with the basal thermal regime: once the basal temperature reaches PMP, basal melt can occur. If the hydraulic conductivity of the bedrock and an emerging basal hydraulic drainage system are low, local water storage increases the basal water pressure. This weakens subglacial sediments, if present, facilitating enhanced basal

motion as represented by Exp ♯5 and providing a potential surge mechanism as suggested earlier by (Fowler *et al.*, 2001). In the following, we will describe the evolution of a surge cycle and the underlying mechanisms.

III.5.1 Through a surge cycle

In agreement with field observations and theory, fast flow is achieved primarily by basal motion. Abrupt flow oscillations are thus governed by temporal variations in basal motion and closely related to the basal thermal regime. Björnsson *et al.* (1996) have shown that the basal thermal regime of Svalbard glaciers is closely linked to ice thickness.

During the quiescent phase of a surge-type basin, the basal temperature is below PMP over a large fraction of the bed. The reservoir zone experiences substantial thickening, while the receiving zone is subjected to severe thinning and retreat. The increased ice thickness leads to increased insulation from the cold atmosphere and increased overburden pressure, the latter resulting in increasing basal shear and hence, dissipative strain heating. The bed eventually approaches PMP in the interior of the ice cap. Sliding sets in according to the chosen γ and initiates the active surge phase. Friction generated by basal motion generates additional heat. Compressive flow in a boundary zone where

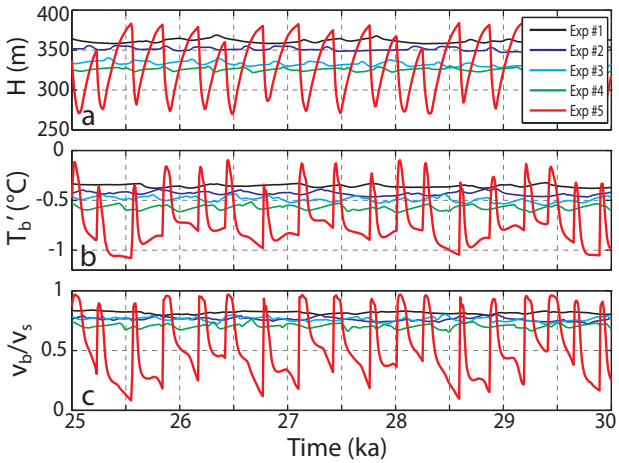

Figure III.8: (a) Ice thickness evolution, (b) basal temperature relative to PMP, T'_{b}, and (c) relative contribution of basal motion to the overall ice flow, i.e. the surface motion, at one specific location on Etonbreen. Time series data is given for the period 25–30 ka and for all five experiments using $\gamma = 0.2$°C.

fast flowing ice (basal motion enabled) meets slowly flowing ice (basal motion disabled or highly reduced) leads to local thickening and surface steepening, provoking local enhancement of basal shear stress and strain heating. This mechanism was described as a trigger of flow instabilities by (Payne, 1995). The warm-based area expands towards the margins and provides a mechanism for forward-propagation of the surge front. The advancing surge lobe is subjected to dynamic thinning and surface flattening thereby reducing both thermal insulation and generation of heat and the area affected by fast basal motion shrinks back upstream. Once the reservoir zone is tapped and the surface profile along the flowline flattened sufficiently, conditions for a temperate bed can no longer be maintained, basal motion becomes insignificant and brings the surge to a halt. Another quiescent phase is initiated, characterized by insufficient ice flux from the accumulation towards the ablation area and hence a gradual build-up of a reservoir zone. These distinct phases in the simulated surge cycle agree with those reported by (Calov *et al.*, 2002) and agree with observations of polythermal surge-type glaciers in other parts of Svalbard (Sund *et al.*, 2009). The simulated surge advances of ca. 10–15 km over widths of ∼15–25 km (Fig. III.6) are of similar size as the 1930s surge of Bråsvellbreen, during which the 30 km wide front advanced by ∼20 km (Schytt, 1969).

To describe the evolution of the surge cycles in detail, we extract time series data at one specific location on Etonbreen. Given the parameter combinations defined by Exp ♯5, the temporal evolution of ice thickness, basal temperature relative to PMP and relative contribution of basal motion to the overall ice flow at this location is clearly influenced by periodic surge-behaviour (Fig. III.8). The contribution of basal sliding vanishes, if the basal temperature relative to PMP falls below –1°C (Fig. III.8b,c). Basal motion becomes the dominant mechanism of glacier flow, i.e. >70 % of the total (surface) motion, if basal temperatures are within 0.7°C from PMP (Exp ♯1–♯4). The point at which basal motion becomes the principal flow mechanism does not coincide with a constant basal temperature, but rather falls within a critical temperature range, that allows for large variations in basal motion (Exp ♯5). This indicates that additional factors, e.g. the basal shear stress, determine the exact onset of fast basal sliding that initiates the surge phase. The sawtooth-shaped signal shows cycles of gradual thickening over 250–300 years followed by abrupt thinning over <50 years. Every ice-thickness peak precedes a corresponding peak in basal temperature (Fig. III.8a, Exp ♯5). No clear relation exist between the basal temperature and the phase of gradual thickening (quiescent phase), however, the mean ice thickness allows maintenance of basal temperatures within the critical temperature range. The basal shear stress increases with increasing ice thickness and increasing surface slope

(not shown in Fig. III.8) and eventually reaches a level at which basal sliding becomes dominant. Frictional heating ($v_b \cdot \tau_b$) provides a positive feedback mechanism to further increase basal temperatures and, hence, basal motion. Each peak in basal temperature coincides with a corresponding peak in the contribution of basal motion, the latter reaching up to ∼95%, the same fraction as observed during the 1982–83 surge of Variegated Glacier (Kamb *et al.*, 1985). Basal motion facilitates fast flow and results in rapid thinning and surface flattening (not shown). The resulting reduction in basal shear stress, limits internal heat sources and lowers the contribution of basal motion to the overall ice flow. It should be noted that the selected point has a bedrock elevation of 240 m a.s.l., i.e. the sliding law parameters at this location remain constant during all experiments. The differences between the experiments are thus of a purely geometric nature and only depend on the efficiency of the ice flux further downstream, where the ice is grounded below sea level and sliding parameters subjected to changes. Enhanced basal motion of the marine grounded ice also entails geometric changes in the interior ice cap, grounded above sea level, and is conducive to the generation of surge-type behaviour. The simulated surge-type behaviour therefore appears to be ultimately controlled by the geometric evolution of the glacier, as mentioned by Clarke (1976) and Raymond (1987).

III.5.2 Numerical robustness

The mechanism initiating oscillatory behaviour of ice sheets evokes some controversy among theoretical glaciologists. Bueler *et al.* (2007) and Bueler and Brown (2009) pointed out a numerical error arising from the abrupt transition from no-slip conditions at the ice base to full basal sliding that is employed by models such as those applied to EISMINT II experiment H (Payne *et al.*, 2000). The numerical artefact arises from a singularity in the horizontal velocity field that leads to infinite vertical velocities, and hence, unrealistic strain heating. The effect is smeared out in the case of large horizontal grid spacing of the order of 10 km, typical for large-scale ice sheet models, but becomes significant at finer grids (Bueler and Brown, 2009). Submelt sliding removes the singularity in the velocity field. Greve *et al.* (2006) and Calov *et al.* (2010) demonstrated that large-scale oscillations can also occur for a smooth transition of the warm-based and cold-based sliding regimes and also for a higher-order model that incorporates longitudinal stresses through a combination of SIA and SSA. The implementation of submelt sliding is in addition motivated by physical reasoning. Sliding is likely to occur on a subgrid-scale, before the entire area represented by a single gridpoint has reached PMP.

To test the robustness of the model experiments, we ran Experiment ♯5 using γ=0.05°C at different spatial (1, 2 and 4 km) and temporal (1, 0.1, 0.025 and 0.00625 years) resolutions. This model run was expected to be the most sensitive to numerical inaccuracies as it represents maximum sliding enhancement and the most abrupt transition from no-slip conditions to full basal sliding. With a time-step of 1 year, only the 4 km resolution run performed stably. However, the generated ice cap size is ∼10 % smaller than for the higher temporal resolutions for which the results converge. The runs at 2 and 1 km spatial resolution converge at a time-step of 0.025 years, although the result at 0.1 year differs only by ∼1 %. We conclude that a time-step of 0.025 years is sufficiently small for all three spatial resolutions. Using this, the total volume ranges from 2471 km^3 at 1 km resolution to 2490 km^3 at 2 km resolution ($<$ 0.8 %) and the total area from 8257 km^2 to 8437 km^2 ($<$ 2.2 %). The resulting mean ice thickness varies from 293 m at 1 km resolution to 300 m at 4 km resolution ($<$2.2 %). Slightly larger differences (12.5 %) exist for the area at PMP, ranging from 1257 km^2 at 1 km up to 1424 km^2 at 4 km resolution, probably associated with a larger mean ice thickness in the case of the 4 km resolution. The oscillatory behaviour is generally unaffected by the spatial resolution. Fluctuations in volume range from 1.2 (4 km) to 1.7 % (1 km), for areal extent from 1.9 (4 km) to 2.2 % (1 km), for mean ice thickness from 1.9 (2 km) to 2.2 % (1 km) and from 16.0 (1 km) to 19.7 % (4 km) for the basal area at PMP. The runs at 1 km spatial resolution give the largest temporal variation in most cases, but there is no unambiguous trend of the scalar variable values with resolution, and the differences do not indicate numerical instabilities. The slight differences in the mean and standard deviations of the presented variables can be explained by the fact that individual flow units are represented differently at the various spatial resolutions; some small and narrow flow units may be present at high and absent at low spatial resolution.

III.6 Concluding Remarks

The simulated dynamic behaviour of Austfonna is sensitive to the parameter combination of the applied sliding law. Submelt sliding in a defined temperature range and the strength of the sliding enhancement of marine ice determine whether spatially limited flow units operate in a mode of permanent or oscillatory fast flow. These results are in line with previous model experiments for the idealized HEINO setup by Greve *et al.* (2006) and Calov *et al.* (2010). In the case of cyclic surge behaviour, enhanced sliding during the active phase is required to draw down the ice surface sufficiently and to re-establish a

cold base, thereby initiating the quiescent phase. Considerable volumes of temperate ice do not occur in any of the model runs, indicating that fast flow is accomplished exclusively by basal motion over a temperate bed. The dynamic regime is shown to have a significant impact on the equilibrium size of Austfonna. Ice volume and areal extent decrease with both enhanced sliding and an increased temperature range at which submelt sliding is allowed to occur. The oscillatory behaviour generated by the model conforms with observational evidence of previous surge activity. However, none of the experiments result in an exact match of the simulated and modern observed ice cap, since the latter follows from an external-climatic and intrinsic-dynamic history with basal conditions being functions of space and time. Nevertheless, we have achieved a set of idealized initial conditions for prognostic model runs that allow us to assess the uncertainties in the dynamic response of the ice cap to climate change.

Acknowledgements

We thank H. Jiskoot and an anonymous reviewer for thorough and constructive comments that helped to improve this article. This study is a contribution to the International Polar Year project GLACIODYN funded by the Norwegian Research Council (grant 176076/S30). The final stage was supported by funding to the ice2sea project from the European Union 7th Framework Programme, grant No. 226375, ice2sea contribution No. 024. TD was supported by a short-term pre-doctoral fellowship through the Japan Society for the Promotion of Science (research stay at ILTS, Sapporo) and an Arctic field grant through the Svalbard Science Forum (fieldwork). TD thanks E. Vasilenko for guidance through relevant Russian publications and O. Salvigsen for providing insight into the geology of Nordaustlandet.

References

Albrecht, T., Martin, M., Haseloff, M., Winkelmann, R., and Levermann, A., 2010. Parameterization for subgrid-scale motion of ice-shelf calving-fronts. The Cryosphere, 4(3), 1497–1523.

Bamber, J., Krabill, W., Raper, V., and Dowdeswell, J., 2004. Anamolous recent growth of part of a large Arctic ice cap: Austfonna, Svalbard. Geophysical Research Letters, 31(12), L12402.

Benn, D. I., Hulton, N. R., and Mottram, R. H., 2007. 'Calving laws', 'sliding laws' and the stability of tidewater glaciers. Annals of Glaciology, 46, 123–130.

Bevan, S., Luckman, A., and Murray, T., 2007. Positive mass balance during the late 20th century on Austfonna, Svalbard revealed using satellite interferometry. Annals of Glaciology, 46, 117–122.

Björnsson, H., Gjessing, Y., Hamran, S. E., Hagen, J. O., Liestøl, O., Palsson, F., and Erlingsson, B., 1996. The thermal regime of sub-polar glaciers mapped by multi-frequency radio-echo sounding. Journal of Glaciology, 42(140), 23–32.

Blake, W., 2006. Occurrence of the Mytilus edulis complex on Nordaustlandet, Svalbard: radiocarbon ages and climatic implications. Polar Research, 25(2), 123–137.

Bueler, E. and Brown, J., 2009. Shallow shelf approximation as a "sliding law" in a thermomechanically coupled ice sheet model. Journal of Geophysical Research-Earth Surface, 114, F03008.

Bueler, E., Brown, J., and Lingle, C., 2007. Exact solutions to the thermomechanically coupled shallow-ice approximation: effective tools for verification. Journal of Glaciology, 53, 499–516.

Calov, R., Ganopolski, A., Petoukhov, V., Claussen, M., and Greve, R., 2002. Large-scale instabilities of the Laurentide ice sheet simulated in a fully coupled climate-system model. Geophysical Research Letters, 29(24), 2216.

Calov, R., Greve, R., Abe-Ouchi, A., Bueler, E., Huybrechts, P., Johnson, J. V., Pattyn, F., Pollard, D., Ritz, C., Saito, F., and Tarasov, L., 2010. Results from the Ice-Sheet Model Intercomparison Project – Heinrich Event INtercOmparison (ISMIP HEINO). Journal of Glaciology, 56(197), 371–383.

Clarke, G., 1976. Thermal regulation of glacier surging. Journal of Glaciology, 16(74), 231–250.

Clarke, G., 1987. Fast glacier flow - ice streams, surging, and tidewater glaciers. Journal of Geophysical Research-Solid Earth and Planets, 92(B9), 8835–8841.

Clarke, G., Collins, S., and Thompson, D., 1984. Flow, thermal structure, and subglacial conditions of a surge-type glacier. Canadian Journal of Earth Sciences, 21(2), 232–240.

Dolgoushin, L. and Osipova, G., 1975. Glacier surges and the problem of their forecasting. International Association of Hydrological Sciences Publications (Symposium at Moscow 1971–Snow and Ice), 104, 292–304.

Dowdeswell, J., 1986. Drainage-basin characteristics of Nordaustlandet ice caps, Svalbard. Journal of Glaciology, 32(110), 31–38.

Dowdeswell, J., Drewry, D., Cooper, A., Gorman, M., Liestøl, O., and Orheim, O., 1986. Digital mapping of the Nordaustlandet ice caps from airborne geophysical investigations. Annals of Glaciology, 8, 51–58.

Dowdeswell, J., G.S., H., and Hagen, J., 1991. The duration of the active phase on surge-type glaciers: contrasts between Svalbard and other regions. Journal of Glaciology, 37(127), 388–400.

Dowdeswell, J. A., Benham, T. J., Strozzi, T., and Hagen, J. O., 2008. Iceberg calving flux and mass balance of the Austfonna ice cap on Nordaustlandet, Svalbard. Journal of Geophysical Research-Earth Surface, 113(F3), F03022.

Dowdeswell, J. A., Unwin, B., Nuttall, A. M., and Wingham, D. J., 1999. Velocity structure, flow instability and mass flux on a large Arctic ice cap from satellite radar interferometry. Earth and Planetary Science Letters, 167(3-4), 131–140.

Dunse, T., Schuler, T. V., Hagen, J., Eiken, T., Brandt, O., and Høgda, K., 2009. Recent fluctuations in the extent of the firn area of Austfonna, Svalbard, inferred from GPR. Annals of Glaciology, 50(50), 155–162.

Fowler, A. C., Murray, T., and Ng, F. S. L., 2001. Thermally controlled glacier surging. Journal of Glaciology, 47(159), 527–538.

Glasser, N. F. and Hambrey, M. J., 2001. Styles of sedimentation beneath Svalbard valley glaciers under changing dynamic and thermal regimes. Journal of the Geological Society, 158, 697–707.

Greve, R., 1997. A continuum-mechanical formulation for shallow polythermal ice sheets. Philosophical Transactions of the Royal Society London A, 355(1726), 921–974.

Greve, R., 2005. Relation of measured basal temperatures and the spatial distribution of the geothermal heat flux for the Greenland ice sheet. Annals of Glaciology, 42, 424–432.

Greve, R. and Blatter, H., 2009. Dynamics of Ice Sheets and Glaciers. Springer, Berlin, Germany etc.

Greve, R., Takahama, R., and Calov, R., 2006. Simulation of large-scale ice-sheet surges: The ISMIP HEINO experiments. Polar Meteorology and Glaciology, 20, 1–15.

Greve, R., Weis, M., and Hutter, K., 1998. Palaeoclimatic evolution and present conditions of the Greenland ice sheet in the vicinity of Summit: An approach by large-scale modelling. Paleoclimates, 2(2-3), 133–161.

Hagen, J., Eiken, T., Kohler, J., and Melvold, K., 2005. Geometry changes on Svalbard glaciers: mass-balance or dynamic response? Annals of Glaciology, 42, 255–261.

Hamilton, G. S. and Dowdeswell, J. A., 1996. Controls on glacier surging in Svalbard. Journal of Glaciology, 42(140), 157–168.

Hindmarsh, R., 1997. Deforming beds: Viscous and plastic scales of deformation. Quaternary Science Reviews, 16(9), 1039–1056.

Hindmarsh, R. C. A. and Le Meur, E., 2001. Dynamical processes involved in the retreat of marine ice sheets. Journal of Glaciology, 47(157), 271–282.

Hjort, C., Mangerud, J., Adrielsson, L., Bondevik, S., Landvik, J. Y., and Salvigsen, O., 1995. Radiocarbon dated common mussels Mytilus edulis from eastern Svalbard and the Holocene marine climatic optimum. Polar Research, 14(2), 239–243.

Hutter, K., 1983. Theoretical Glaciology: Material Science of Ice and the Mechanics of Glaciers and Ice Sheets. D. Reidel Publishing Company, Dordrecht, The Netherlands.

Ignatieva, I. Y. and Macheret, Y. Y., 1991. Evolution of Nordaustlandet Ice Caps In Svalbard Under Climate Warming. International Association of Hydrological Sciences Publications (Symposium at St Petersburg 1990–Glaciers-Ocean-Atmosphere Interactions), 208, 301–312.

Jakobsson, M., Macnab, R., Mayer, L., Anderson, R., Edwards, M., Hatzky, J., Schenke, H. W., and Johnson, P., 2008. An improved bathymetric portrayal of the Arctic Ocean: Implications for ocean modeling and geological, geophysical and oceanographic analyses. Geophysical Research Letters, 35(7), L07602.

Jiskoot, H., Murray, T., and Boyle, P., 2000. Controls on the distribution of surge-type glaciers in Svalbard. Journal of Glaciology, 46(154), 412–422.

Kamb, B., 1987. Glacier Surge Mechanism Based On Linked Cavity Configuration of the Basal Water Conduit System. Journal of Geophysical Research-Solid Earth and Planets, 92(B9), 9083–9100.

Kamb, B., Raymond, C., Harrison, W., Engelhardt, H., Echelmeyer, K., Humphrey, N., Brugman, M., and Pfeffer, T., 1985. Glacier Surge Mechanism - 1982-1983 Surge of Variegated Glacier, Alaska. Science, 227(4686), 469–479.

Kotlyakov, V. and Macheret, Y., 1987. Radio-echo sounding of sub-polar glaciers in Svalbard: some problems and results of Soviet Studies. Annals of Glaciology, 9, 151–159.

Lauritzen, Ø. and Ohta, Y., 1984. Geological map of Svalbard, 1:500 000, Sheet 4G, Nordaustlandet. Norsk Polarinstitutt, Skrifter, 154 D, 14pp., 1 map.

MacAyeal, D., 1993. Binge/purge oscillations of the Laurentide Ice Sheet as a cause of the North Atlantic's Heinrich events. Paleoceanography, 8(6), 775–784.

Macheret, Y., Bobrova, L., and Sankina, L., 1991. Volumetric hydrothermal state and regime of the Spitsbergen glaciers from airborne radio-echo sounding [In Russian with English summary]. Data of Glaciological Studies, 71, 40–53.

Macheret, Y. and Vasilenko, E., 1988. Pecularities of internal structure and regime of glaciers on Nordaustlandet by airborne radio-echo sounding data [In Russian with English summary]. Data of Glaciological Studies, 62, 44–56.

Marshall, S., Tarasov, L., Clarke, G., and Peltier, W., 2000. Glaciological reconstruction of the Laurentide Ice Sheet: physical processes and modelling challenges. Canadian Journal of Earth Sciences, 37(5), 769–793.

Meier, M. and Post, A., 1969. What are glacier surges. Canadian Journal of Earth Sciences, 6(4P2), 807–817.

Moholdt, G., Hagen, J., Eiken, T., and Schuler, T., 2010. Geometric changes and mass balance of the Austfonna ice cap, Svalbard. The Cryosphere, 4(1), 21–34.

Morland, L., 1984. Thermomechanical balances of ice-sheet flows. Geophysical and Astrophysical Fluid Dynamics, 29(3), 237–266.

Murray, T., Stuart, G., Miller, P., Woodward, J., Smith, A., Porter, P., and Jiskoot, H., 2000. Glacier surge propagation by thermal evolution at the bed. Journal of Geophysical Research-Solid Earth, 105(B6), 13491–13507.

Payne, A., 1995. Limit-cycles In the basal thermal regime of ice sheets. Journal of Geophysical Research-Solid Earth, 100(B3), 4249–4263.

Payne, A., Huybrechts, P., Abe-Ouchi, A., Calov, R., Fastook, J., Greve, R., Marshall, S., Marsiat, I., Ritz, C., Tarasov, L., and Thomassen, M., 2000. Results from the EISMINT model intercomparison: the effects of thermomechanical coupling. Journal of Glaciology, 46(153), 227–238.

Pfeffer, W. T., 2007. A simple mechanism for irreversible tidewater glacier retreat. Journal of Geophysical Research-Earth Surface, 112(F3), F03S25.

Pinglot, J., Hagen, J., Melvold, K., Eiken, T., and Vincent, C., 2001. A mean net accumulation pattern derived from radioactive layers and radar soundings on Austfonna, Nordaustlandet, Svalbard. Journal of Glaciology, 47(159), 555–566.

Raymond, C., 1987. How do glaciers surge - a review. Journal of Geophysical Research-Solid Earth and Planets, 92(B9), 9121–9134.

Ritz, C., 1987. Time dependent boundary conditions for temperature fields in ice sheets. In: Waddin, E. and Walder, J. (Eds.), The Physical Basis of Ice Sheet Modelling, number IAHS Publication No. 170, Wallingford, UK. IAHS Press.

Schuler, T., Crochet, P., Hock, R., Jackson, M., Barstad, I., and Johannesson, T., 2008. Distribution of snow accumulation on the Svartisen ice cap, Norway, assessed by a model of orographic precipitation. Hydrological Processes, 22(19), 3998–4008.

Schuler, T., Loe, E., Taurisano, A., Eiken, T., Hagen, J., and Kohler, J., 2007. Calibrating a surface mass-balance model for Austfonna ice cap, Svalbard. Annals of Glaciology, 46, 241–248.

Schytt, V., 1969. Some comments on glacier surges In eastern Svalbard. Canadian Journal of Earth Sciences, 6(4P2), 867–871.

Shreve, R., 1984. Glacier sliding at subfreezing temperatures. Journal of Glaciology, 30(106), 341–347.

Smith, R. B. and Barstad, I., 2004. A linear theory of orographic precipitation. Journal of the Atmospheric Sciences, 61(12), 1377–1391.

Solheim, A., 1986. Submarine evidence of glacier surges. Polar Research, 4, 91–95.

Solheim, A., 1991. The depositional environment of surging sub-polar tidewater glaciers: a case study of the morphology, sedimentation and sediment properties in a surgeaffected marine basin outside Nordaustlandet, the Northern Barents Sea. Skrifter - Norsk Polarinstitutt, 194, 5–97.

Solheim, A. and Pfirman, S. L., 1985. Sea-floor morphology outside a grounded, surging glacier - Bråsvellbreen, Svalbard. Marine Geology, 65(1-2), 127–143.

Sund, M., Eiken, T., Hagen, J., and Kääb, A., 2009. Svalbard surge dynamics derived from geometric changes. Annals of Glaciology, 50(52), 50–60.

Tarasov, L. and Peltier, W., 1997. A high-resolution model of the 100 ka ice-age cycle. Annals of Glaciology, 25, 58–65.

Taurisano, A., Schuler, T., Hagen, J., Eiken, T., Loe, E., Melvold, K., and Kohler, J., 2007. The distribution of snow accumulation across the Austfonna ice cap, Svalbard: direct measurements and modelling. Polar Research, 26(1), 7–13.

Tulaczyk, S., Kamb, W. B., and Engelhardt, H. F., 2000. Basal mechanics of Ice Stream B, West Antarctica 2. Undrained plastic bed model. Journal of Geophysical Research-Solid Earth, 105(B1), 483–494.

Vasilenko, E., Navarro, F., Dunse, T., Eiken, T., and Hagen, J., 2010. New low-frequency radio-echo soundings of Austfonna ice cap, Svalbard. In: Ahlstrøm, A. and Sharp, M. (Eds.), The Dynamics and Mass Budget of Arctic Glaciers. Extended abstracts. Workshop and GLACIODYN (IPY) meeting, 16−19 February 2009, Kananaskis, Canada., volume 127 of Danmarks og Grønlands geologiske undersøkelse rapport. GEUS, Copenhagen: IASC Working Group on Arctic Glaciology.

Yde, J. and Paasche, Ø., 2010. Reconstracting climate change: not all glaciers suitable. EOS, Transactions American Geophysical Union, 91(21), 189–190.

Zagorodnov, V., Sinkevich, S., and Arkhipov, S., 1989a. Hydrothermal regime of the ice-divide area of Austfonna, Nordaustlandet[In Russian with English summary]. Data of Glaciological Studies, 68, 133–141.

Zagorodnov, V., Sinkevich, S., and Arkhipov, S., 1989b. Ice core express-analysis for structure and thermal regime studies of Austfonna [In Russian with English summary]. Data of Glaciological Studies, 66, 149–158.

Zweck, C. and Huybrechts, P., 2005. Modeling of the northern hemisphere ice sheets during the last glacial cycle and glaciological sensitivity. Journal of Geophysical Research-Atmospheres, 110(D7), D07103.

Appendix

A Transient simulations of Austfonna: a contribution to the model initiative GlacMod2010

An initiative by H. Oerlemans, termed GlacMod2010, calls on the glacier-modelling community to investigate the response of an appreciable number of simulated glaciers and ice caps to a set of climate-change scenarios up to the year 2010 (personal communication H.Oerlemans, Institute for Marine and Atmospheric Research, Utrecht University, Utrecht, The Netherlands, 2010). A synthesis report is to be compiled with the aim to facilitate projections of the contribution of glaciers and ice caps to global sea level rise in a warming climate.

A.1 Reference forcing and initial state

The climate input consists of monthly mean precipitation and temperature fields and is based on ERA-40 and ERA-Interim reanalysis data at a 6 hour temporal resolution, for the period 1980 to 2009 (in the case of the precipitation field only until 2006). The downscaling algorithm for the precipitation field utilizes a simple precipitation model (Schuler, 2010), while the temperature was extracted for a single location, at which temperature observations for the time period 2004-2009 where available for bias-removal. The local temperature record was then distributed over space by using surface elevations and by assuming a reasonable lapse rate of $-0.0045\,^{\circ}\mathrm{C\,m^{-1}}$.

We run the GlacMod2010-simulations of Austfonna twice, with slightly different submelt-sliding parameter and initial state, IS-A and IS-B, respectively. The initial states do not represent dynamically calibrated states. This has a number of reasons: firstly, no record of past glacier variations over a sufficiently long time period does exist. Secondly, the present dynamics, shape and areal extent of Austfonna are highly influenced by the surge activity of individual basins. Such flow instabilities can be reproduced by the model

(Dunse *et al.*, 2011), however, without control on the exact phase or principle period of the surge cycle. Instead, the chosen initial states correspond to 30 ka runs according to experiment 2 of Dunse *et al.* (2011) (sliding over hard rock, reduced effective basal normal pressure for marine ice), employing a submelt-sliding parameter, $\gamma = 0.2°C$ in the case of IS-A, $\gamma = 0.5°C$ in the case of IS-B, respectively. For IS-A, both the total ice volume and areal extent correspond well to the present values. Furthermore, large-scale surge behaviour, which would potentially mask climate induced changes over the model-run time, is absent, although some spatial and temporal variability in glacier flow and hence, glacier outline and shape do exist. The introduction of IS-B aims to investigate the sensitivity of the glacier response to the initial conditions and the description of basal motion at sub-freezing temperatures. Furthermore, it provides conditions so that the control run (Exp. 1) does not produce a growing ice cap (becomes clear in section A.3). The run producing IS-B is analog to the one for IS-A, but with enhanced submelt sliding, $\gamma = 0.5°C$. A constant temperature offset $T' = –0.25°C$ was applied to compensate for the increased mass flux towards the margin caused by increased submelt sliding, and hence ice loss. The ice cap described by IS-B has a similar total ice volume as the present-day ice cap, or the ice cap described by IS-A, however, the flat shape leads to a larger areal extent compared to the other states. Table A.1 lists ice cap volume and areal extent for present-day geometry and the 2 initial states, IS-A and IS-B.

	Present	**IS-A**	**IS-B**
Volume (km^3)	2585	2482	2489
Area (km^2)	8332	8400	9388

Table A.1: Ice cap volume and areal extent for present-day geometry and the 2 initial states, IS-A and IS-B.

A.2 Model experiments

The model experiments follow the GlacMod2010 initiative coordinated by Hans Oerlemans (personal communication H. Oerlemans, 2010). All experiments are run for the time period 2010–2100. The requested output is annual total glacier volume, areal extent and the mass budget components, consisting of surface mass balance and calving flux. Utilizing IS-A as initial conditions, the submelt-sliding parameter is set to $\gamma = 0.2°\mathrm{C}$, $\gamma = 0.5°\mathrm{C}$ for IS-B respectively.

A.2.1 Experiment 1: no climate change

The model is forced with the reference climate. This experiment is meant to provide an idea of the current imbalance of the glacier, as described by the given initial state, with respect to the reference climate.

A.2.2 Experiment 2: linear temperature-precipitation change scenarios

The model is forced with a linear increase in temperature, T', with and without an associated increase in precipitation, P':

$$T'(t) = \lambda t, \tag{A.1}$$

where t is the time in years and λ a temperature increase per year, and

$$\frac{P'(t)}{\overline{P}} = \mu T', \tag{A.2}$$

where $\overline{P}$ is the reference precipitation rate, and the relative change in precipitation is assumed to be linear related to the temperature change, T', given in Kelvin, by a constant of proportionality, μ.

A total number of 9 runs are performed with $\lambda \in [0.01,\ 0.02,\ 0.04\,\mathrm{K\,a^{-1}}]$ and $\mu \in [0.00,\ 0.05,\ 0.10\,\mathrm{K^{-1}}]$ and referred to as E-λ-μ.

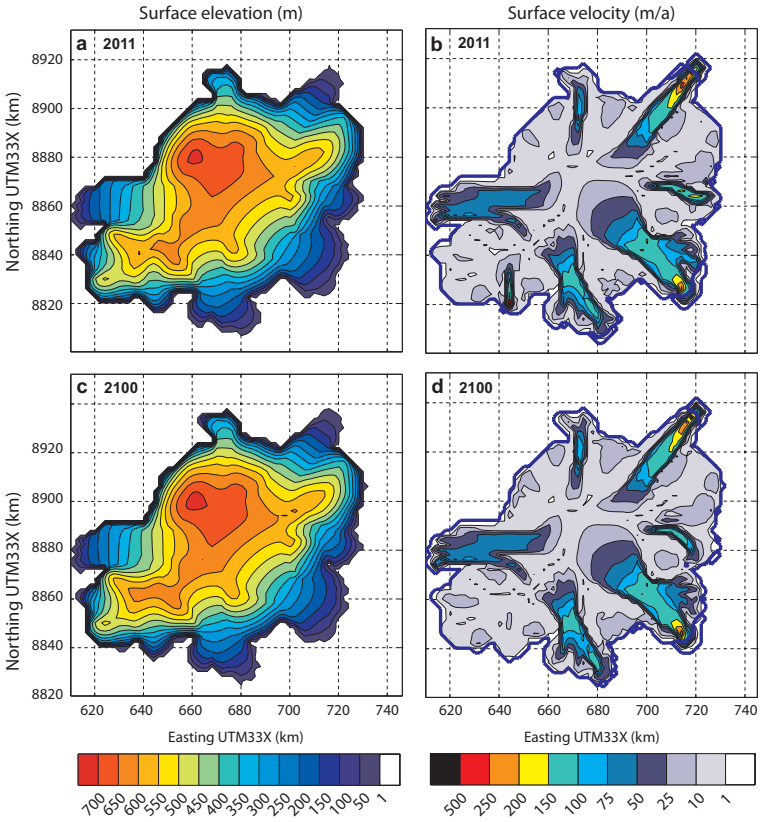

Figure A.1: Simulated surface elevation (a,c) and surface velocities (b,d) in experiment 1, after the first year (upper panel) and last year (lower panel) of model integration.

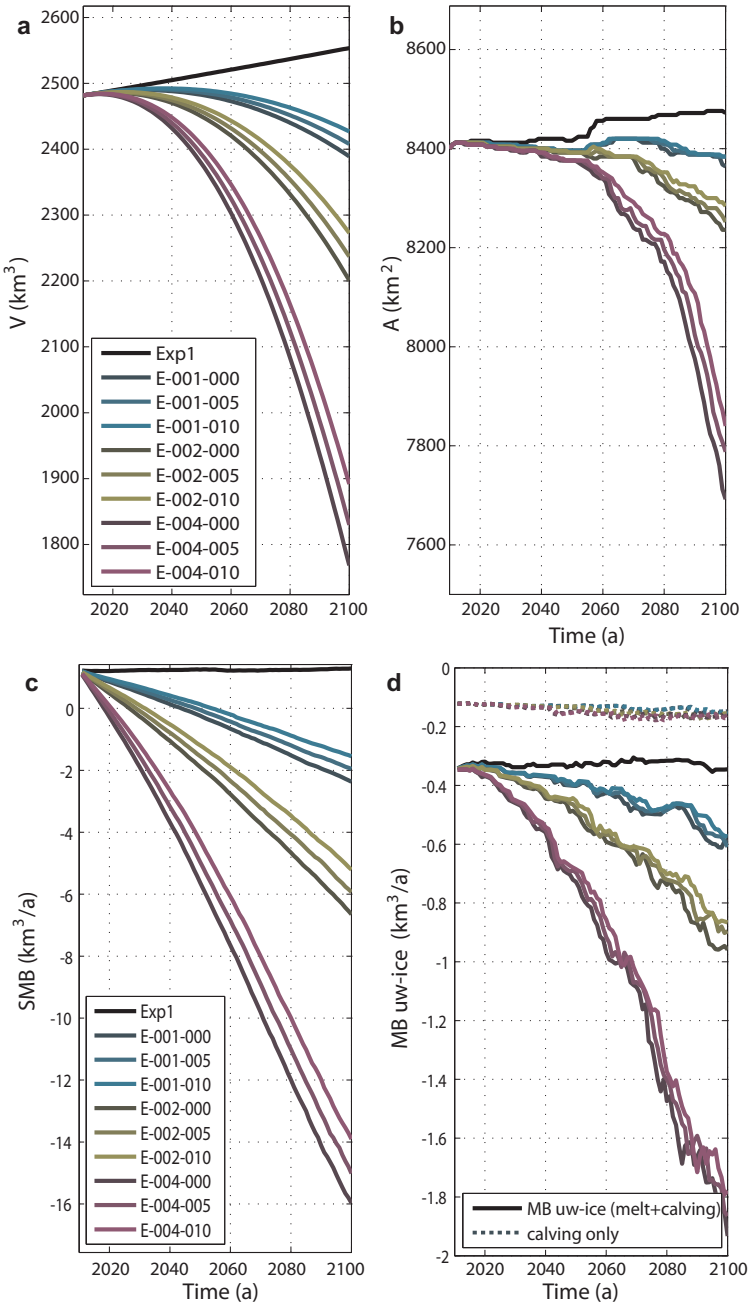

Figure A.2: Evolution of Austfonna during GlacMod2010 time period in terms of (a) ice volume, (b) areal extent, (c) annual surface mass balance (SMB) and (d) calving rate.

A.3 Results and Discussion

We will first discuss the results related to IS-A. An overview of the general model performance in terms of the simulated surface elevation and surface velocities is provided in Figure A.1. Results are shown for a constant reference climate (Exp. 1), after the first and last year of model integration. The bulk of the ice cap is slowly moving ($<$10 m a^{-1}), interrupted by several fast flow units with moderate velocities of 50-250 m a^{-1}. While the general flow pattern in 2011 and 2100 compares well, local changes do exist: e.g. in the southeast, where a small and narrow flow unit is active in 2011, but almost stagnant in 2100; or in the northeast, where a flow unit of similar extent changes its direction.

The temporal evolution in terms of total ice volume, areal extent, and mass balance rate distinguishing between surface mass balance (SMB) and calving, is displayed in Figure A.2. In the case of a constant reference climate (Exp. 1) the ice cap grows during the period 2010–2100, both in terms of volume (2482–2553 km^3) and areal extent (8400–8472 km^2). This can be explained by the fact that the reference climate for 1980–2006 is slightly colder than the idealized present-day climate used by Dunse *et al.* (2011), where the temperature fields built on field data recorded in 2004–2009. In the case of the temperature-precipitation scenarios (Exp. 2), ice wastage related to both SMB and calving and melt of uw-ice, increases nonlinearly with time during the first decades, but almost linearly with time during the last decades (as apparent from the second derivative of SMB). The sensitivity of the glacier response increases non-linearly with the different temperature scenarios, e.g. a doubling of the temperature increase from 1 to 2°C triples ice wastage by means of SMB from about 2 to 6 km^3 a^{-1}, while a 4-fold temperature increase leads to 8-fold increase in surface ablation. The total ice loss from the uw-ice is characterized by larger fluctuations than the SMB component of the stable grounded ice. Furthermore, the mass loss computed by the calving law is comparably insignificant, one orders of magnitude smaller than the mass loss from melting.

The experiments performed using IS-B aim at investigating the compensating effect of a growing ice cap with forcing given by the reference climate (Exp. 1) on ice wastage in a warming climate (Exp. 2), as produced using IS-A. In the control run (Exp. 1) the ice cap volume and areal extent decreases slightly. The general response of the model in Exp. 2, compared to the control run is similar to the one related to IS-A (Fig. A.3). For example, subtracting the 2010 volume of run E-001-000, E-002-000, E-004-000 for IS-B from the control run (Exp. 1) leads to 188, 398 and 863 km^3, compared to 164, 353 and 785 km^3,

in the case of IS-A. The mass balance components are slightly more negative, due to the larger areal extent of the ice mass at lower elevations compared to IS-A.

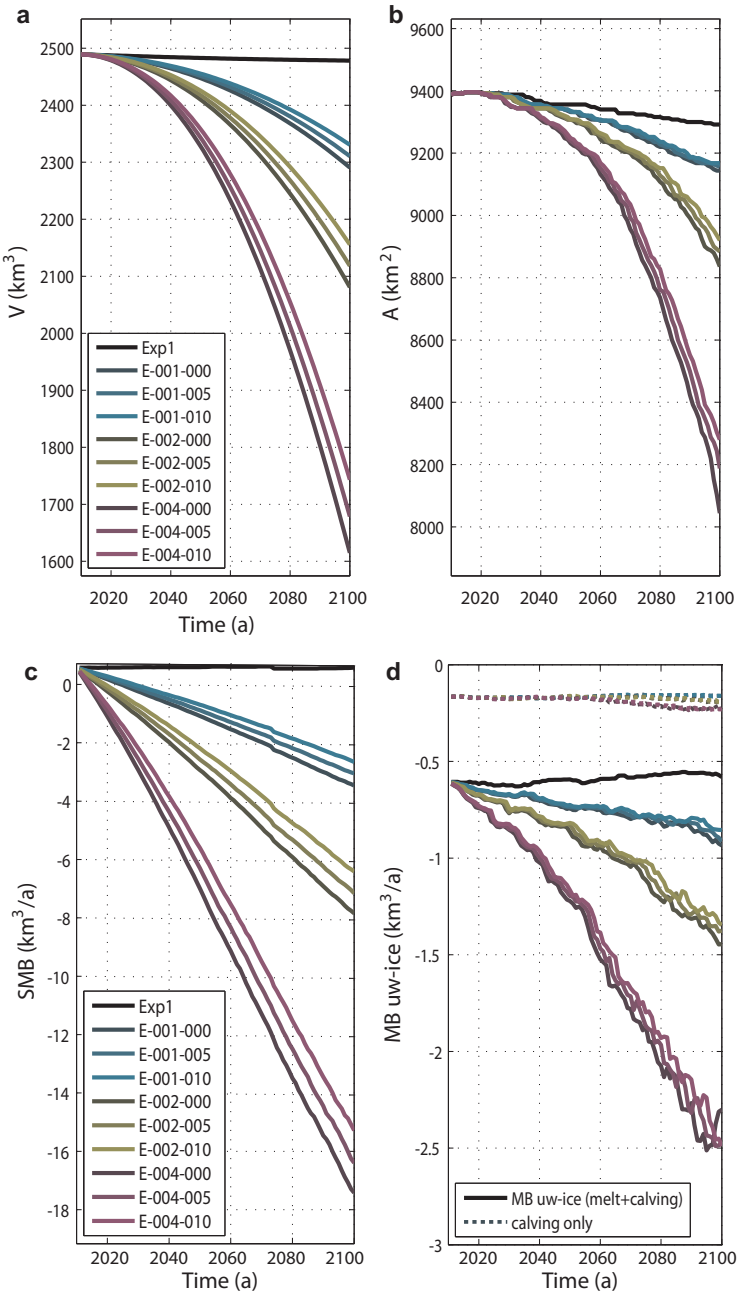

Figure A.3: Evolution of Austfonna during GlacMod2010 time period in terms of (a) ice volume, (b) areal extent, (c) annual surface mass balance (SMB) and (d) calving rate.

References

Dunse, T., Greve, R., Schuler, T., and Hagen, J., 2011. Permanent fast flow vs. cyclic surge behavior: numerical simulations of the Austfonna ice cap, Svalbard. Journal of Glaciology, 57(202), 13 pp.

Schuler, T., 2010. A surface mass balance history of Austfonna, Svalbard, derived from reanalysis data. In: IPY Oslo Science Conference, 8–12 June 2010, Oslo, Norway.